# Skin Hydration and Solvent Penetration Measurements by Opto-thermal Radiometry, AquaFlux and Fingerprint Sensor

## XIANG OU

**London South Bank University**

PhD

# April 2014

# To my parents…

# Content

# Abstract

The aim of this study is to develop new data analysis techniques and new measurement methodologies for skin hydration and solvent penetration measurements by using Opto-Thermal Transient Emission Radiometry (OTTER), AquaFlux and capacitive contact imaging based on Fingerprint sensor, three novel technologies developed by our research group.

This research work is divided into three aspects: the theoretical work, the experimental work and the portable opto-thermal radiometry hardware design work. In the theoretical work, a) an effective image retrieval method based on Gabor wavelet transform has been developed, the results show that it is particularly useful for retrieving the grayscale capacitive skin images; b) an algorithm based on Grey Level Co-occurrence Matrix (GLCM) has been developed to analyze the grayscale capacitive skin images; c) a comparison study of Gabor wavelet transform, Grey level co-occurrence matrix (GLCM) and Principal Component Analysis (PCA) has been conducted in order to understand the performance of each algorithm, and to find out which algorithm is suitable for what type of images. In the opto-thermal radiometry hardware design work, a new, low cost, portable opto-thermal radiometry instrument, based on a broadband Infrared emitter and a room temperature PbS detector, has been designed and developed. The results show that it can work on any unprepared sample surfaces. In the experimental work, various *in-vivo* and *in-vitro* measurements were performed in order to study skin hydration and solvent penetration through skin and membranes. The results show that, combined with tape stripping, capacitive skin imaging can be a powerful tool for skin hydration, skin texture and solvent penetration measurements. The effect of three different parameters of Fingerprint sensor and its detection depth are also studied. The outcomes of this work have provided a better understanding for skin hydration and solvent penetration measurements and have generated several publications.

# Acknowledgment

First I like to express my thanks to Dr. Perry Xiao, my supervisor, for his guidance, support and patience during this PhD work. These totally changed my way of thinking of engineering and science.

Thanks also go to my colleagues in the Photophysics group of South Bank University for their help and useful discussion.

I thank my parents for their care and encouragement, without them life will be meaningless.

Finally, I like to thank my friends, classmates and everyone who had ever spent effort in helping me to get this studying opportunity. Without their friendships, encouragement and assistance, I can never be what I am today.

## Chapter 1  Introduction and Skin Review

Human skin is a uniquely engineered organ that acts as a barrier to protect the body from the external environment, and also functions to regulate heat and water loss from the body. According to British Skin Foundation, there are eight million people living with skin diseases in UK, some skin diseases are manageable, others are severe enough to kill. Skin diseases have a major impact on quality of life (QoL).  Skin cosmetics are also a big industry. According to the Cosmetic, Toiletry & Perfumery Association, UK cosmetic market is worth more than £8b in 2011, and there are more than 4000 cosmetic companies in EU. The skin research plays a key role in cosmetic industry, as well as skin health.

Our research group, originally founded by Prof R E Imhof, has more than 25 years of experiences in skin research, and has developed several skin measurement technologies, such as Opto-Thermal Transient Emission Radiometry (OTTER), AquaFlux and capacitive contact imaging based on Fingerprint sensor. The overview of the three technologies can be found in chapter 2. The aim of this research project is to build on existing research work of the group, and to developed new data analysis techniques and new measurement methodologies for skin measurements using OTTER, AquaFlux and capacitive contact imaging technologies.

This research work is divided into three themes, namely, the theoretical work, the experimental work, and the opto-thermal radiometry hardware design work.  For the theoretical work, the aim is to develop new mathematical algorithms to analyze capacitive skin images. The details are described in chapter 3, 4 and 7.

For the opto-thermal radiometry hardware design work, the aim is to design a novel, low cost, portable opto-thermal radiometry instrument for skin measurements, using modulated broadband Infrared emitter and a room temperature PbS (lead sulphide) detector. The details are described in chapter 5.

For the experimental work, the aim is to develop new skin measurement methodologies and to have a better understanding of capacitive imaging

measurements. The details are described in chapter 6.

This chapter provides a general introduction and review of skin histology, skin hydration measurements, and organization of the thesis.

## 1.1 Skin Histology

The skin is the heaviest single organ of the body, accounting for about 16% of total body weight. Skin is a barrier to provide protections against environmental hazards, such as radiological and microbial attacks, physical and chemical. It also works as a sensor to transmit environmental information such as pain, cool to the nerve centre and depot to store excess food as fat for future use [1]. For an average 70 kg human being, the surface area is about $1.8m^2$. A typical square centimetre covers 10 hair follicles, 12 nerves, 15 sebaceous glands, 100 sweat glands, 3 blood vessels with 92 cm total length, 360 cm of nerves and $3 \times 10^6$ cells.

Human skin may be subdivided into three mutually dependent layers: the fatty **subcutaneous layer** (hypodermis), the overlying **dermis**, and the **epidermis**, the outermost layer of the skin (Figure 1.1, from [2]). Human skin displays two main types. Hairy skin encloses hair follicles and sebaceous glands, but there no encapsulated sense organs. Glabrous skin of the palms and the soles constructs a thick epidermis with a compact stratum corneum, but the integument lacks hair follicles and the dermis supports encapsulated sense organs. Ridges groove hairless skin into individually unique configurations termed dermatoglyphics. Besides providing identification, for example, fingerprints, dermatoglyphics may aid diagnosis or they may indicate that a patient has an increased tendency to develop certain diseases.

### 1.1.1 The Epidermis

The epidermis (Figure 1.2, from [2]) which is a stratified epithelium containing one layer of proliferative cells and several layers of differentiated cells is the most superficial layer of human skin [3]. The cells of the epidermis are produced from the basal layer and migrate to the exterior, undergoing keratinisation to form the

outermost layer, the stratum corneum. It varies in thickness from 0.8 mm on the palm to 0.06 mm on the eyelids. The epidermis can be subdivided into five layers:
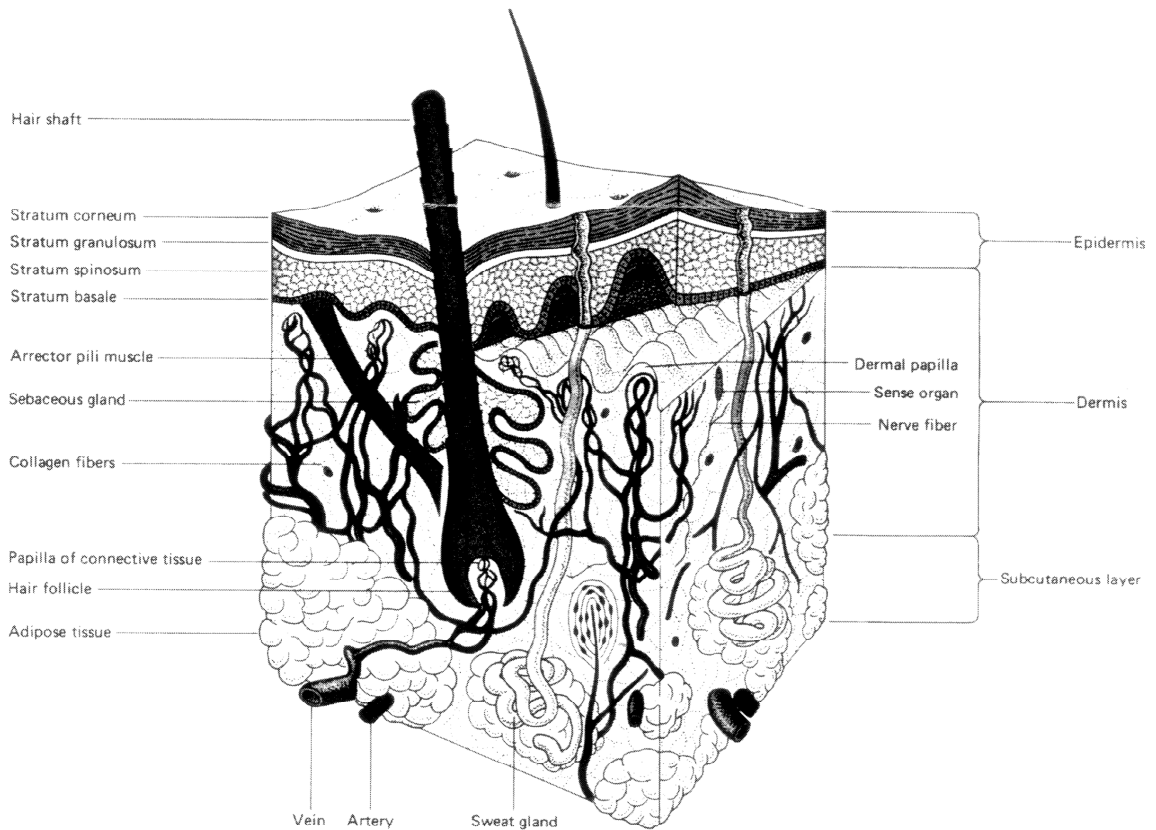


*Figure 1.1   Structure of Human Skin, from Van De Graaff KM, Fox SI. [2]*

(1) The stratum basale (stratum germinativum).

The stratum basale is characterized by intense mitotic activity and is responsible, in conjunction with the initial portion of the next layer, for constant renewal of epidermal cells. The cell division occurs in this layer. New keratinocytes which move upwards pushing the older above towards the surface of the skin are generated by the basal keratinocytes.

(2) The stratum spinosum.

The cells begin to flatten and their nuclei shrink in this layer. The epidermis of areas subject to continuous friction and pressure (such as the sole of the feet) has a thicker stratum spinosum with more abundant tonofibrils and desmosomes.

(3) <u>The stratum granulosum</u> (granular layer).

It is characterized by 3-5 layers of flattened polygonal cells containing centrally located nuclei and cytoplasm. Its shape is membrane-coating granule, ovoid or rodlike. The cells generate keratohyalin granules in this layer.



**Stratum corneum**
Consists of many layers of keratinized, dead cells that are flattened and nonnucleated; cornified

**Stratum lucidum**
A thin, clear layer found only in the epidermis of the palms and soles

**Stratum granulosum**
Composed of one or more layers of granular cells that contain fibers of keratin and shriveled nuclei

**Stratum spinosum**
Composed of several layers of cells with centrally located, large, oval nuclei and spinelike processes; limited mitosis

**Stratum basale**
Consists of a single layer of cuboidal cells that undergo mitosis; contains pigment-producing melanocytes

***Figure 1.2*** *Structure of Epidermis, from Van De Graaff KM, Fox SI [2]*

(4) <u>The stratum lucidum</u>.

It is a thin translucent layer and is generated in the palm of the hand and the sole of the foot, an anatomically distinct, poorly staining hyaline zone.

**Permeation Enhancement through Skin**

Figure content:

Intercellular route  Transcellular route

Plasma membrane  Cell cytoplasm  Fatty acid  Intrinsic protein

Intercellular space

Lipid  Aqueous  Ceramide  Cholesterol/Cholesterol sulfate  Lipid  Keratin
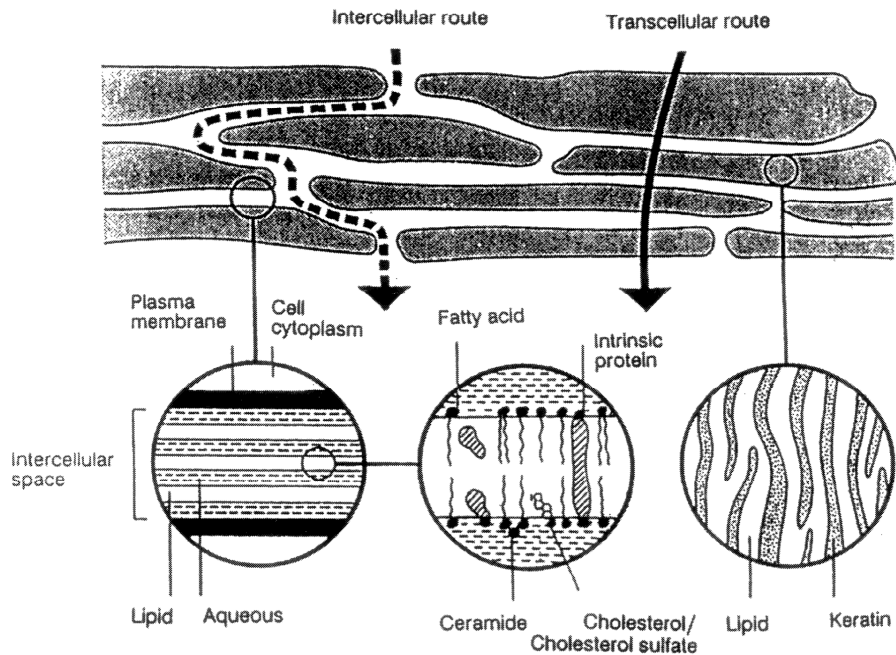
*Figure 1.3 The "brick and mortar" structure of the stratum corneum [4].*

(5) <u>The stratum corneum</u> (The horny layer).

It is the most superficial layer of the skin and comprises 10 to 15 layers of dead cells with approximately 10-20 $\mu m$ thickness. The structure of the stratum corneum may be represented as a brick and mortar model which provides two micro pathways for the trans-epidermal drug diffusion (Figure 1.3 [4]). When the cells arrive at the SC, they are fully keratinized and dead.

The Epidermis contains three less abundant cell types: Melanocytes, the Langerhans Cells, and the Merkel Cells.

### 1.1.2   The Dermis

The dermis shown in Figure 1.4 [2] is the second layer of the skin. The connective tissue that supports the epidermis and binds it to the subjacent layer forms the dermis. The thickness of the dermis varies depending upon the region of the body, reaching its

maximum of 3 mm on the soles of the feet [5]. The epidermis can be subdivided into two anatomical regions [6]:


(1) The papillary dermis.

It is the thinner outermost portion of the dermis and constitutes approximately 10% of the 1-4 mm thick dermis.

(2) The reticular dermis.

It can extend up to about 25% by stretching the collagen fibers. Meanwhile, it can be squeezed due to the capacity to displace the ground substance laterally.
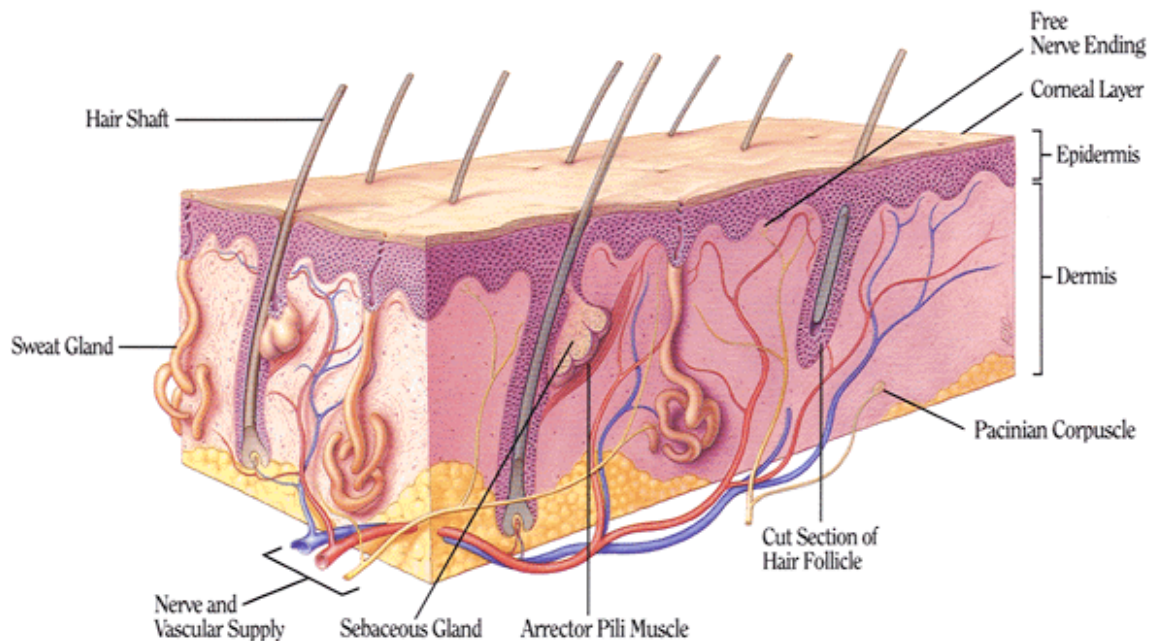


***Figure 1.4*** *Structure of dermis [2]*


The dermis is composed of two layers. One is the immediately sub epidermal papillary layer, and another is the deeper, more massive and denser the reticular layer. The dermis has a rich network of blood vessels which regulates temperature and pressure, delivers nutrients to the skin and removes waste products, mobilizes defence forces, and contributes to skin colour. The dermis also contains some epidermal derivatives, the hair follicles, sweat and sebaceous glands. A rich supply of nerves is found in the dermis, and the effector nerves to the skin are postganglionic fibres of the ganglia of the par vertebral chain.

*1.1.3 The Subcutaneous Tissue*

The subcutaneous fat (hypodermis, sub cutis) spreads all over the body. The size of this layer varies throughout the body and from person to person. The sub cutis provides a thermal barrier and a mechanical cushion; it is a site of synthesis and depot of readily available high-energy chemicals [7]. It carries the major blood vessels and nerves to the skin and may contain sensory pressure organs [4]. The information of human subcutaneous fat is useful for assessing health risks due to obesity and for monitoring athletes' health status, body shapes and weight for various sports competitions such as gymnastics and wrestling [8].

*1.1.4 Skin Functions*

The skin performs many varied functions; the following presents a brief digest of its biological role [3].

1. To contain body fluids and tissues --the mechanical function.
2. To protect from potentially harmful external stimuli--the protective or barrier function: (a) micro-organisms; (b) chemicals; (c) radiation; (d) heat; (e) electrical barrier; or (f) mechanical shock.
3. To receive external stimuli, i.e., to mediate sensation: (a) tactile (pressure); (b) pain; or (c) heat.
4. To regulate body temperature.
5. To synthesize and to metabolize compounds.
6. To dispose of chemical wastes.
7. To provide identification by skin variations.
8. To attract the opposite sex.
9. To regulate blood pressure.

## *1.2 Skin Hydration*

A water profile in skin calculated from Energy Dispersive Spectrometry Spectra [9] is shown in Figure 1.5 [9]. The water in skin and its relationship to the skin function will be introduced in the following section.

### *1.2.1 Skin Hydration*

The relationship between relative humidity and water contents of the stratum corneum is shown in Figure 1.6 [10]. According to Takenouchi M, at 0% relative Humidity (RH), stratum corneum still holds about 0.05 g/g water.
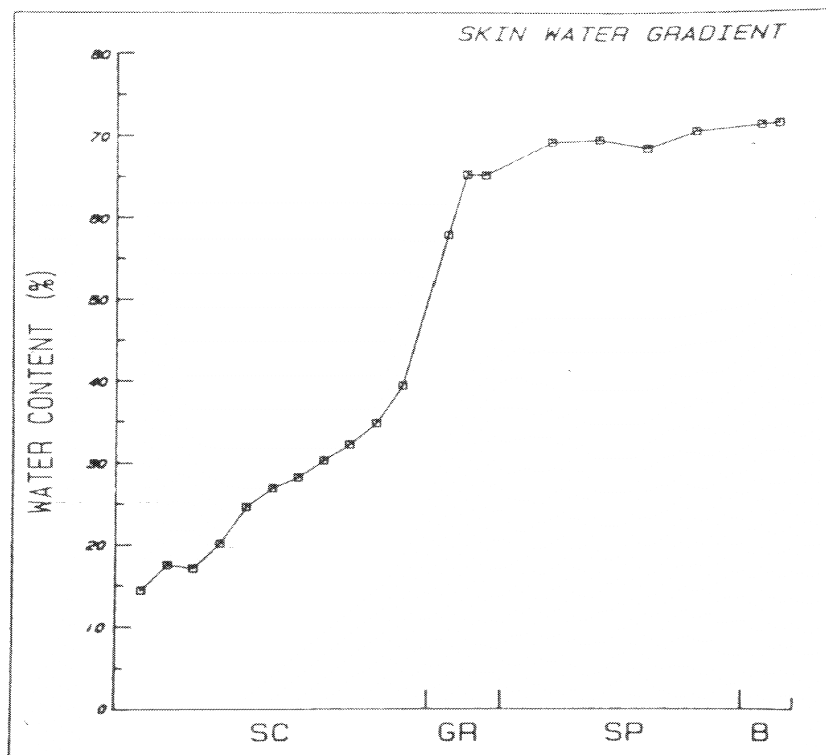


***Figure 1.5*** *Calculated Water profile across human skin. Vertical scale is percent water expressed as grams of water per total grams (water plus dry mass) of tissue. SC stands for Stratum Corneum, GR stands for Stratum Granulosum, SP stands for Stratum Spinosum, and B stand for Stratum Basale [9].*

*1.2.2 Water concentration profile and TEWL*

Stratum corneum is dry at its surface because of the dry external environment and wet at its base where it is contact with the deeper fully hydrated part of the epidermis [11]. Therefore, a concentration gradient which results in a continuing diffusion of water from within the body through the skin to the environment, trans-epidermal water loss (TEWL) will generate within the stratum corneum. The TEWL for normal skin is about 4~8 $g/m^2$ per h [12].
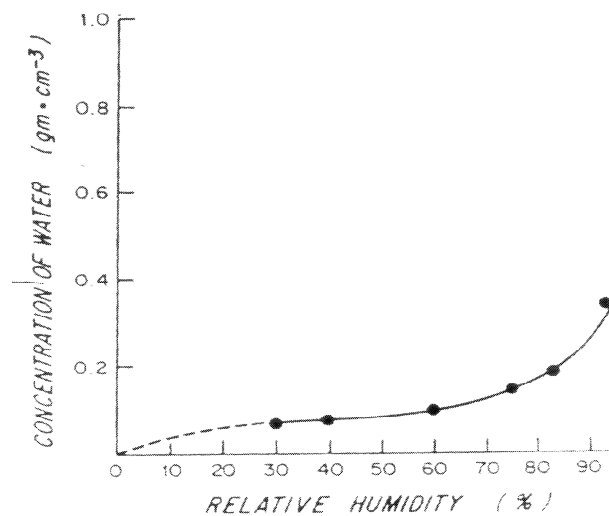


*Figure 1.6   Concentration of water in stratum corneum in equilibrium with air at 30 ℃ as a function of relative humidity [10].*

*1.2.3 The water in stratum corneum*

In the stratum corneum, there are three types of water: tightly bound water, loosely bound water and free water. The experiments from [13] show that the hydration and dehydration rates of free water are lower than that of bound water. This suggests that free water is located primarily intracellular, with the cell envelope the major barrier to its loss, while the bound water is primarily intercellular or on the cell surface.

## *1.3 Organization of the thesis*

Chapter 2 describes the conceptions and principles of OTTER, Aqua Flux and Fingerprint sensor, and their functions.

Chapter 3 presents an effective content-based image retrieving technique for different types of skin images. In this chapter, texture feature is used for retrieving images, and 2D Gabor wavelet transform, which is an important and promising method, is used for texture feature description and extraction. After applying 2D Gabor wavelet transform to images, the means and variances are calculated as texture features of the images for image retrieval.

Chapter 4 describes the grey level co-occurrence matrix (GLCM) technique for analyzing capacitive skin images. It first describes the theory of GLCM, then shows the GLCM results of capacitive skin images, finally, discusses how to select the optimum distance through analyzing the influence of distance change to the feature vectors.

Chapter 5 describes the design work of the new portable opto-thermal radiometry instrument which can work at room temperature. It first introduces the principle of infrared emitters and PbS detector, then introduces and explains their drive circuits, and finally shows the test results.

Chapter 6 describes five different experiments: the first one is tape stripping measurements by using AquaFlux and Fingerprint Sensor, the second one is *in-vivo* solvent penetration study by using capacitive Fingerprint Sensors and OTTER, the third one is measuring the Fingerprint Sensor detection depth, the fourth one is to study the effects of the three configuration parameters of the Fingerprint sensors on image quality and the last one is the measurements of 6 different solvents penetrating through the silicone membrane.

In chapter 7, three different algorithms, namely Principal Component Analysis (PCA), Grey level co-occurrence matrix (GLCM) and Gabor wavelet transform are compared

for image retrieval, in order to understand the pros and cons of each algorithm, and to find out which algorithm is suitable for what types of images.

Chapter 8 concludes this thesis and looks at possible and additional work that will be carried out in the future.

# Chapter 2 OTTER, AquaFlux and Fingerprint Sensor Overview

Over the past few years, many different measurement techniques have been applied in the research of skin hydration and solvent penetration, including electrical measurements, evaporimetry, infrared spectrometry, ultrasound, magnetic resonance imaging and photo thermal imaging etc. Each technique has its own strength and weakness [14]. Opto-thermal Transient Emission Radiometry (OTTER), AquaFlux and capacitive contact imaging based Fingerprint sensor are three novel and promising skin measurement techniques developed in our research group. This thesis presents the research work on skin hydration and solvent penetration measurements by using Opto-Thermal Transient Emission Radiometry (OTTER), AquaFlux and capacitive contact imaging based on Fingerprint sensor.

This chapter will present the conceptions and principles of OTTER, AquaFlux and Fingerprint sensor, and their functions.

## 2.1 OTTER

Opto-thermal transient emission radiometry (OTTER) [14-17], shown in Figure 2.1, is an infrared remote sensing technique based on photo-thermal radiometry (PTR) or Opto-thermal radiometry (OTR). Comparing with other skin hydration measurement instruments, OTTER has many advantages, such as, non-contact, non-invasive, work on arbitrary surfaces, in-sensitive to colour and small movements.

***Figure 2.1*** *OTTER [15]*

Figure 2.2 shows a schematic diagram of the OTTER. A Q-switched pulsed laser as the excitation source is used to heat up the sample surface and then generate a heat radiation. Heat radiation, whose wavelength region is in the mid-infrared ~5-15µm, is focused by an aluminum ellipsoidal mirror from the sample onto a high speed, liquid nitrogen cooled Mercury Cadmium Telluride (MCT) detector, whose signal is captured by a digital oscilloscope. A PC, linked to the digital oscilloscope through a high-speed PCI (Peripheral Component Interconnect) interface, is used for signal averaging, data storage, display and analysis. The shape of measured signal is dependent on sample's optical and thermal properties, the thickness of the sample and its layer structure.
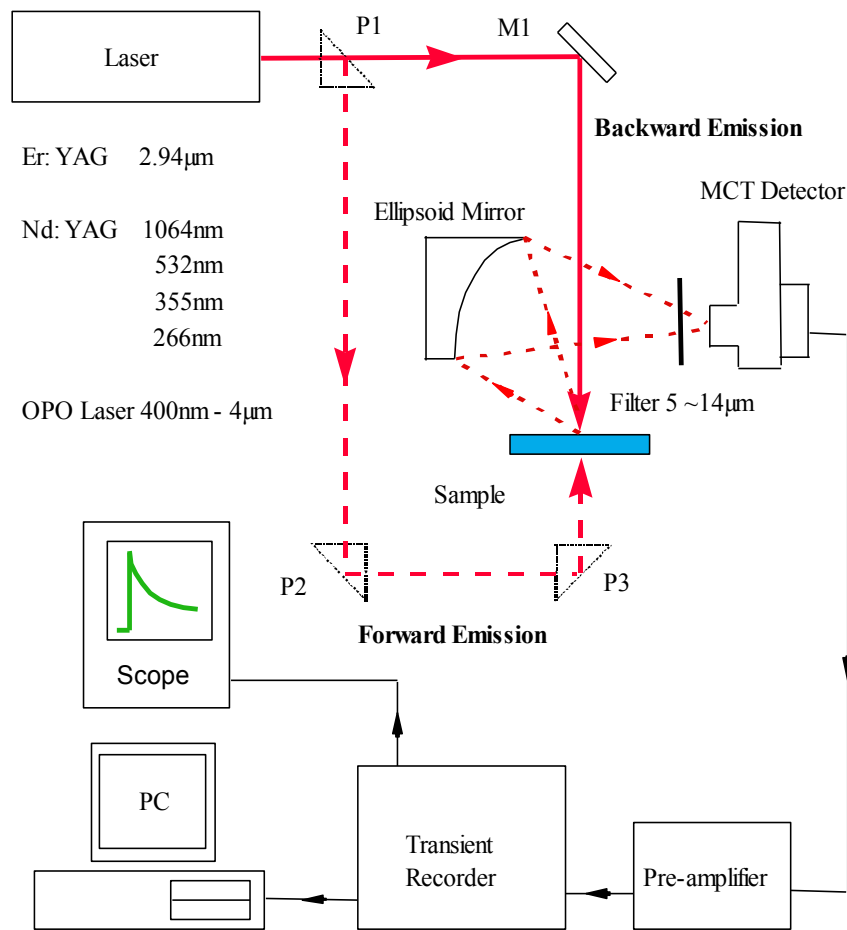
***Figure 2.2*** *Schematic Diagram of OTTER. P1, P2, P3 are prisms, and M1 is a mirror [15]*.

In Opto-Thermal physical process, OTTER measurements can be modeled as three sequential physical processes as follows:

(1) The near-surface region of the sample is heated by absorption of the incident laser energy. This establishes an initial temperature field at time $t = 0$.

(2) The absorbed energy diffuses within the sample and causes the temperature distribution to change with time (transient temperature field).

(3) Due to the changes of the transient temperature field, the thermal radiation from the sample surface changes. This heat radiation can be detected, recorded and analyzed as an opto-thermal signal.

Therefore, Opto-thermal signals can be modeled in three steps: (1) the initial temperature field; (2) the transient temperature distribution; (3) the infrared heat radiation. The main sample properties involved in these three steps: (1) the absorption coefficient for the laser radiation $\alpha$; (2) the thermal diffusivity D; (3) the absorption coefficient for the emitted thermal radiation $\beta$.

When laser radiation is incident on a sample surface, some radiation will penetrate into sample as it is absorbed. The initial temperature field can be expressed as:

$$\theta(z,0) = \frac{E_0 \alpha}{\rho C} e^{-\alpha z} \tag{2.1}$$

where $\theta(z,0)$ is the temperature at $t = 0$ of sample at position $z$, with $z = 0$ at the surface of the sample and increasing toward the inside of the sample. $C$ is the sample's specific heat, $\rho$ is the sample's density and $E_0$ is the energy density absorbed from the excitation pulse [18,19].

The temperature re-distribution after the initial disturbance follows the diffusion law, which can conveniently be expressed in Green's function form as:

$$\theta(z,t) = \int_0^t \int_0^\infty \frac{Q(z',t)}{\rho C} G(z,z';t,t') dz' dt$$

$$= \int_0^\infty \theta(z',0) G(z,z';t,t') dz' \tag{2.2}$$

where $G(z,z';t,t')$ is Green's function describing the temperature change in position $z$ at time $t$ due to a Dirac-Delta heat disturbance at position $z'$ and time $t'$. Therefore the transient temperature field $\theta(z,t)$ can be found by integration of the heat source and Green's function in the semi-space of the sample.

The opto-thermal signal comes from the transient thermal radiation, which is caused by the time-dependent temperature field $\theta(z,t)$ above. The calculation of Opto-thermal signal is given by [18, 19]:

$$S(t) = \varsigma \int_0^\infty \beta(z) e^{-\int_0^{\bar{z}} \beta(z)dz} \theta(z,t)dz \tag{2.3}$$

where the parameter $\varsigma = \varsigma(\lambda_{em})$ includes factors that depend on the blackbody emission curve, detector sensitivity, focusing and alignment, but is independent of the properties of the sample.

By substituting Eq. (2.1) and (2.2) into Eq. (2.3), and using semi-opaque limit, i.e. $\alpha \gg \beta$, or $\beta \gg \alpha$, we have

$$S(t) = A_1 e^{t/\tau_{\hat{\alpha}}} erfc \sqrt{t/\tau_{\hat{\alpha}}} \tag{2.4}$$

where $\hat{\alpha}$ is either $\alpha$ or $\beta$, $\tau_{\hat{\alpha}} = \dfrac{1}{\hat{\alpha}^2 D}$, $A_1 = \dfrac{\varsigma E_0 \hat{\alpha}}{\rho C}$ is the amplitude of the signal

and $erfc(x) = 1 - erf(x)$ is the complementary error function,

$erf(x) = \dfrac{2}{\sqrt{\pi}} \int_0^x e^{-y^2} dy$ is error function. The least-squares fitting of all signals of

OTTER measurements in this thesis is done by using Eq. (2.4).

OTTER has demonstrated the capability for measuring skin hydration, skin pigments, skin thickness and transdermal drug delivery [14, 17, and 19]. However, Skin measurement is not the only application of OTTER measurements. OTTER can also be used as a non-destructive evaluation technology for many industrial applications, such as [18]:

(1) Measurement of thermal properties of materials.

(2) Measurement of optical properties of materials.

(3) Measurement of paint thickness.

(4) Measurement of thermal resistance of materials.

(5) Material characterization.

(6) Flaw detection and characterization.

## 2.2 AquaFlux

AquaFlux [20-22], shown in Figure 2.3, is a novel condenser-based, closed chamber technology for measuring water vapour flux density from arbitrary surfaces, including *in-vivo* measurements of trans-epidermal water loss (TEWL), skin surface water loss (SSWL) and perspiration. It uses a cylindrical measurement chamber, with one end open and attached to the sample surface, and another end closed and cooled down to below the water freezing point.



**Figure 2.3** *AquaFlux [20]*

Figure 2.4 shows a simple cutout diagram of the AquaFlux condenser-chamber. When the chamber is brought in contact with the skin surface, the chamber is sealed and it can protect the diffusion zone within it from ambient air movement. The natural convection and other bulk air movements are brought down because of the internal dimensions of the chamber being very small. In fluid dynamics terms, this requires the Rayleigh Number to be below the critical value for its geometry. Under these conditions, passive diffusion remains the only transport mechanism for the water vapour entering the chamber. The condenser controls the absolute humidity in the measurement chamber independently of ambient conditions. It is similar to a vapour sink by forming ice on its surface, thus creating a zone of low humidity in its

immediate vicinity. By contrast, the test surface acts as a vapour source, creating a zone of higher humidity in its immediate vicinity. This humidity difference causes
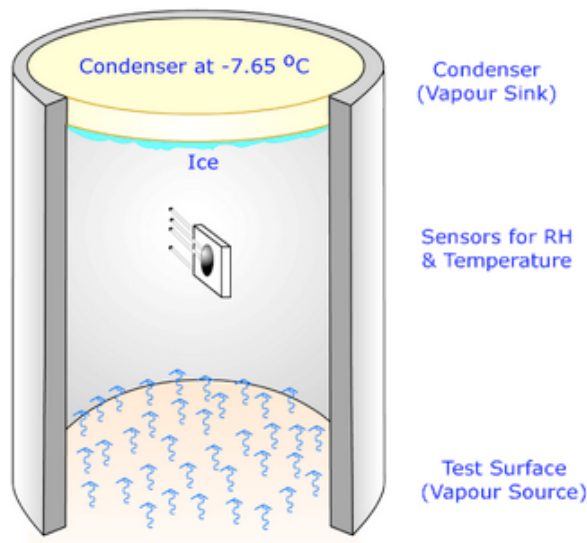


*Figure 2.4 a simple cutout diagram of the AquaFlux condenser-chamber [20]*

water vapour to migrate from source to sink by passive diffusion and creates a diffusion vapour density gradient, from which the flux density can be measured. The process of calculation is introduced as follows [21]:

Since the size of sample is normally much greater than the measurement orifice, the measurement principles are discussed under one dimension, and the Cartesian coordinate system is used, shown as Figure 2.5.



*Figure 2.5 Geometry of 1-D AquaFlux modeling [21]*

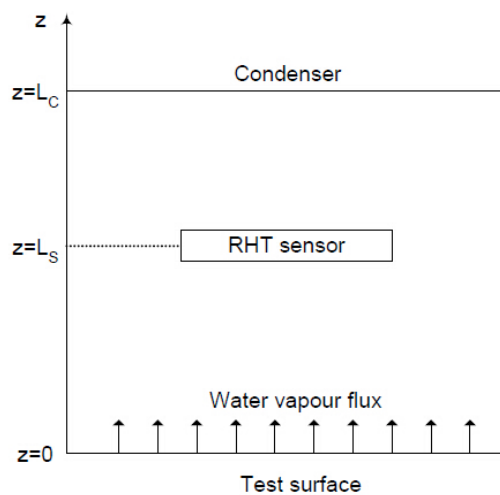As mentioned above, the internal space of the measurement chamber is small enough to suffocate natural convection and other bulk air movement. Therefore, diffusion is the only transport mechanism available, so bulk air movement is ignored, and thus, the migration of the water molecules in the chamber can be calculated using Fick's first law of diffusion:

$$J = -D_{VA} \frac{\partial H}{\partial z} \tag{2.5}$$

where $J$ is the water vapour flux density from the sample surface, $D_{VA}$ is the molecular diffusion coefficient for water vapour in air ($D_{VA} = 2.42 \times 10^{-5} m^2/s$ at room temperature 20$^o$C), and H is the water vapour humidity.

Similarly, the temperature transfer is expressed as:

$$Q = -K_A \frac{\partial \theta}{\partial z} \tag{2.6}$$

where $Q$ is the heat flux density, $K_A$ is the thermal conductivity of air, and $\theta$ is the temperature distribution in the chamber.

Immediately after the vapour enters the chamber from the sample, it will be removed by the condenser. The steady-state vapour distribution is established. The steady-state solution is characterized by the constant water vapour humidity gradient $\frac{\partial H}{\partial z}$ in the chamber, whence the water vapour flux density from the sample surface. Therefore,

$$J = D_{VA} \frac{H(z) - H(L_C)}{L_C - z} \tag{2.7}$$

In the AquaFlux measurements, the water vapour humidity $H(z)$ is calculated using the following equations.

$$H(z) = \chi \rho_{VE}(\theta_z) \tag{2.8}$$

where $\chi$ is the fractional RH value, $\rho_{VE}(\theta)$ is the equilibrium vapour density at temperature $\theta$, and $\theta_z$ is the temperature at position z.

Then Eq. (2.8) can be rewritten as:

$$J = \frac{D_{VA}}{L_C - z}\left[\chi_z \rho_{VE}(\theta_z) - \chi_C \rho_{VE}(\theta_C)\right] \tag{2.9}$$

where $\chi_z$ and $\chi_C$ are the fractional RH values at $z$ and at the condenser respectively, $\theta$ and $\theta_C$ are the temperatures at $z$ and at the condenser respectively, and $\rho_{VE}(\theta_z)$ and $\rho_{VE}(\theta_C)$ are the equilibrium vapour densities at $z$ and at the condenser respectively.

Due to the thermodynamic equilibrium between the vapour phase near the condenser and the solid phase at the condenser (ice), $\chi_C = 1$ at the condenser. The Eq. (2.9) can be simplified as:

$$J = \frac{D_{VA}}{L_C - z}\left[\chi_z \rho_{VE}(\theta_z) - \rho_{VE}(\theta_C)\right] \tag{2.10}$$

Some extreme cases of the above equation are important for the AquaFlux measurements. When $z = L_s$, Eq. (2.9) is rewritten as:

$$J = \frac{D_{VA}}{L_C - L_S}\left[\chi_S \rho_{VE}(\theta_S) - \rho_{VE}(\theta_C)\right] \tag{2.11}$$

where $\theta_S$ and $\chi_S$ are the temperature and the fractional RH value at the RHT sensor respectively, and above equation allows the flux density to be determined from measurements of $\chi_S, \theta_S$ and $\theta_C$.

When $z = 0$, Eq. (2.10) becomes:

$$J = \frac{D_{VA}}{L_C}\left[\chi_0 \rho_{VE}(\theta_0) - \rho_{VE}(\theta_C)\right] \tag{2.12}$$

where $\theta_0$ and $\chi_0$ are the temperature and the fractional RH value at the sample surface.

20

The above equation specifies the microclimate immediately above the sample surface. With $J$ calculated from Eq. (2.11), the fractional RH value at the sample surface can be calculated.

Comparing with other water vapour flux density measurement instruments, such as Tewameter (Courage + Khazaka Electronic GmbH, Germany), Delfin VapoMeter (Delfin Technologies, Finland) and Evaporimeter (Cortex Technology ApS, Denmark), AquaFlux has many advantages, for example, high sensitivity, low noise, super reliability, excellent calibration ability and comparability, and above all, the measurement results are independent of external environment. AquaFlux can be used in the following areas [21-23]:

(1) Skin barrier function, skin recovery, skin disease etc., based on TEWL (Trans-Epidermal Water Loss) measurements.

(2) Membrane penetration and permeation.

(3) Material absorption/ desorption.

## 2.3 Capacitive Contact Imaging Based on Fingerprint sensor

The water content within human skin is very important for its cosmetic properties and its barrier functions; however, to measure it is very difficult. There are some disadvantages of the commercial skin hydration measurement devices, such as, poor repeatability, reproducibility and difficult to calibrate. To address these issues, a novel hand-held probe for in-vivo skin hydration imaging using capacitive Fingerprint sensors has been developed by the research group. It is based on capacitance measurement principle of capacitors.

Commonly, a capacitor is used to store (hold) the electrical charge. A capacitor is constructed of two conductive parallel plates separated by a non-conductive medium

or the dielectric region. Assuming that the parallel plates are charged with $+Q$ and

$-Q$ and that the voltage between the plates is $V$, the capacitance can be shown as:

$$C = \frac{Q}{V}$$     (2.13)

The unit of measurement used for measuring capacitance is farad, where 1 farad is equal to 1 coulomb per volt [24].

The capacitor stores energy which is equal to the energy required to charge it and thus electrical energy is not dissipated.

If a small element of charge $(dq)$ is moved across the two plates against the potential difference $V = q/C$; it will require the amount of energy $dW$:

$$dW = \frac{q}{C} dq$$     (2.14)

This energy fluctuates depending on the interference of the dielectric medium.

Fingerprint sensors [25, 26] are based on the capacitance fringing field measurement principle. The parallel plates of capacitor are split to a coplanar position; the fringing electric field will continue to create a field between the two plates, see Figure 2.6.
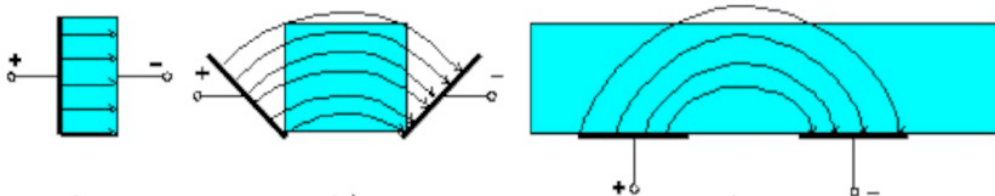


**Figure 2.6** *Two parallel capacitor plates are moved into coplanar position with fringing electric fields. Reproduced from [24]*

Each set of a parallel plate is regarded as a cell and each cell in turn contains a feedback capacitance known as a sensor plate. After a side--by--side array of alternating charged and sensor conductor plates are created, the alternating plates form the two plates of the capacitor. Meanwhile, any interference in between the plates causes the dielectric fields to change between the conductor plates. One set of conductor plates makes a single cell whose size is larger than the width of one ridge on the skin. The print image is created when the sensor detects variance in dielectric constants between the two.

Each set of the conductor plates (or cells) contains their own electrical circuit which the electrical circuit creates an inverting operational amplifier that alters the voltage being supplied thus making them tiny groups of semiconductor chips. The altered voltage is connected to the inverting terminal input and the non--inverting terminal input is relative to a reference voltage supply and a feedback loop. This feedback loop is in turn connected to the amplifier output which includes two conductor plates.

Fingerprint sensor is non-invasive, quick, simple to use, imaging based and is based on latest fingerprint sensor technologies and using well researched mathematical imaging processing algorithms. Compared with thermal sensors, capacitor technology offers better image quality with a wider range of operating conditions. It can measure any part of the body, and generate $256 \times 300$ pixels black and white skin capacitance images with a $50 \mu m \times 50 \mu m$ special resolution. In each image, each pixel is represented by an 8 bit grayscale value, 0~255, with 0 represents white (i.e. dry skin - low capacitance) and 255 represents black (i.e. wet skin- high capacitance).

The prototype of capacitive contact imaging based on Fingerprint sensor shown in Figure 2.7 has many functions [25, 26]:

(1) By processing those capacitive skin images using a dedicated software programme with purposely designed mathematical algorithms, we can produce skin hydration images, skin micro relief images and skin 3D surface profile images.

(2) It can also be used for study soft materials.

(3) It can also be used to study solvent membrane penetrations. Apart from water, Fingerprint sensor is also sensitive to many the solvents using in pharmaceutical studies.
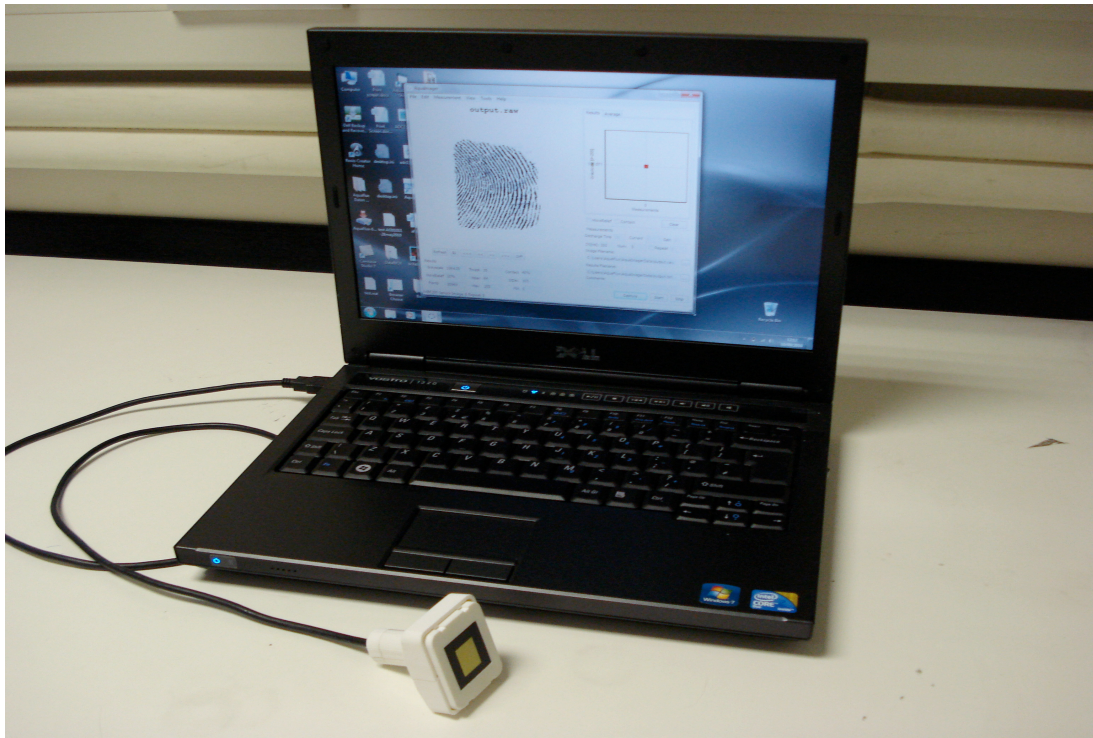


**Figure 2.7** *The prototype of capacitive contact imaging based on Fingerprint sensor*

## 2.4 Conclusions

In summary, OTTER is an infrared remote sensing technique for the Non-Destructive Examination (NDE) of sample surfaces, through their optical and thermal properties. AquaFlux is a novel technology for measuring water vapour flux density from

arbitrary surfaces and capacitive contact imaging based on Fingerprint sensor is a novel fringing field capacitive imaging technique, which can be used both for water measurements, as well as solvent measurements. It is a potentially very useful tool for studying solvent penetrations through membranes or skin.

# Chapter 3 Content-based Image Retrieval Using 2D Gabor Wavelet Texture Feature

Skin imaging plays a key role in many research areas, such as dermatology, clinical analysis, pharmacology and cosmetic science. In our research, many different imaging technologies have been used, including standard digital camera, Dermilte Dermoscopy, Proscope HR microscope and capacitive contact imaging based on Fingerprint sensors [27-30]. As more and more skin images are added to databases and there is clearly a need for effective and efficient image retrieval systems. Content-based image retrieval (CBIR) [31] is a useful technology to retrieve stored images from the database by supplying query images. In a typical CBIR, images are retrieved based on color, shape, and texture, etc. In this chapter, texture feature is used for retrieving images, and 2D Gabor wavelet transform, which is an important and promising method, is used for texture feature description and extraction. The results show that the 2D Gabor wavelet texture features can work efficiently on human face images, skin medical images and skin capacitive images generated by capacitive Fingerprint sensor.

## 3.1 The theory of 2D Gabor wavelet transform

In image processing, texture generally refers to the structures consisting of large numbers of texture elements or models similar to each other; it is a key component for human visual perception and plays an important role in image-related applications. Meanwhile, texture features have been researched in the content-based image retrieval, image classification and segmentation. Gray-level co-occurrence matrix [32], Tamura texture feature [33], and Gabor wavelet texture feature [34, 35] are the conventional

methods used to describe texture feature. Compared with other techniques, Gabor wavelet texture feature is computationally simpler, and image analysis using Gabor wavelet transform is similar to perception in the human visual system [36]. Gabor wavelet transform has been used in optical character recognition, iris recognition and fingerprint recognition. This chapter describes an image retrieval technique based on Gabor wavelet texture feature.

### 3.1.1 Wavelet Transform

It is well know that the Fourier transform has been the most commonly used tool for analyzing frequency properties of a given signal. However, this transformation is a global transformation, with some limitations, namely, after transformation, the information about time is lost and it is hard to tell where a certain frequency occurs. To solve this problem, the wavelet transform [37, 38] which is a kind of time-frequency analysis techniques was developed by the geophysicist Jean Morlet in 1981. Wavelet transform could extract both the time (spatial) and frequency information from a given signal, and the tunable kernel size results in different time-frequency resolution pairs. For example, bigger kernel size has higher resolution in frequency domain but lower resolution in time domain, and is used for lower frequency analysis. Smaller kernel size (in time domain) has higher resolution in time domain but lower resolution in frequency domain, and is used for higher frequency analysis. This great property makes wavelet transform useful for many image processing tasks. In other words, the image can be seen under the lens with a magnification given by the scale of a wavelet. This great character also makes wavelet transform suitable for applications such as image edge detection, filter design, and some kinds of image object recognition, etc.

Wavelets, as the name suggests, are 'little waves'. If a single real valued function $\psi(t) \in L^2(R)$, namely, $\psi(t)$ must satisfy the admissibility condition:

$$\int_0^\infty \frac{|\psi(\omega)|^2}{\omega} d\omega < \infty$$

(3.1)

where $\psi(\omega)$ denotes the Fourier transform of $\psi(t)$ and $L^2(R)$ represents the space of finite- energy (also known as square – integral) functions.

Then the function $\psi(t)$ is called the basic wavelet or mother wavelet.

Once one has a mother wavelet, one can then generate wavelets by the operations of dilation and translation as follow:

$$\psi_{s,\tau}(t) = s^{-1/2} \psi(\frac{t-\tau}{s})$$
$$s, \tau \in R \; s > 0$$

(3.2)

where $s$ is dilation parameter and $\tau$ is translation parameter.

### 3.1.2 *Gabor Wavelet Transform*

Gabor wavelet transform is a wavelet transform and among the different kinds of wavelet transforms, the Gabor wavelet transform has some impressive mathematical and biological properties and has been used frequently in image processing research. J. G. Daugman found that simple cells in the visual cortex of mammalian brains can be modeled by Gabor functions, see figure 3.1 [35]. Gabor wavelet transform can extract the relevant textural feature at different scales and directions in the frequency domain [39]. It is widely used to extract texture features from images for image retrieval and has been shown to be very efficient [40- 44].
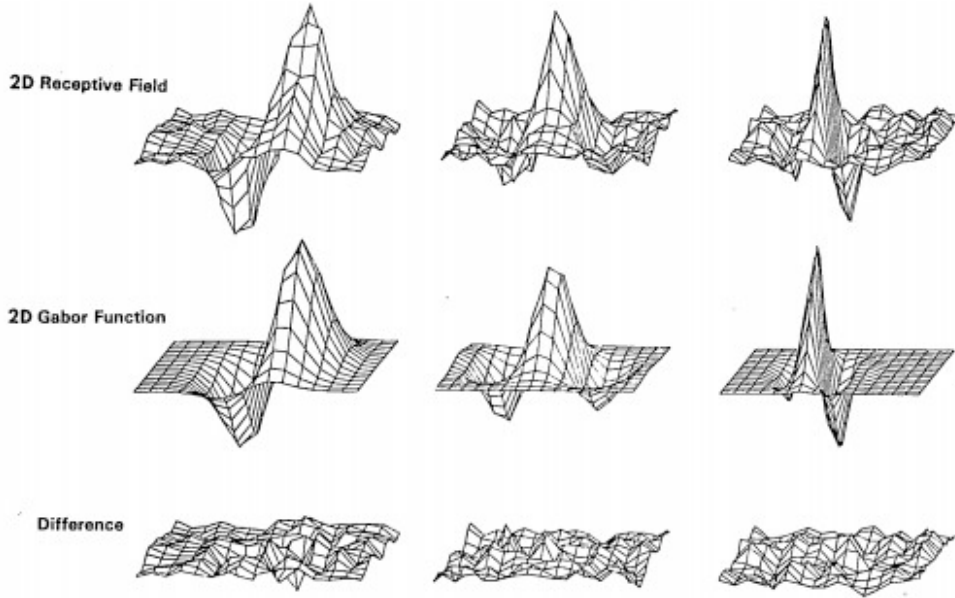
**Figure 3.1** *Top row: illustrations of empirical 2-D receptive field profiles measured by J. P. Jones and L. A. Palmer (personal communication) in simple cells of the cat visual cortex. Middle row: best-fitting 2-D Gabor elementary function for each neuron, described by (IO). Bottom row: residual error of the fit, indistinguishable from random error in the Chi- squared sense for 97 percent of the cells studied [35].*

Gabor wavelet transform has a good joint resolution in both spatial and frequency domain. It is well known that there is always uncertainty [45] between the time and the frequency resolution, namely, when the time duration gets larger, the bandwidth becomes smaller. Among various wavelet bases, the Gabor function is proved to achieve the lower bound optimally the optimal in the sense of minimizing the joint two-dimensional uncertainty in space and frequency.

The typical 2D Gabor function can be expressed as the product of Gaussian function and sinusoidal function [44, 46]:

$$g(x, y) = \left[ \frac{1}{2\pi\sigma_x\sigma_y} e^{-\frac{1}{2}\left( \frac{x^2}{\sigma_x^2} + \frac{y^2}{\sigma_y^2} \right)} \right] \times \left( e^{2\pi j f x} \right) \qquad (3.3)$$

where $\sigma_x$ and $\sigma_y$ are the Gaussian variance, which describe the spreads of the Gaussian function, $j$ is the imaginary part of complex number, $f$ is the frequency of the sinusoidal function. Using Eq. 1 as the mother function, we can generate a set of child functions, called Gabor wavelets.

$$g_{mn}(x,y) = a^{-m} g(x',y') \quad a > 1, m,n = \text{Integer}$$

$$x' = x\cos\theta + y\sin\theta$$
$$y' = -x\sin\theta + y\cos\theta$$

$$(3.4)$$

where $\theta = n\pi / K$, *n = 0, 1, …, K-1*, and $K$ is the total number of the directions which specifies the orientation of a Gabor function; *m = 0, 1, …, S-1,* and *S* is the number of scales which specifies the amplitude of a Gabor function. If we use $(U_l, U_h)$ to denote the lower and upper center frequency of the sinusoidal function, we have

$$a = \left(\frac{U_h}{U_l}\right)^{\frac{1}{S-1}}$$

$$f = U_h$$

$$(3.5)$$

Figure 3.2 shows typical 2D Gabor wavelet profile with different directions and scales.

(A)    Gaussian function            Sinusoidal function            Gabor function
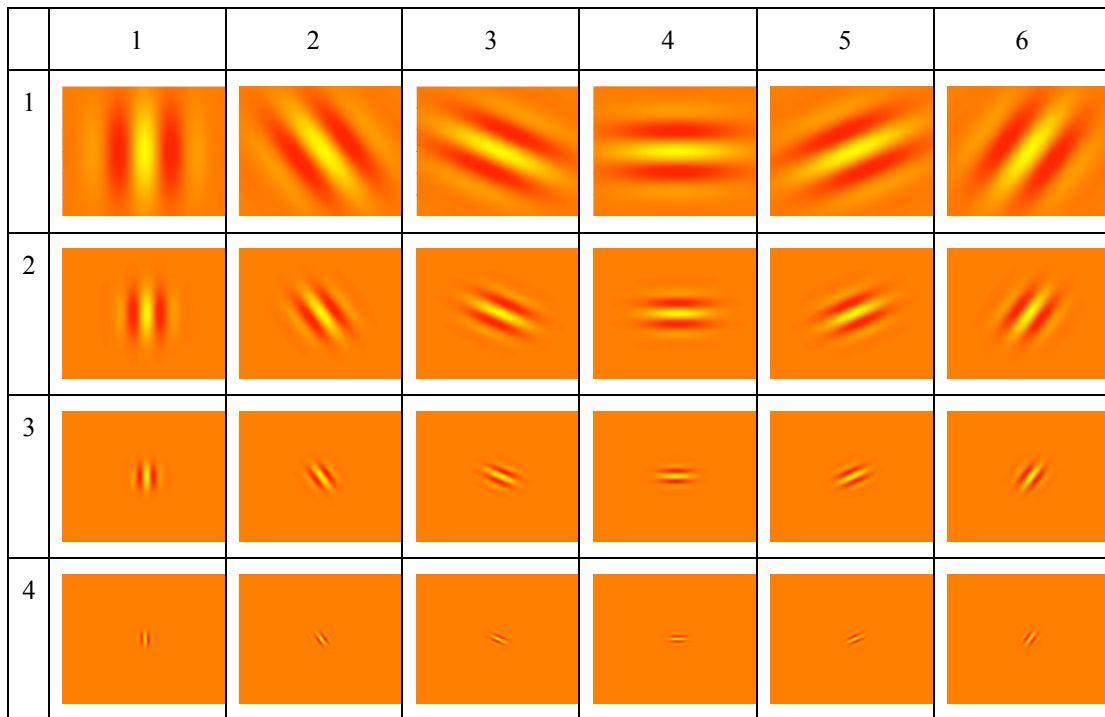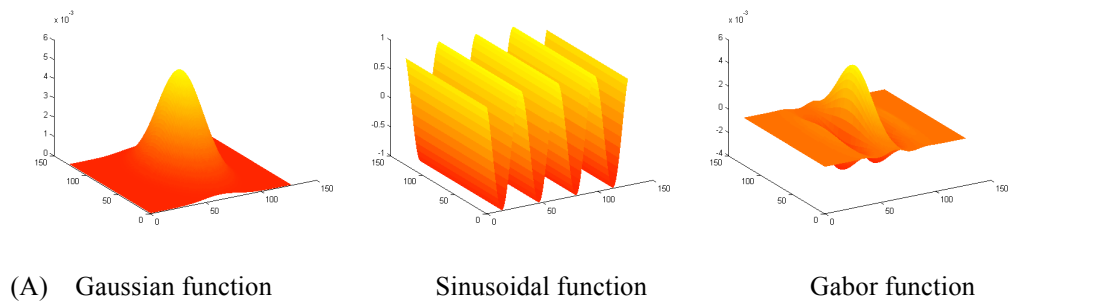


(B) Top view of 2D Gabor wavelet profiles at 6 different directions (columns) and 4 scales (rows).

**Figure 3.2** *2D Gabor wavelet profile with different directions and scales (A) shows profiles of Gaussian function, sinusoidal function and the corresponding wavelet function; (B) shows the 2D Gabor wavelet profiles at 6 different directions and 4 different scales.*

Image feature extraction based on 2D Gabor wavelet transform is introduced as follows [44, 47]:

**A: Transform the colour images into gray images.**

**B: Process the image by applying the Gabor wavelet transform.**

Gabor wavelet transform can be considered as a wavelet transform whose mother wavelet is Gabor function. For a given image $I(x, y)$ with $M \times N$ pixels, its Gabor wavelet transform is defined as follows:

$$W_{mn}(x, y) = \int I(x_1, y_1) g_{mn} * (x - x_1, y - y_1) d_{x_1} d_{y_1} \tag{3.6}$$

where * represents the complex conjugate.

In this chapter, $U_l$ and $U_h$ used are 0.05 and 0.4, the total number of directions (K) and scales (S) and have chosen to be $K = 6$ and $S = 4$, respectively, which is resulting 4x6=24 Gabor wavelet filters to filter the images. The values of scales (S) and directions (K) in Gabor wavelet transform not only affect the accuracy of retrieval, they also affect the computational time of program. More discussions on the choices of S and K, as well as $U_l$ and $U_h$, can be found in section 3.2.2 and 3.2.3 later in this chapter.

**C: Find the mean and standard deviation as a texture feature.**

An array of magnitudes, which represent the energy content at different scales and directions of the image, can be obtained after applying Gabor wavelet filters on the image with different directions and different scale,

$$E(m, n) = \sum_x \sum_y |W_{mn}(x, y)| \tag{3.7}$$

The mean $\mu_{mn}$ and the standard deviation $\sigma_{mn}$ of the magnitude of the transform coefficients are used to indicate the region for classification and retrieval purposes:

$$\mu_{mn} = \frac{\sum_x \sum_y |W_{mn}(x, y)|}{M \times N}$$

$$\sigma_{mn} = \sqrt{\frac{\sum_x \sum_y \left( \left| W_{mn}(x,y) \right| - \mu_{mn} \right)^2}{M \times N}} \tag{3.8}$$

**D: Get the feature vector F.**

A feature vector F is created using $\mu_{mn}$ and $\sigma_{mn}$ as the feature components. In this paper, scales S and directions K are set to 4 and 6, so the feature vector defined as follows:

$$\bar{f} = \left[ \mu_{00} \sigma_{00} \mu_{01} ... \mu_{35} \sigma_{35} \right] \tag{3.9}$$

Figure 3.3 is the flowchart of Gabor filter feature extraction. S and n specify which Gabor filter is selected.
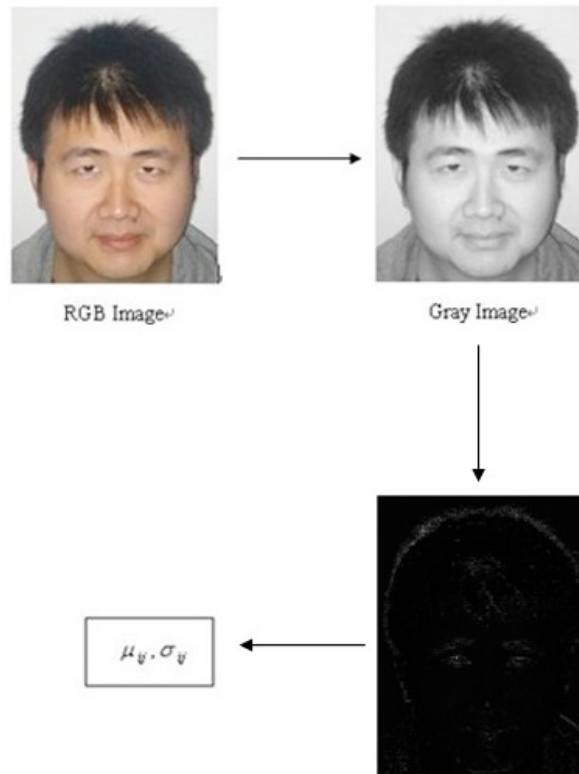


*Figure 3.3* *The flowchart of Gabor feature extraction.*

**E: Similarity Measure.**

Distance measurement and correlation measurement are the two main image similarity measurements. In this chapter, distance measurement is used only. The distance between the query images $i$ and the target image $j$ in the database is defined by:

$$d(i,j) = \sum_m \sum_n d_{mn}(i,j) \tag{3.10}$$

where

$$d_{mn}(i,j) = \left| \frac{\mu_{mn}^{(i)} - \mu_{mn}^{(j)}}{\alpha(\mu_{mn})} \right| + \left| \frac{\sigma_{mn}^{(i)} - \sigma_{mn}^{(j)}}{\alpha(\sigma_{mn})} \right| \tag{3.11}$$

$\alpha(\mu_{mn})$ and $\alpha(\sigma_{mn})$, which are used to normalize the individual feature components, are the standard deviations of the respective features over the entire database.

## 3.2 Results and Discussions

All the skin images used in this study were taken by using standard digital camera and capacitance based Fingerprint sensor, except the skin cancer and skin disease images, which were from Skin Cancer page of About.com [48]. Standard digital camera used is SONY DSC--W55 model, which has a 7.2 Mega Pixels with 3X optical zoom. A Matlab programmer has been developed to implement the Gabor wavelet transform for analyzing the skin images, and a Matlab Graphic User Interface (GUI) was also developed to simplify the operations. As the first step to evaluate the algorithm, a database containing fifty-six images are used in this study, the database images are in JPEG format, including six different digital colour human face images, four different digital colour skin cancer images, four different digital colour skin disease images and the rest of them are skin texture grey capacitive images which were captured from Fingerprint sensor [48]. Figure 3.4 shows some sample images from the database.
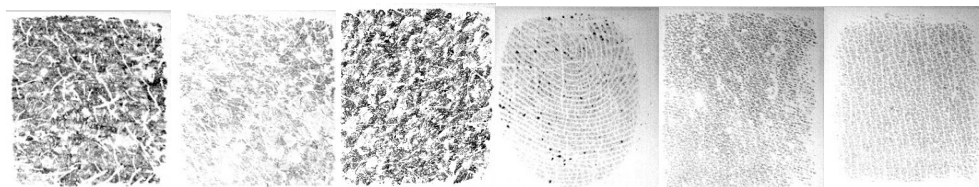
Faces
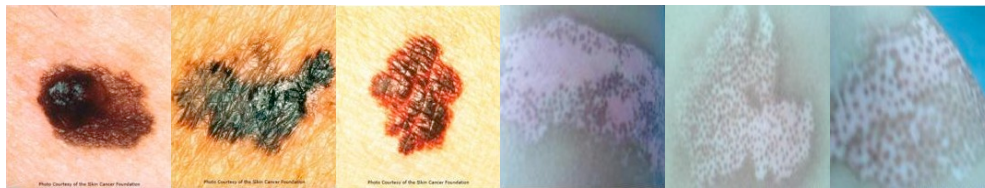


Skin cancers          Skin diseases



Capacitive skin images

**Figure 3.4** *Sample images from the database*

### 3.2.1. Image query results

Figure 3.5 shows the GUI for preliminary results on image retrieval using Gabor texture features. In all the four retrieval results shown, the upper left image in the first row is the query image and the others in the second row are the results of retrieved images from the image database. The best three retrieved images are shown for illustration. The retrieved images are ranked in descending order according to the similarity of their Gabor texture features to those of the query image, i.e. the most similar, the second similar, and the third similar images. In this study, for reasons of simplicity, the query images are also from the database, and therefore the most similar result should always be the image itself.

In Figure 3.5 (a)-(g), the query images are grey capacitive skin images captured from finger, eye, face, forehead, neck, volar forearm and palm. The black spots are the areas that water is actively coming out of skin. As it can be seen, the three most similar images are all similar finger, eye, face, forehead, neck, volar forearm and palm grey capacitive images captured from Fingerprint sensor. Figure 3.5 (h) shows the retrieval result for a query image using a human face. Human face pictures in the database are with two different expressions – smile and non-smile. The most similar image is the same one. The second most similar image is the same person without smile and the third image is that another person without smile. It shows that this method has certain reference value for human face recognition. It might be also useful for facial expression recognition. Figure 3.5 (i) and (j) are the output of skin disease classification. The query image in Figure 3.5 (i) is a skin cancer picture of melanoma. From the illustration, the three most similar images are all skin cancer images. The query image in Figure 3.5 (j) is a skin disease picture of leucoderma. From the illustration, the three most similar images are all leucoderma images. The results show that Gabor wavelet transform could also be potentially used for skin disease diagnostics. Users could take a skin image, search the skin disease database, find out what possible type of skin disease it might resemble, and seek doctors for early diagnoses.
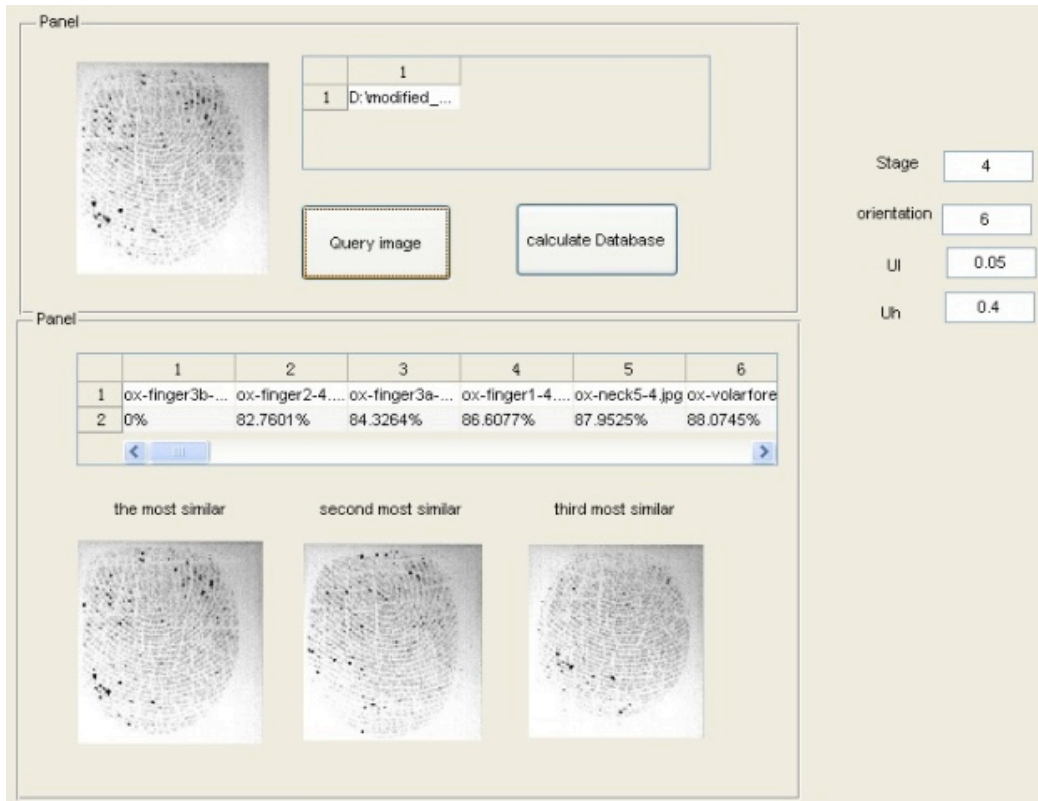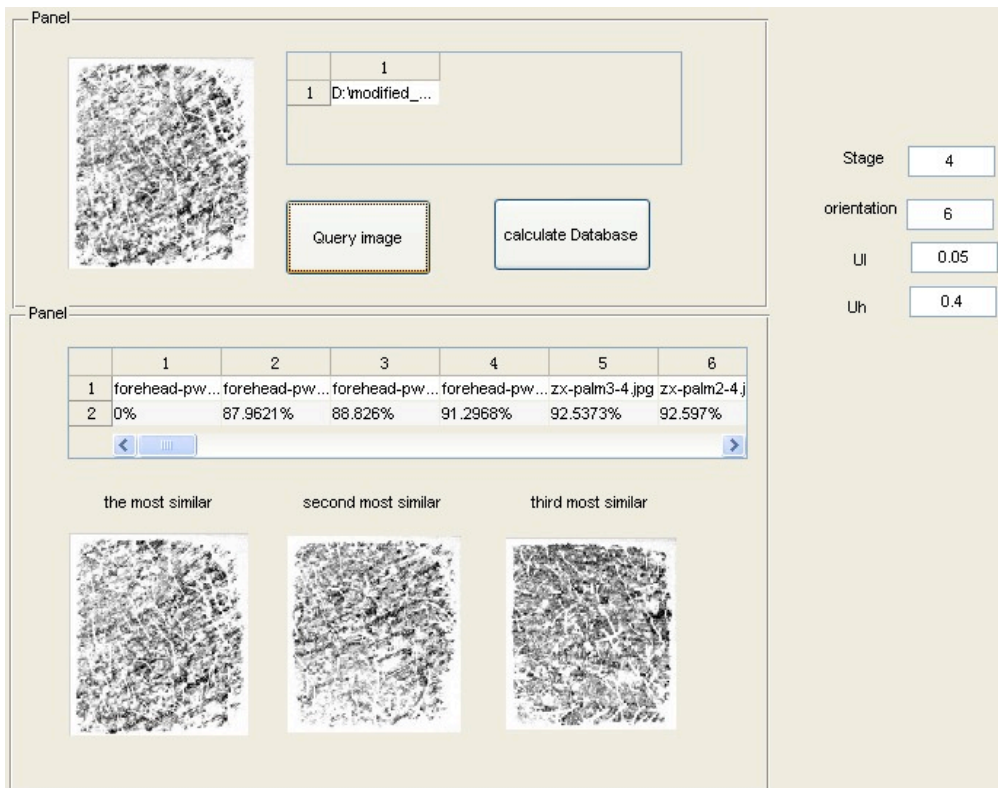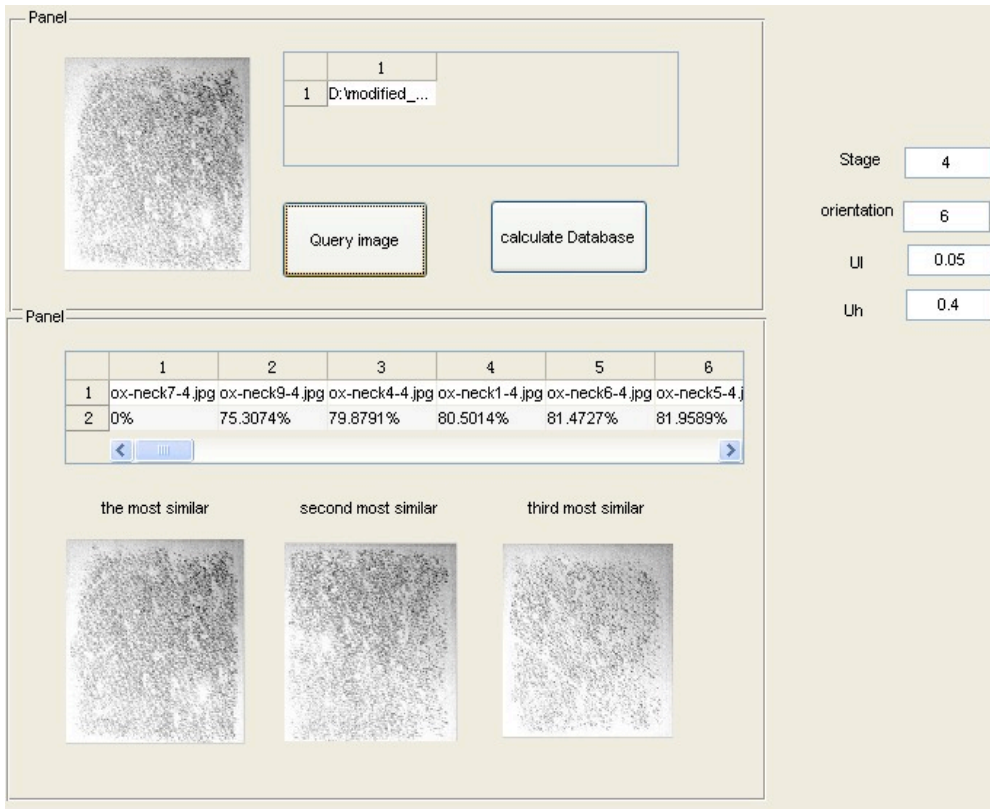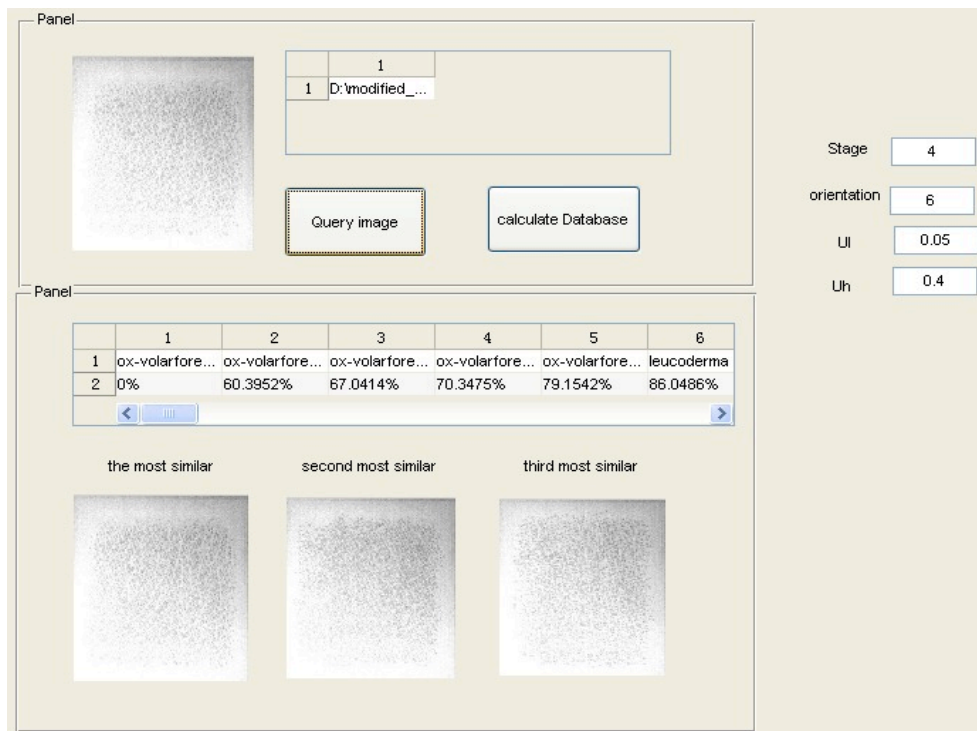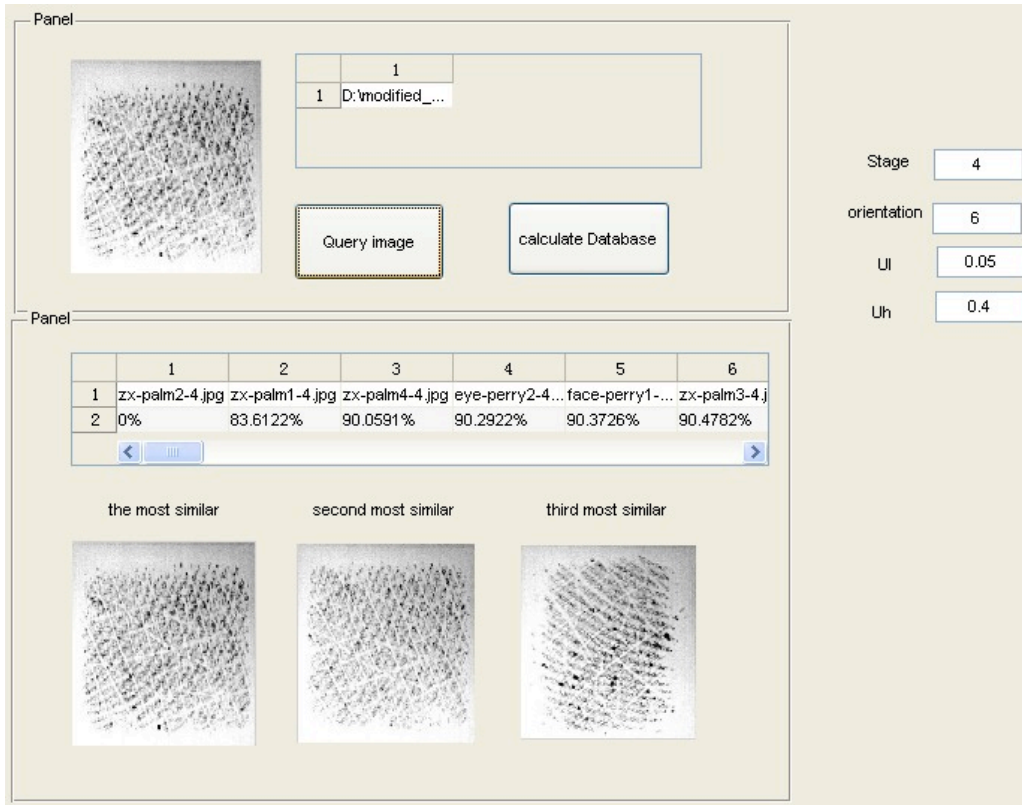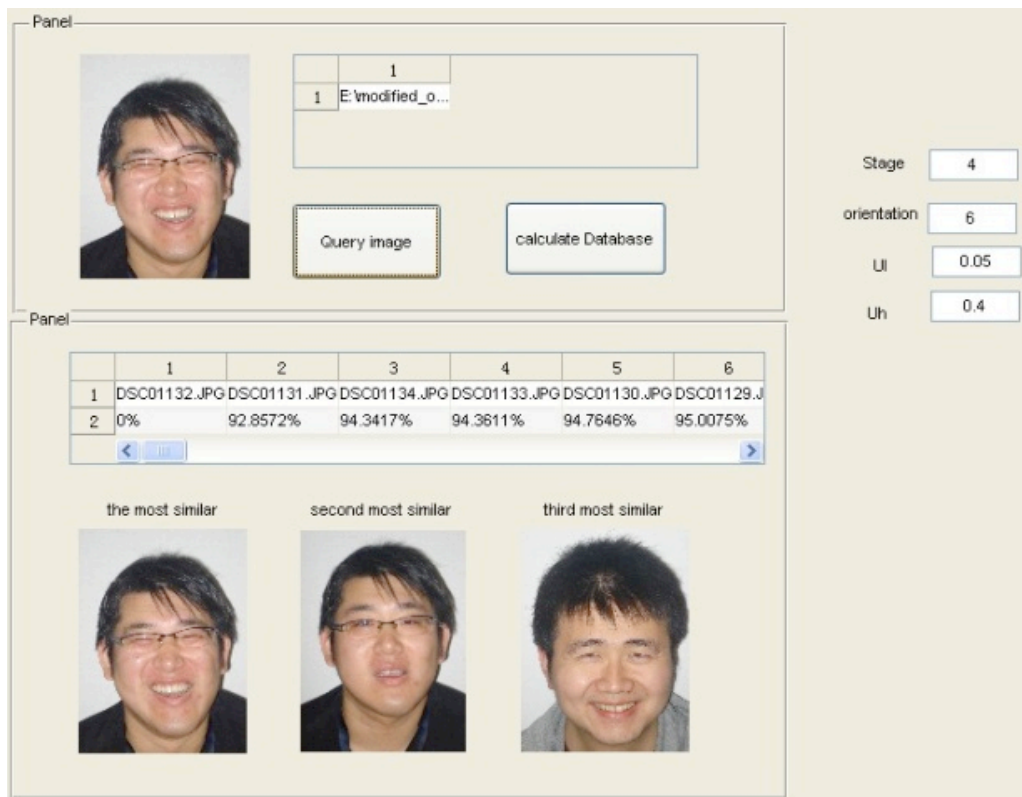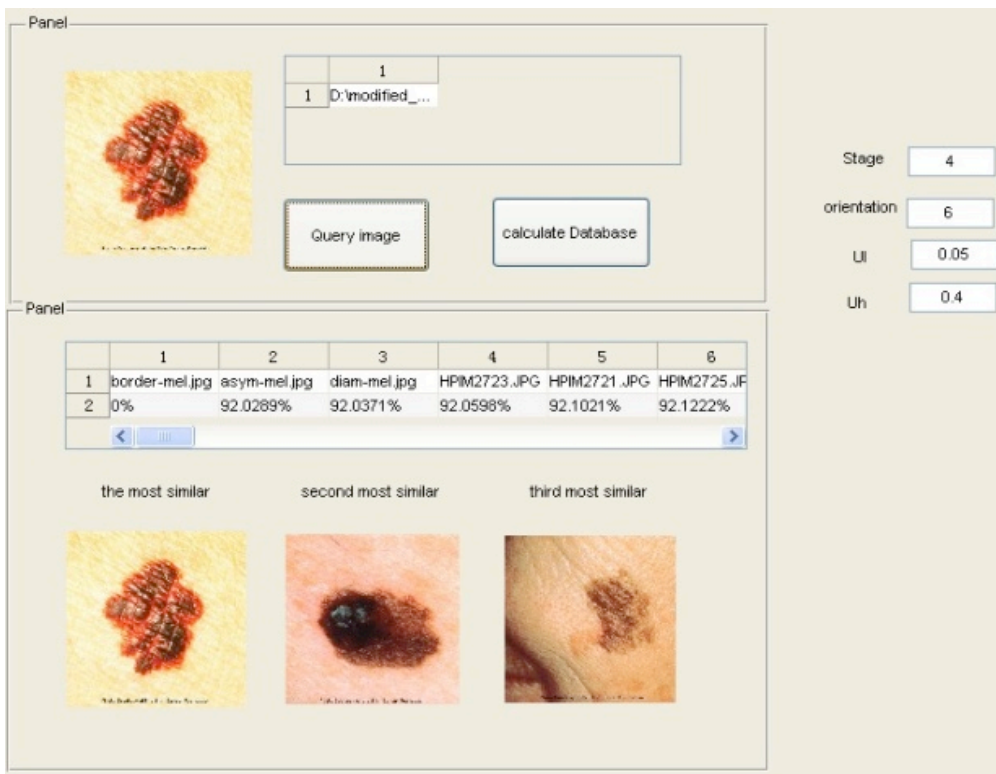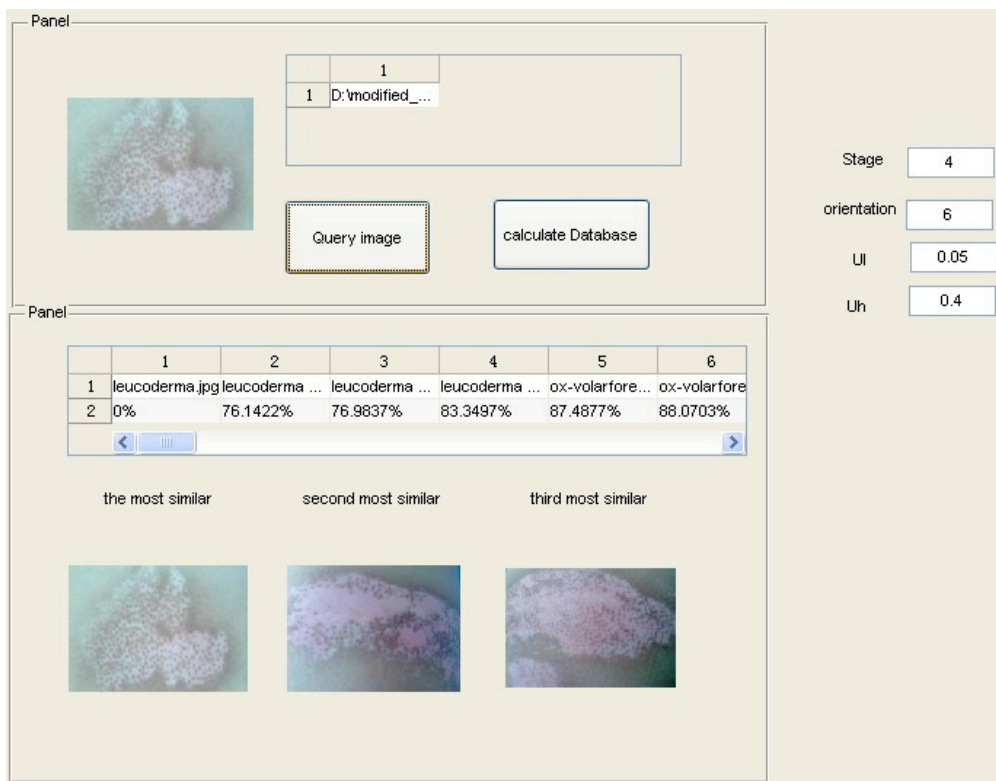
(a)
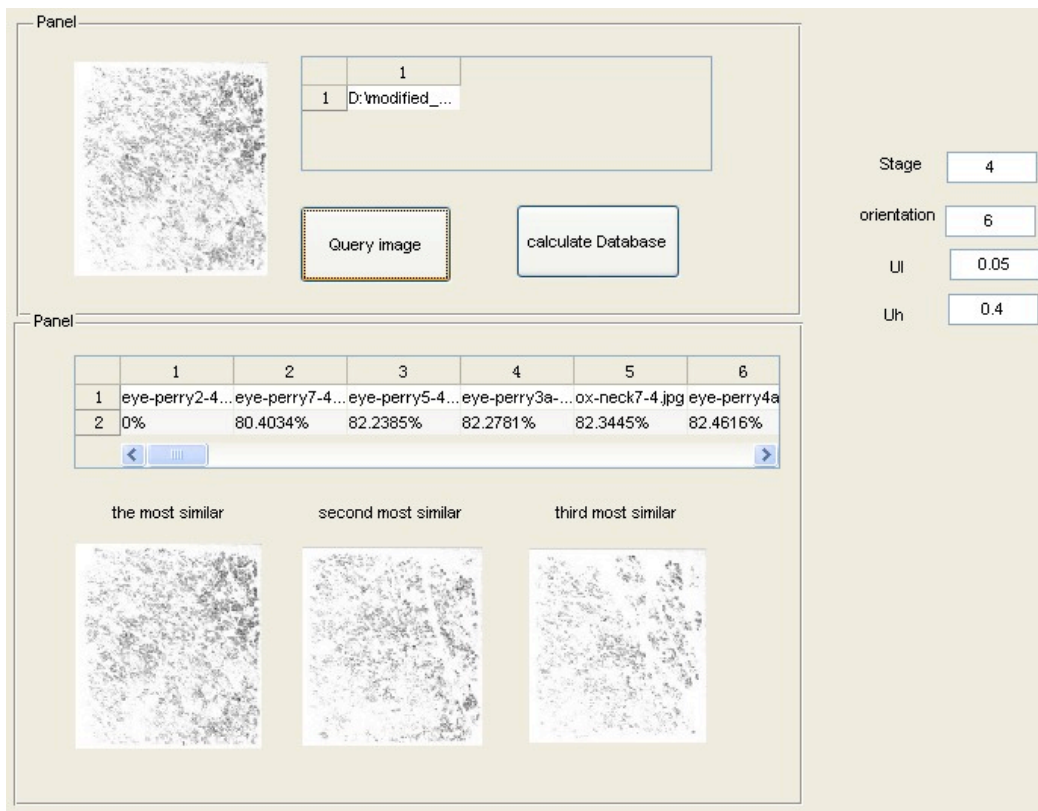


(b)
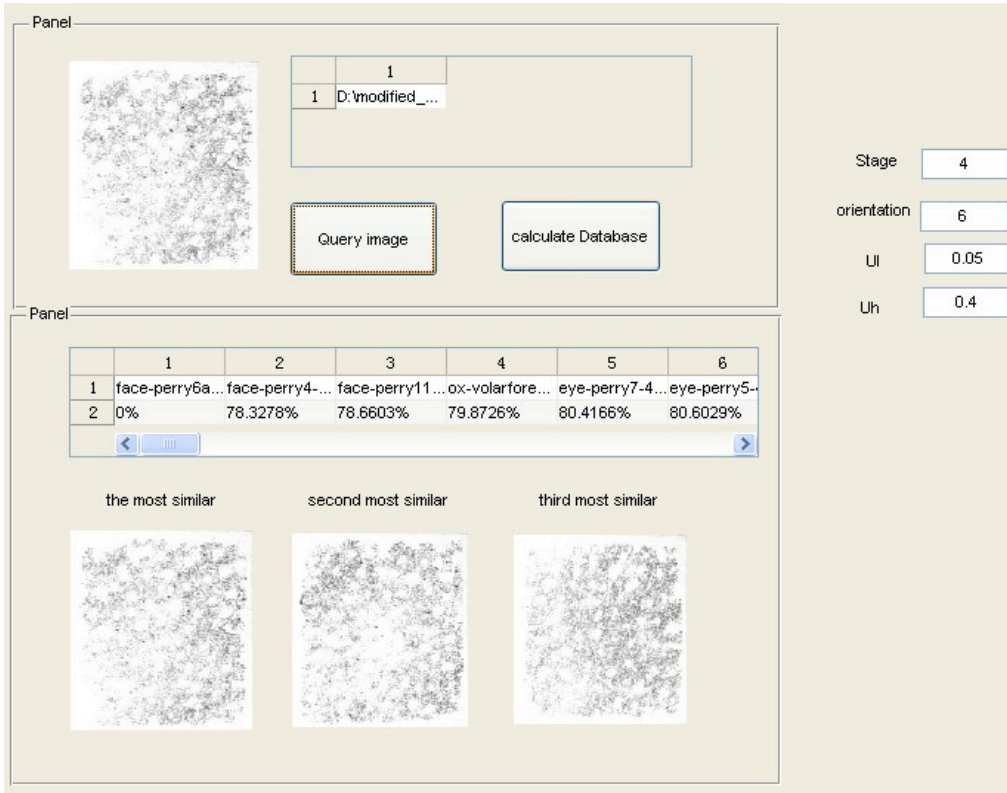
(c)



(d)

(e)



(f)

(g)



(h)

(i)



(j)

**Figure 3.5**Image retrieval results using Gabor texture features

*3.2.2. The effects of scales (S) and directions (K)*

The values of scales (S) and directions (K) in Gabor wavelet transform not only affect the accuracy of retrieval, they also affect the computational time of program. Figure 3.6(a) and (b) show typical retrieval errors and Figure 3.6 (c) shows the relationships between computational time and the production of scales and directions $(S \times K)$. If any of the best three results is not the right type of images, such as Figure 3.6 (a) or (b), we classify it as a retrieval error, and then we can plot the relationships between retrieval errors and $S \times K$, also shown in Figure 3.6 (c). Generally speaking, the higher the values of $S \times K$, the lower the retrieval errors, but the longer the computational time; the lower the values of $S \times K$, the shorter the computational time, but the higher the retrieval errors. The key is to find the optimum value of $S \times K$ that has highest accuracy, but the lowest possible computational time. From this study, it is found that setting scales and directions to 4 and 6 is a reasonable choice.

(a)                                              (b)
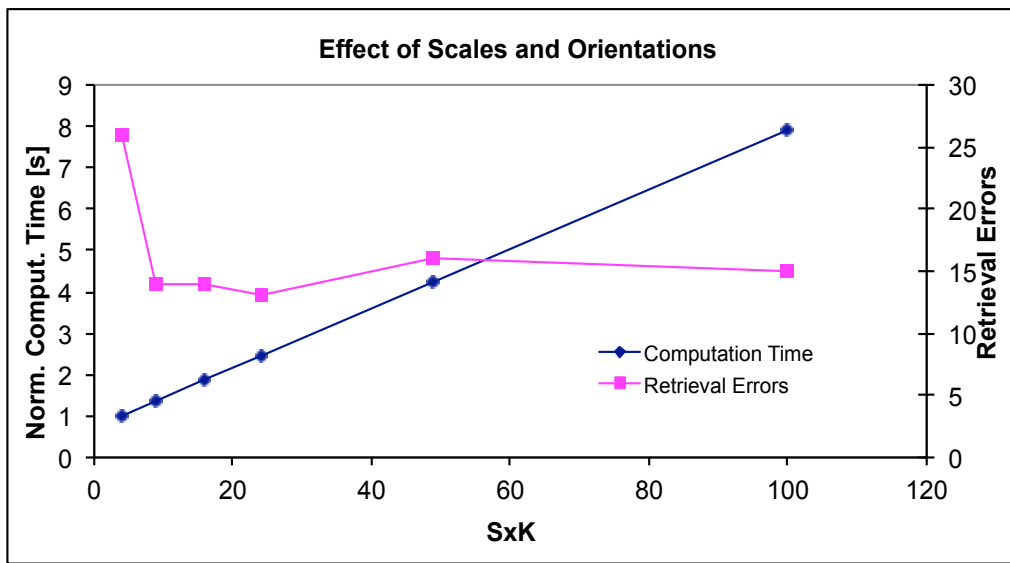


(c)

**Figure 3.6** *(a) and (b) are image retrieval errors, (c) is computational times and retrieval errors against the production of scales and directions $S \times K$.*

### 3.2.3. The effects of $U_l$ and $U_h$

Although the values of lower and higher center frequency $U_l$ and $U_h$ do not affect the computational time, they do affect the retrieval accuracy. In general, the values of $U_l$ and $U_h$ are set to 0.05 and 0.4 because the lowest frequency of image is 0 and the highest frequency of image calculated from Nyquist sampling theorem [49] is 0.5. According to the visual characteristics of the human eye, the frequency range from

43

0.05 to 0.4 can be completely reflected people's perception of texture features [50]. However, the retrieval results using these standard values shown in Figure 3.7 (a) are unsatisfactory because the query image in Figure 3.7 (a) is the neck grey capacitive image, but the third most similar image is the face grey capacitive image**.** By changing the value of $U_l$ and $U_h$ to 0.2 and 0.3 and the results shown in Figure 3.7 (b) become much better. From Figure 3.7, it can be concluded that the values of $U_l$ and $U_h$ might need to be adjusted differently to different type of images in order to have better retrieval accuracy.
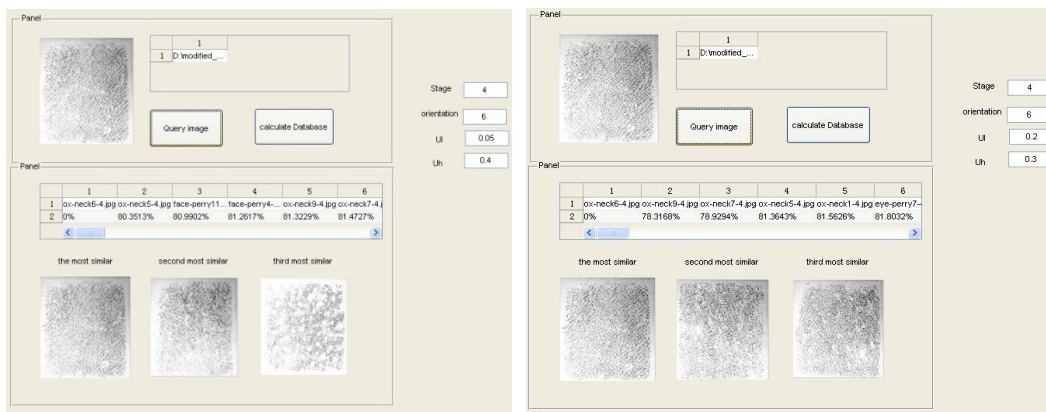


(a)                                         (b)

**Figure3.7** *Image retrieval results using Gabor texture features.*

### 3.2.4. Further discussions

In practical applications, there are many factors which will affect the accuracy of retrieval, for example, the same face image with different orientations, the same skin area with different location, the same skin with different lighting and at different days etc. In human face recognition, changing of people's face, such as, wearing glasses, eye closed, different hairstyles, will also increase the retrieval difficulty, which results in retrieval accuracy decreasing. In chapter 7, a detailed study which involves

retrieving human face images with different orientations will be presented.

## 3.3 Conclusions

In summary, an effective image retrieval method based on Gabor wavelet transform has been developed, and the effects of the parameters used in Gabor wavelet transform, e.g. the scales, directions, lower and higher center frequency, have been discussed. Experimental results show that Gabor wavelet transform can be used for retrieving different types of images, namely digital colour face images, digital colour skin cancer, skin disease images, and grayscale skin capacitive images. This suggests that using the Gabor wavelets to extract texture features could be potentially useful for human face recognition, facial expression recognition, skin cancer and disease diagnostics etc. The results also show that Gabor wavelet transform is particularly effective for retrieving grayscale skin capacitive images of the different parts of human body, which are very similar in texture.

# Chapter 4 In-Vivo Skin Capacitive Imaging Analysis by using Grey Level Co-occurrence Matrix (GLCM)

Skin capacitive contact imaging based Fingerprint sensors has shown potentials in skin hydration imaging, skin texture analysis, skin 3D surface profiles, and skin micro relief measurements [51- 55]. It is based on capacitance measurement principles, and the measurement results depend on the sample's dielectric constants. Our latest studies showed that apart from water, capacitive Fingerprint sensors are also sensitive to many solvents, due to their high dielectric constants. This makes the technique very useful for skin hydration, solvent penetrations, as well as in-vivo trans-dermal drug delivery studies [56, 57]. The aim of this chapter is to develop a new mathematical algorithm based on Grey level co-occurrence matrix (GLCM) to analyze the capacitive skin images, in order to extract information on skin texture and solvent penetrations. This chapter will first introduce the theoretical background of GLCM and then show some analysis results.

## 4.1 The Theory of Grey Level Co-occurrence Matrix (GLCM)

Grey level co-occurrence matrix (GLCM), proposed by Haralick in the 1970s [58- 60], is an image processing technique that has been widely used for measuring of texture in images. It first generates a grey level co-occurrence matrix that is defined as the distribution of co-occurring values at a given offset over a given image, and then calculates a set of textual features (usually called Haralick features) from the matrix that can reflect the image texture. There are 14 different textual features, but only 4 are independent [61], namely angular second moment (ASM), entropy (ENT), contrast (CON) and correlation (COR).

## 4.1.1 Grey Level Co-occurrence Matrix

Grey Level Co-occurrence Matrix (GLCM) [62- 65] provides a mature and effective statistical method for analyzing texture. It reflects the comprehensive information of the direction, adjacent interval and amplitude variations for image grey-level. For a given image I, the corresponding GLCM can be calculated by:

$$P(i,j,d,\theta) = \sum_{x=0}^{n} \sum_{y=0}^{m} \begin{cases} 1, if\ I(x,y) = i\ and\ I(x + d\cos\theta, y + d\sin\theta) = j \\ 0, otherwise \end{cases} \qquad (4.1)$$

where $P(i,j,d,\theta)$ in GLCM describes the probability with which two pixels separated by a particular displacement distance $d$ and a specified angle $\theta$ occur on the image, one with grey-level $i$ and the other with grey-level $j$. The following example is used to illustrate the process of calculation.

A 4 by 4 section **I** of an image having five grey-level intensities is showed below (vectors and matrices are indicated in bold).

$$I = \begin{bmatrix} 0 & 3 & 4 & 2 \\ 2 & 1 & 3 & 4 \\ 0 & 3 & 2 & 1 \\ 2 & 1 & 0 & 3 \end{bmatrix}$$

If an image contains G grey-levels from 0 to G-1, then the GLCM can be written as a G × G matrix. Consider I, a $5 \times 5$ matrix is formed and sequential numbers along the left (reference) and top (neighbor) are used to indicate them. A generalized GLCM for that image is shown in figure 4.1. The # (i, j) stands for number of times gray tones *i* and *j* have been neighbors satisfying the condition stated by displacement vector d. In this chapter, the distance *d* is considered as 1 i.e. only adjacent pixels are considered.

| Gray tone | 0 | 1 | 2 | 3 | 4 |
|---|---|---|---|---|---|
| 0 | #(0,0) | #(0,1) | #(0,2) | #(0,3) | #(0,4) |
| 1 | #(1,0) | #(1,1) | #(1,2) | #(1,3) | #(1,4) |
| 2 | #(2,0) | #(2,1) | #(2,2) | #(2,3) | #(2,4) |
| 3 | #(3,0) | #(3,1) | #(3,2) | #(3,3) | #(3,4) |
| 4 | #(4,0) | #(4,1) | #(4,2) | #(4,3) | #(4,4) |

***Figure 4.1*** *General form of GLCM*

For example, when angle $\theta$ is considered as 0º i.e. along the positive x-axis from left to right, 0 (reference) adjacent to 0 (neighbor) in **I** occurs 0 times, hence we put 0 at position (0, 0) of **G**, 1 adjacent to 0 occurs 1 times (rows 3) hence (1, 0) contains 1. This procedure is repeated for all pairs of intensities starting in the upper left corner and proceeding to the lower right:



$$G = \begin{bmatrix} 0 & 0 & 0 & 3 & 0 \\ 1 & 0 & 0 & 1 & 0 \\ 0 & 3 & 0 & 0 & 0 \\ 0 & 0 & 1 & 0 & 2 \\ 0 & 0 & 1 & 0 & 0 \end{bmatrix}$$

The texture calculation requires a symmetrical matrix. In order to get the GLCM into this form, the calculation should be moved along the −ve x-axis, i.e. we had looked from right to left, and then the matrix formed would have been the transpose matrix $G^T$. After adding transpose to the original, a symmetrical matrix, namely $S = G + G^T$ is generated:

$$G + G^T = \begin{bmatrix} 0 & 0 & 0 & 3 & 0 \\ 1 & 0 & 0 & 1 & 0 \\ 0 & 3 & 0 & 0 & 0 \\ 0 & 0 & 1 & 0 & 2 \\ 0 & 0 & 1 & 0 & 0 \end{bmatrix} + \begin{bmatrix} 0 & 1 & 0 & 0 & 0 \\ 0 & 0 & 3 & 0 & 0 \\ 0 & 0 & 0 & 1 & 1 \\ 3 & 1 & 0 & 0 & 0 \\ 0 & 0 & 0 & 2 & 0 \end{bmatrix} = \begin{bmatrix} 0 & 1 & 0 & 3 & 0 \\ 1 & 0 & 3 & 1 & 0 \\ 0 & 3 & 0 & 1 & 1 \\ 3 & 1 & 1 & 0 & 2 \\ 0 & 0 & 1 & 2 & 0 \end{bmatrix}$$

Before GLCM is used to extract the features, it should be normalized by dividing each element by the sum of all elements to form $S_0$.

The '0' in the subscript indicates angle $\theta = 0°$. There are another three directions: vertical ($\theta = 90°$), right diagonal ($\theta = 45°$) and left diagonal ($\theta = 135°$) generating matrices $S_{45}, S_{90}$ and $S_{135}$ which also can be computed:

$$S_0 = \frac{1}{24} \begin{bmatrix} 0 & 1 & 0 & 3 & 0 \\ 1 & 0 & 3 & 1 & 0 \\ 0 & 3 & 0 & 1 & 1 \\ 3 & 1 & 1 & 0 & 2 \\ 0 & 0 & 1 & 2 & 0 \end{bmatrix}$$



$$S_{45} = \frac{1}{24} \begin{bmatrix} 0 & 0 & 4 & 0 & 0 \\ 0 & 0 & 0 & 4 & 1 \\ 4 & 0 & 0 & 1 & 1 \\ 0 & 4 & 1 & 0 & 1 \\ 0 & 1 & 1 & 1 & 0 \end{bmatrix}$$



$$S_{90} = \frac{1}{16} \begin{bmatrix} 0 & 2 & 0 & 0 & 0 \\ 2 & 0 & 1 & 0 & 1 \\ 0 & 1 & 0 & 2 & 1 \\ 0 & 0 & 2 & 2 & 0 \\ 0 & 1 & 1 & 0 & 0 \end{bmatrix}$$

$$S_{135} = \frac{1}{18} \begin{bmatrix} 0 & 2 & 0 & 1 & 0 \\ 2 & 0 & 1 & 1 & 0 \\ 1 & 1 & 0 & 2 & 0 \\ 1 & 1 & 2 & 1 & 0 \\ 0 & 0 & 0 & 0 & 2 \end{bmatrix}$$

*4.1.2 Textural Features and Their Significance*

Four different GLCM feature vectors, i.e. angular second moment (ASM), entropy (ENT), contrast (CON) and correlation (COR) are selected to describe the skin texture, see Eq.(4.2) to Eq.(4.5) for their definitions:

$$ASM = \sum_{i=0}^{G-1} \sum_{j=0}^{G-1} \{\hat{P}(i,j,d,\theta)\}^2 \qquad (4.2)$$

Where $\hat{P}(i,j,d,\theta)$ represents normalized $P(i,j,d,\theta)$, and G is the total number of grey-levels.

$$ENT = - \sum_{i=0}^{G-1} \sum_{j=0}^{G-1} \hat{P}(i,j,d,\theta) \times \log\left(\hat{P}(i,j,d,\theta)\right) \qquad (4.3)$$

$$CON = \sum_{i=0}^{G-1} \sum_{j=0}^{G-1} (i-j)^2 \cdot \hat{P}(i,j,d,\theta) \qquad (4.4)$$

$$COR = \frac{\sum_{i=0}^{G-1} \sum_{j=0}^{G-1} ij\hat{P}(i,j,d,\theta) - \mu_1\mu_2}{\sigma_1^2 \sigma_2^2} \qquad (4.5)$$

Where $\quad \mu_1 = \sum_{i=0}^{G-1} i \sum_{j=0}^{G-1} \hat{P}(i,j,d,\theta)$

$$\mu_2 = \sum_{i=0}^{G-1} j \sum_{j=0}^{G-1} \hat{P}(i,j,d,\theta)$$

$$\sigma_1^2 = \sum_{i=0}^{G-1} (i - \mu_1)^2 \sum_{j=0}^{G-1} \hat{P}(i,j,d,\theta)$$

$$\sigma_2^2 = \sum_{i=0}^{G-1} (i - \mu_2)^2 \sum_{j=0}^{G-1} \hat{P}(i,j,d,\theta)$$

The angular second moment (ASM) [59, 66] is the squared sum of all the elements of GLCM, also called energy. ASM measures the texture uniformity, it can also reflect the thickness of skin micro relief lines, i.e. the thicker the micro relief lines, the higher ASM value, and the thinner the micro relief lines, the lower the ASM value [67].

The term entropy has originated in thermodynamics. In image processing, the entropy (ENT) [58, 59, 68] is a statistical measure of the disorder of an image, reflects the randomness of grayscale distribution. Its value achieves the largest when all elements in GLCM are as equal as possible and the smallest when some values are high and others low. The more dense the texture is, the more scattered the grayscale distribution, and the more small elements GLCM has. Hence the entropy value is higher.

The contrast (CON) [69- 71] is a measure of the amount of the local grey level variations in an image, which is the moment of inertia of the matrix around its main diagonal. Values on the GLCM main diagonal imply no contrast, and contrast value increases away from the main diagonal. The larger amount of the local grey level variations the image has, the higher the values for the GLCM elements which are further away from the main diagonal, so, creating a weight that increases as distance from the diagonal increases. Therefore, the contrast value is higher.

The correlation (COR) [69- 71] is a measure of grey level linear-dependencies in an image. This also reflects the degree of the rows (or columns) of the GLCM relative to

each other. For example, when the number of the textures in the horizontal direction is more than other directions, the value of the correlation feature is higher along this direction compared to the values for others.

*4.1.3 Preprocessing Images*

In this chapter, through using histogram equalization to increase image grayscale dynamic range, the contrast and sharpness of the image are improved and the detailed features of the image has also been better highlighted, which make subsequent processing easier, faster, more accurate and reliable. The principle of the histogram equalization is introduced as follows [72]:

In the image, let the variable r denote the intensities of an image to be processed and the range of r is from 0 to L-1, with r= 0 representing black and r= L-1 representing white. Let $P_r(r)$ represent the probability density function (PDF) of the intensity levels in a given image where the subscript is used for discriminating that the PDF belongs to input or the output images. The output intensity level s can be obtained through performing the following transformation on the input levels:

$$s = T_{(r)} = (L-1)\int_0^r p_r(w)dw = \frac{2}{L-1}\int_0^r wdw = \frac{r^2}{L-1} \qquad (4.6)$$

Where $w$ is a dummy variable of integration.

The discrete form for the equation (4.6) is:

$$s_k = T_{(r_k)} = (L-1)\sum_{j=0}^{k} p_r(r_j)$$

$$= \frac{(L-1)}{MN}\sum_{j=0}^{k} n_j \qquad k = 0,1,2,...,L-1 \qquad (4.7)$$

where MN is the total number of pixels in the image.

Through using equation (4.7) namely, mapping each pixel in the input image with intensity $r_k$ into a corresponding pixel with level $s_k$ in the output image, the input image is obtained. The transformation $T_{(r_k)}$ in this equation is called a histogram equalization or histogram linearization transformation.

### 4.1.4 Experimental Procedures

In this research, four sets of experiments are performed. The first experiment involves two healthy male volunteers whose age ranges are 20-30 years old and 40-50 years old respectively. The capacitive images are taken from their foreheads, eyes and cheeks, and each site is repeated six times.

The second experiment is solvent penetration through in-vivo skin combined with tape stripping. In this experiment, two solvents are used: undiluted dimethyl sulfoxide (DMSO) and undiluted ethylene glycol (EG), due to their relatively high dielectric constants compared with dry skin, as shown in Table 4.1. DMSO and EG are also chosen because they are commonly used in many cosmetic products.

Three different skin sites on the volar forearm of a healthy female volunteer (Asian, aged 29 and a mass of 56 kg) are selected, with one skin site is for DMSO, one for EG, and one is used as a control site. Before performing measurements, the volunteer was acclimatized for 20min, and each skin site was wiped clean with EtOH/water (95 %) solution. And then a small amount of solvent (～0.1 mL) is applied for 5min on each test skin site. After the test site is wiped dry, tape stripping is performed. Fingerprint sensor measurements are performed both before and after the solvent applications, and after each stripping. Tape stripping is repeated for twelve times.

| Materials | Skin | Water | DMSO | Ethylene Glycol |
|---|---|---|---|---|
| **Dielectric Constant** | 7 | 80.4 | 47.2 | 37 |

***Table 4.1*** *Dielectric Constants of the solvents and skin*

The third experiment is using Fingerprint Sensor to study the permeation ability of solvent. Six different solvents were selected for this test (Table 4.2).

.

| Solvent | Dielectric constant |
|---|---|
| Water | 80 |
| Ethanol | 24.55 |
| Butanol | 18 |
| Heptanol | 11.75 |
| Decanol | 8.1 |
| Propylene Glycol | 32.1 |

***Table 4.2*** *The dielectric constants for the used solvents*

A piece of membrane is fixed on the Fingerprint Sensor and a regular hexagonal sleeve is put on top of the membrane. After the sleeve is filled with solvents, measurements started for about 1000 seconds. Six different solvents were studied: butanol, decanol, heptanol, propylene glycol (PG), water and ethanol.

The fourth experiment is using Fingerprint Sensor to study the skin immersive hydration. Two different skin sites on the volar forearm of a healthy female volunteer (Asian, aged 31 and a mass of 56 kg) are selected, with one skin site is used as a test site and one is used as a control site. The skin test site is hydrated by soaking in room temperature water for 30 min. After the soaking, the test site is carefully wiped dry. The measurements are performed both before soaking and periodically after at both sites at 5min, 10min, 15 min, 20min and 30min.
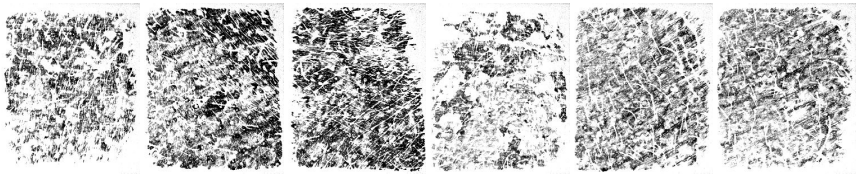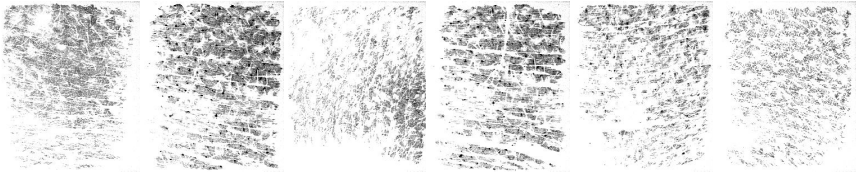
## 4.2 Results and Discussions
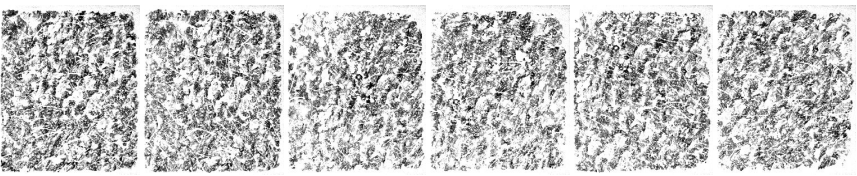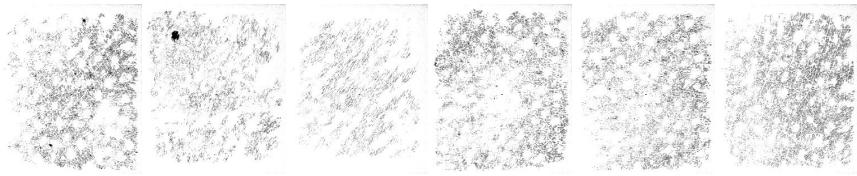
### 4.2.1 Experiment 1 – Different Skin Sites

Figure 4.2 shows the grey capacitive images on the skin sites of forehead, cheek and eye, from two male volunteer with different ages. Each skin site is repeated 6 times. Figure 4.3 shows the corresponding feature vector values, changing with age on the skin sites of forehead, cheek and eye.

The results show that the ASM values of the volunteer whose age range is 40-50 years old are bigger than the values of the volunteer whose age range is 20-30 years old, indicating the skin textures of the volunteer whose age range is 40-50 years old are coarser and thicker than another's. The results also show that the entropy values indicate the reverse trend between the two different volunteers, which indicates that the skin textures of older volunteer are sparser than the younger's. The contrast and correlations values show little changes between the two different volunteers.

**Forehead**

| Volunteer 1 |  |
|---|---|
| Volunteer 2 |  |

**Cheek**

| Volunteer 1 |  |
|---|---|
| Volunteer 2 |  |

**Eye**

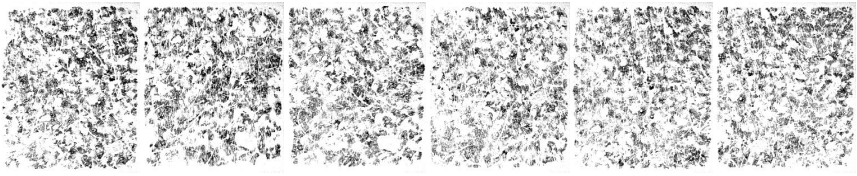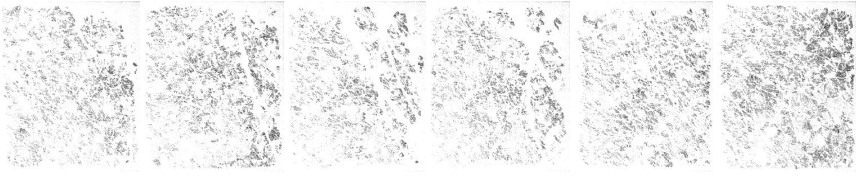| Volunteer 1 |  |
|---|---|
| Volunteer 2 |  |

***Figure 4.2*** *The capacitive images on the forehead, cheek and eye from two male volunteers with different ages, volunteer 1 (age from 20-30) and volunteer 2 (age from 40-50).*
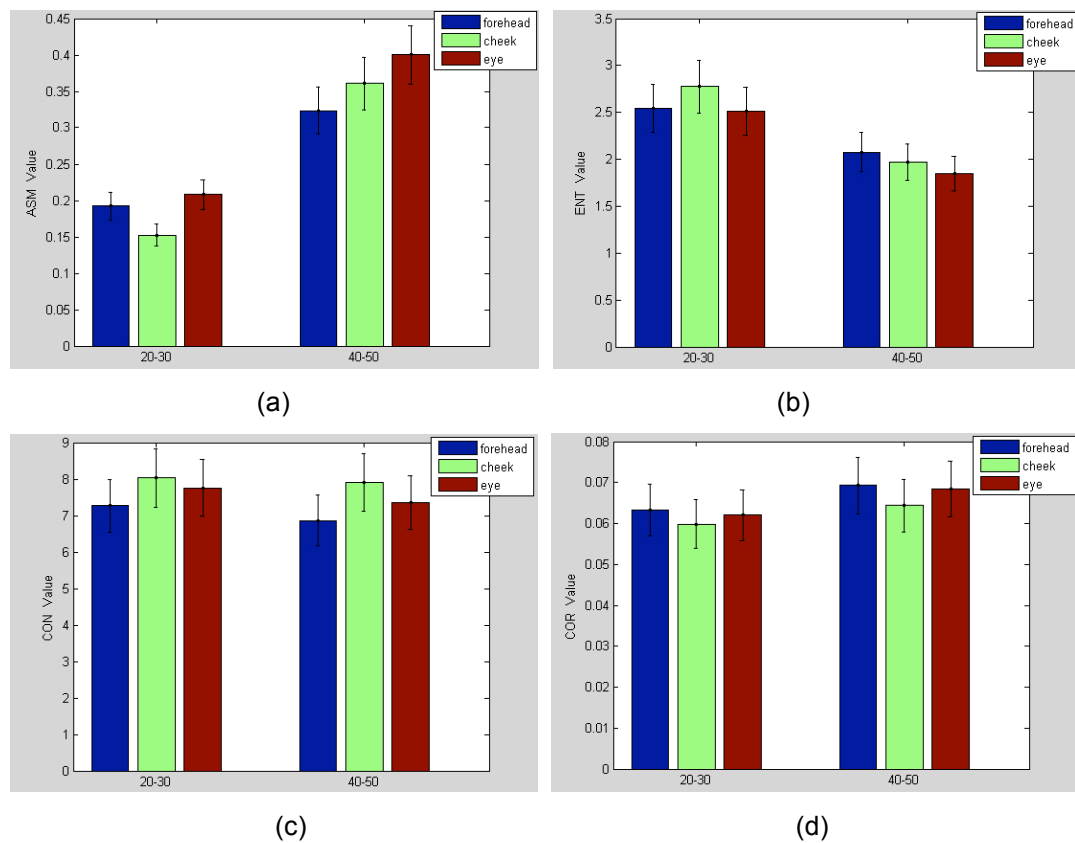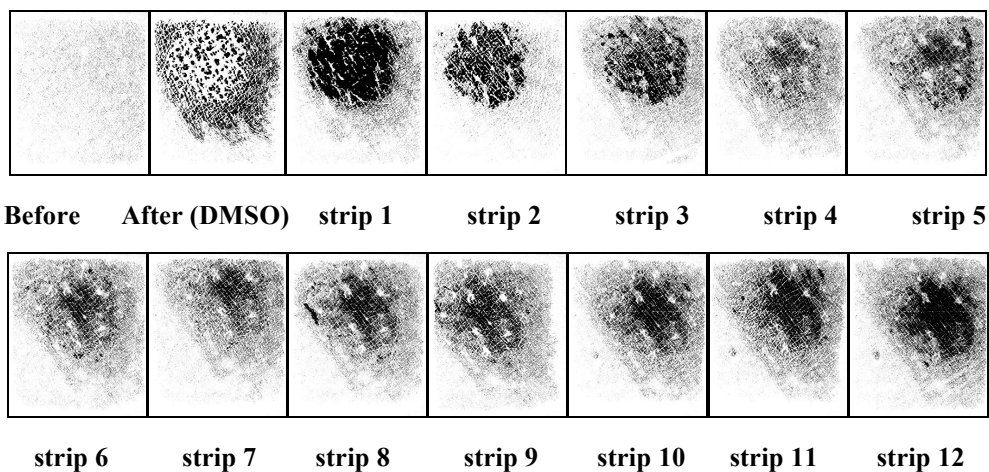
(a)

(b)

(c)

(d)

**Figure 4.3** *The corresponding graph of the feature vectors of images of Figure2, (a) The graph of ASM; (b) The graph of ENT; (c) The graph of CON; (d) The graph of COR. The error bars show the standard deviation of each site, which was repeated six times.*
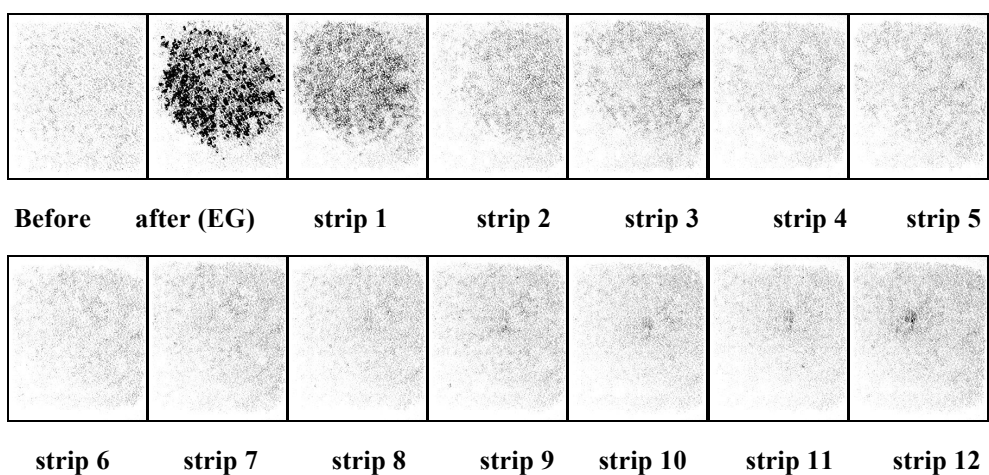
*4.2.2 Experiment 2 – Skin Solvent Penetration with Tape Stripping*

Figure 4.5 shows the corresponding GLCM feature vector results of the Figure 4.4 images. The fluctuation of the data largely reflects the noise, measurement error and bio-variability; however, if we use the control skin site as a reference, we can compare the trend of two test skin sites.

A



| Before | After (DMSO) | strip 1 | strip 2 | strip 3 | strip 4 | strip 5 |

| strip 6 | strip 7 | strip 8 | strip 9 | strip 10 | strip 11 | strip 12 |

B



| Before | after (EG) | strip 1 | strip 2 | strip 3 | strip 4 | strip 5 |

| strip 6 | strip 7 | strip 8 | strip 9 | strip 10 | strip 11 | strip 12 |

C



| Before | After | strip 1 | strip 2 | strip 3 | strip 4 | strip 5 |

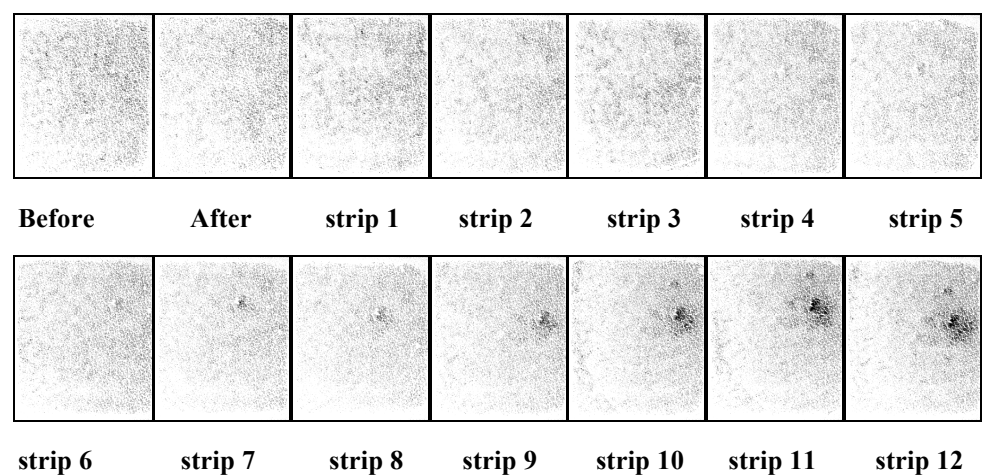| strip 6 | strip 7 | strip 8 | strip 9 | strip 10 | strip 11 | strip 12 |

**Figure4.4** *The capacitive images of (A) the DMSO skin site, (B) the ethylene glycol site, and (C) the control site, before and after solvent application and subsequently during tape stripping*

In the angular second moment results, the two test skin sites fluctuated along the control site, indicating there is no difference. The overall downward trend on three different skin sites is likely due to the texture on three different skin sites, shown in Figure 4.4, becoming thinner and thinner with the increasing number of tape stripping.

Figure 4.4 shows the capacitive images of three skin sites of on the volar forearm of a healthy female volunteer during the solvent penetration measurements. The results show that the capacitive images can clearly differentiate the solvents, e.g. DMSO and EG, from the skin. The results also show that DMSO penetrates more and deeper than EG.

In the entropy results, the two test skin sites fluctuated along the control site, a slightly more than the angular second moment results, but again, no significant difference. The overall upward trend on three different skin sites is likely because of the texture on three different skin sites, shown in Figure 4.4, becoming denser with the increasing number of tape stripping.

It is quite different for the contrast results. The control site increased first then gradually decreased. The changes of the contrast values of the skin sites applied DMSO and EG are far greater than the variation range of the control site, especially in the beginning. The EG site dropped significantly immediate after the EG application, then gradually increased to the similar level as the control site. This suggests that with the increasing number of the tape stripping, the amount of EG in skin is decreasing, until it is almost exactly the same as the control site. For DMSO site, it also decreased sharply after the DMSO application, indicates the presence of DMSO in skin, but it did not recover back to the control site level, this indicates that DMSO has penetrated much deeper and probably caused more damage than EG. A similar reverse trend can also be observed in the correlation results.
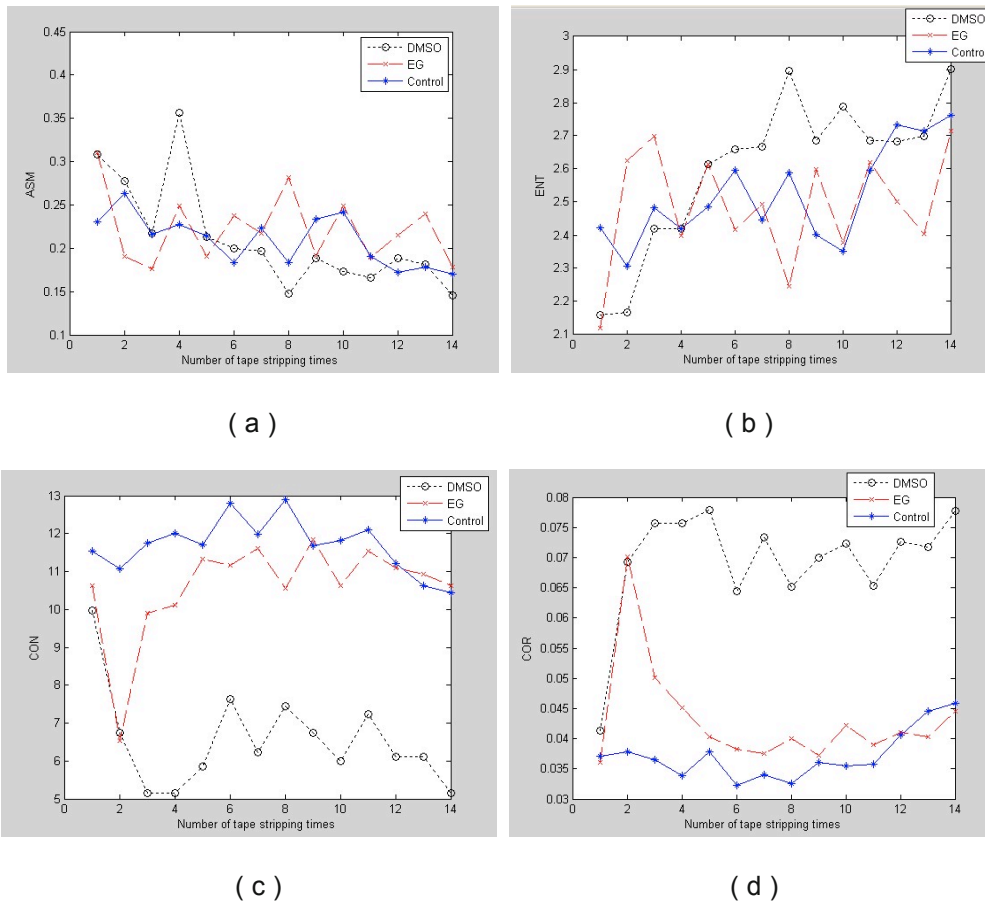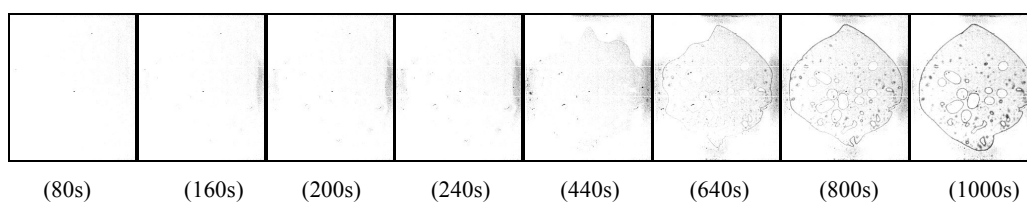
( a )　　　　　　　　　　　　　　　( b )

( c )　　　　　　　　　　　　　　　( d )

***Figure 4.5*** *The trend graph of feature vectors on three different skin sites　(a) The trend graph of ASM on three different skin sites　(b) The trend graph of ENT on three different skin sites　(c) The trend graph of CON on three different skin sites　(d) The trend graph of COR on three different skin sites*
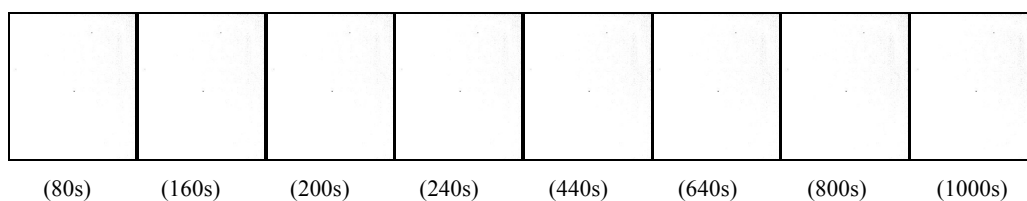
Combined with the first experiment, it is concluded that the angular second moment values and the entropy values reflect more about the skin texture, rather than topically applied solvents, whilst the contrast values and the correlation values reflect more about the topically applied solvents. These results also show that GLCM could be potentially a powerful tool for skin aging studies and skin solvent penetration studies; we could use GLCM to quantify the skin texture and skin aging. Through proper calibrations, it is also possible to use GLCM to quantify the solvent absorption within skin, and the solvent penetration through skin.
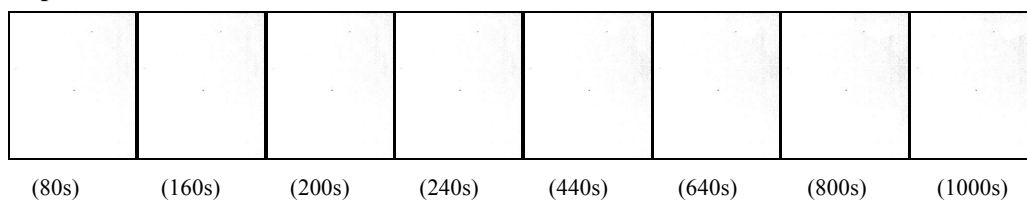
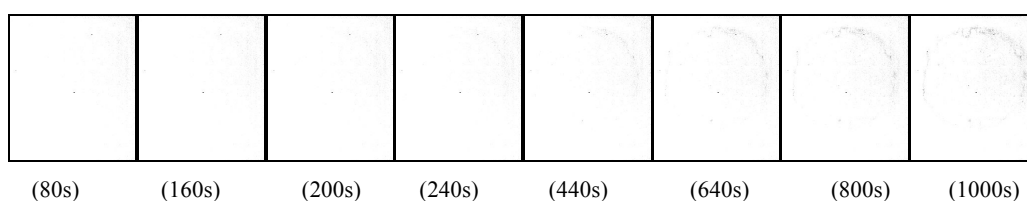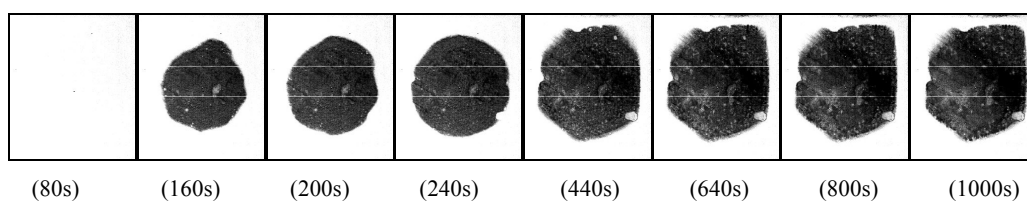## 4.2.3 Experiment 3 – Membrane Solvent Penetrations

**A. Butanol**



(80s)    (160s)    (200s)    (240s)    (440s)    (640s)    (800s)    (1000s)

**B. Decanol**



(80s)    (160s)    (200s)    (240s)    (440s)    (640s)    (800s)    (1000s)

**C. Heptanol**



(80s)    (160s)    (200s)    (240s)    (440s)    (640s)    (800s)    (1000s)

**D. PG**



(80s)    (160s)    (200s)    (240s)    (440s)    (640s)    (800s)    (1000s)

**E. Water**



(80s)    (160s)    (200s)    (240s)    (440s)    (640s)    (800s)    (1000s)

**F. Ethanol**



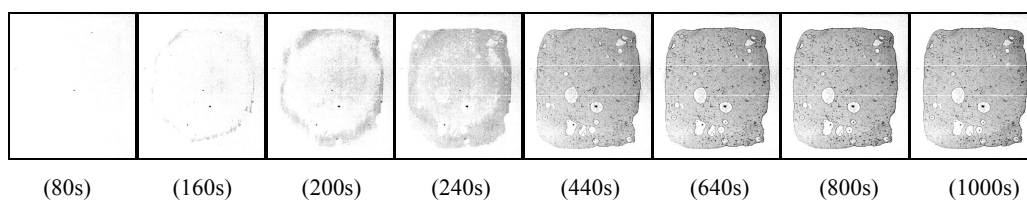(80s)    (160s)    (200s)    (240s)    (440s)    (640s)    (800s)    (1000s)

**Figure 4.6** *The capacitive images of membrane solvent penetrations at different times after application. (A) butanol, (B )decanol, (C) heptanol, (D) PG, (E) water and (F) ethanol.*

Figure 4.6 shows the capacitive images of butanol, decanol, heptanol, PG, water and ethanol membrane penetrations at different times. The results show that the capacitive

images can clearly reflect the rate and the equilibrium of penetration of different solvents.
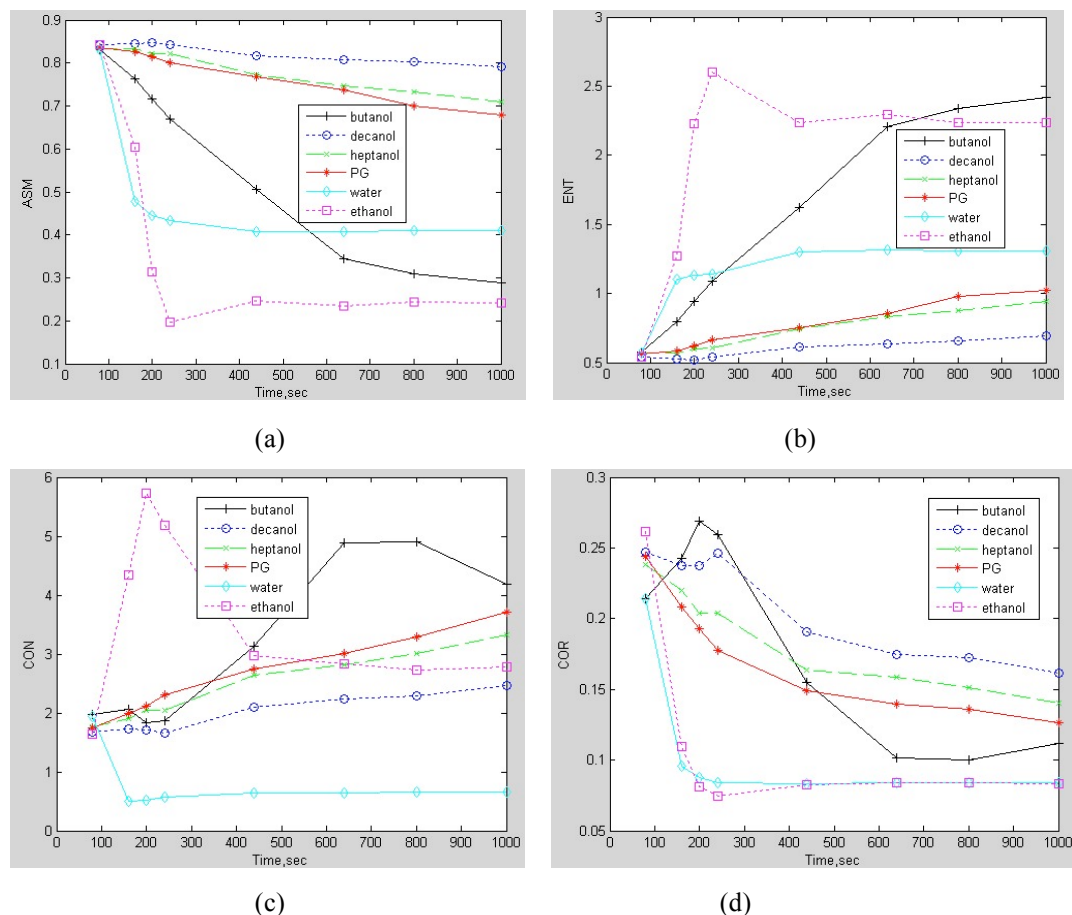


(a)                                          (b)

(c)                                          (d)

**Figure 4.7** *The corresponding graph of the feature vectors of images of Figure4.6. (a) The ASM of 6 different solvents   (b) The ENT of 6 different solvents   (c) The CON of 6 different solvents   (d) The COR of 6 different solvents*

Figure 4.7 shows the corresponding GLCM feature vector results of the Figure 4.6 images. The angular second moment (ASM) values of decanol, heptanol and PG show a slow downward trend; this is likely because the 3 different solvents shown in Figure 4.6 penetrated very slowly. The ASM values of ethanol and water dropped significantly immediately after the solvents application, then stabilized. This is likely because the two different solvents shown in Figure 4.6 penetrated very fast initially, and quickly they reached steady state. Whilst the penetration of butanol is somewhere

between the two groups. The entropy values of the solvents, as well as the correlation values, also tell a similar story.

The contrast values of ethanol shows a quick different profile than other solvent; this is likely due to the non-uniform penetration of ethanol, which is clearly visible in Figure 4.6.

*4.2.4 Experiment 4 –Skin Immersive Hydration*

A



Before      After      5min      10min      15min      20min      30min

B



Before      After      5min      10min      15min      20min      30min
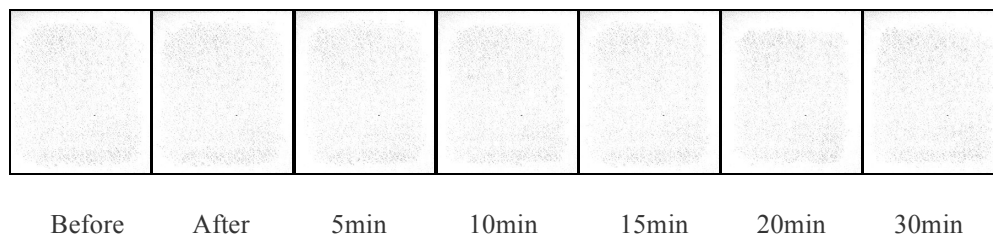
***Figure 4.8** The capacitive images of (A) the control skin site and (B) soaked skin site*

Figure 4.8 shows the capacitive images of the control skin site and test skin site. The results show that the capacitive images can clearly reflect the water content of skin and the evaporation rate of water content in the skin.

(a)                                                    (b)

(c)                                                    (d)

**Figure 4.9** *The trend graph of feature vectors on two different skin sites: (a) the ASM on two different skin sites, (b) the ENT on two different skin sites, (c) the CON on two different skin sites and (d) the COR on two different skin sites.*
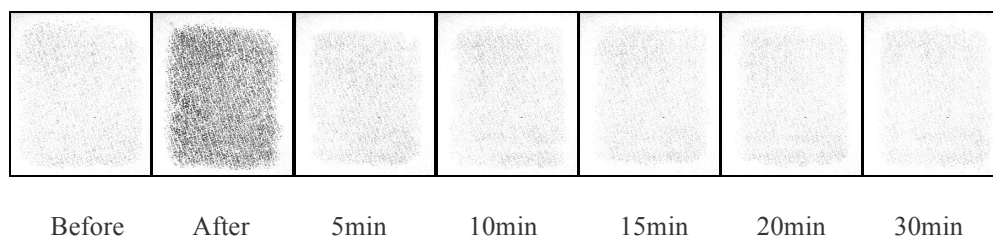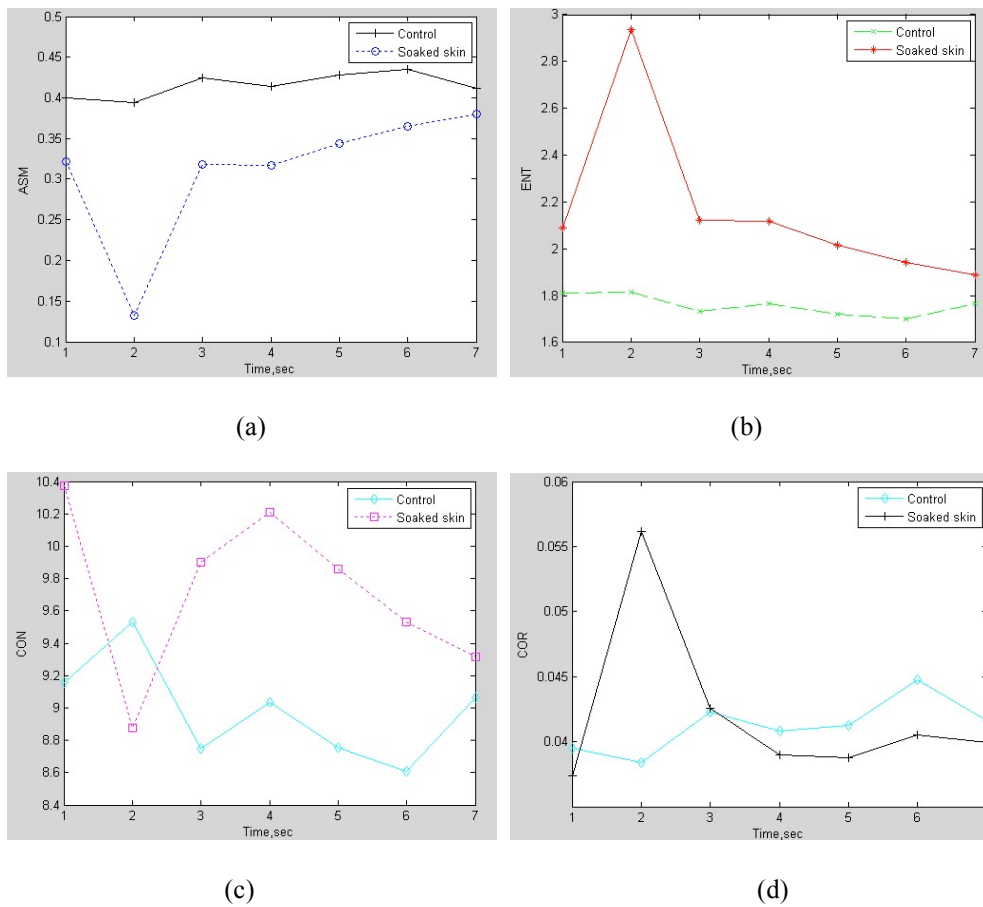
Figure 4.9 shows the corresponding GLCM feature vector results of the Figure 4.8 images. The angular second moment values on control site did not change very much as expected. The skin test site value dropped significantly immediately after soaking, then increased significantly immediately to the similar level as before, this is likely because of the texture of hydration skin became finer with the increased skin water content, and then as the water content of the skin recovered and the textures are also recovered. It is interesting to point out that although this particular volunteer's skin can pick a lot of extra water through soaking, it lost the water very quickly, only 5min, which might indicate a poor water holding capability. The other feature values also tell a similar story.

*4.2.5 The effects of GLCM displacement distance*

In this study, for the reason of simplicity, the GLCM displacement distance parameter *d* value is set to 1. However, when the distance values change, the feature vectors will also change. This section will discuss how to select the optimum distance through analyzing the influence of distance change to the feature vectors. This study is applied on six different grey capacitive images captured form forehead, cheek, eye and arm shown in Figure 4.10. Because the increase of the distance value between two pixels will cause the loss of information, so the value of distance should not be too big. In this study, the range of distance is chosen from 1 to 16.
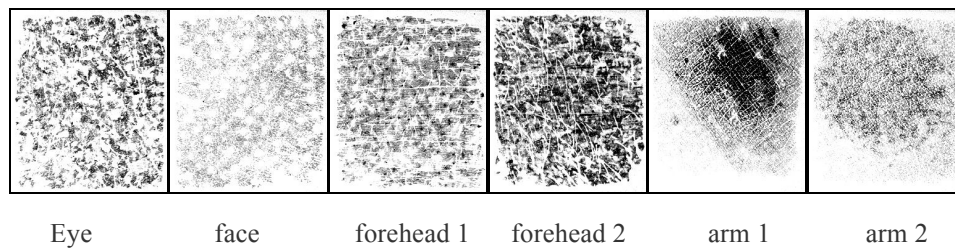


| Eye | face | forehead 1 | forehead 2 | arm 1 | arm 2 |

**Figure 4.10** *Sample images from different skin sites*

Figure 4.11 shows the changes of the four different feature vectors with different distance values. As it can be seen, the values of the four different feature vectors appear a clearly upward or downward trend when the distance value changed from 1 to 10, and became stable when the distance values changed from 10 to 14. According to the above analysis, it can be concluded that the optimum range of the distance value is from 10 to 14 because the values of four different feature vectors are stable and reflect a very clear difference for six different tested images within this interval. Therefore in the future we can use GLCM with optimized displacement distances.
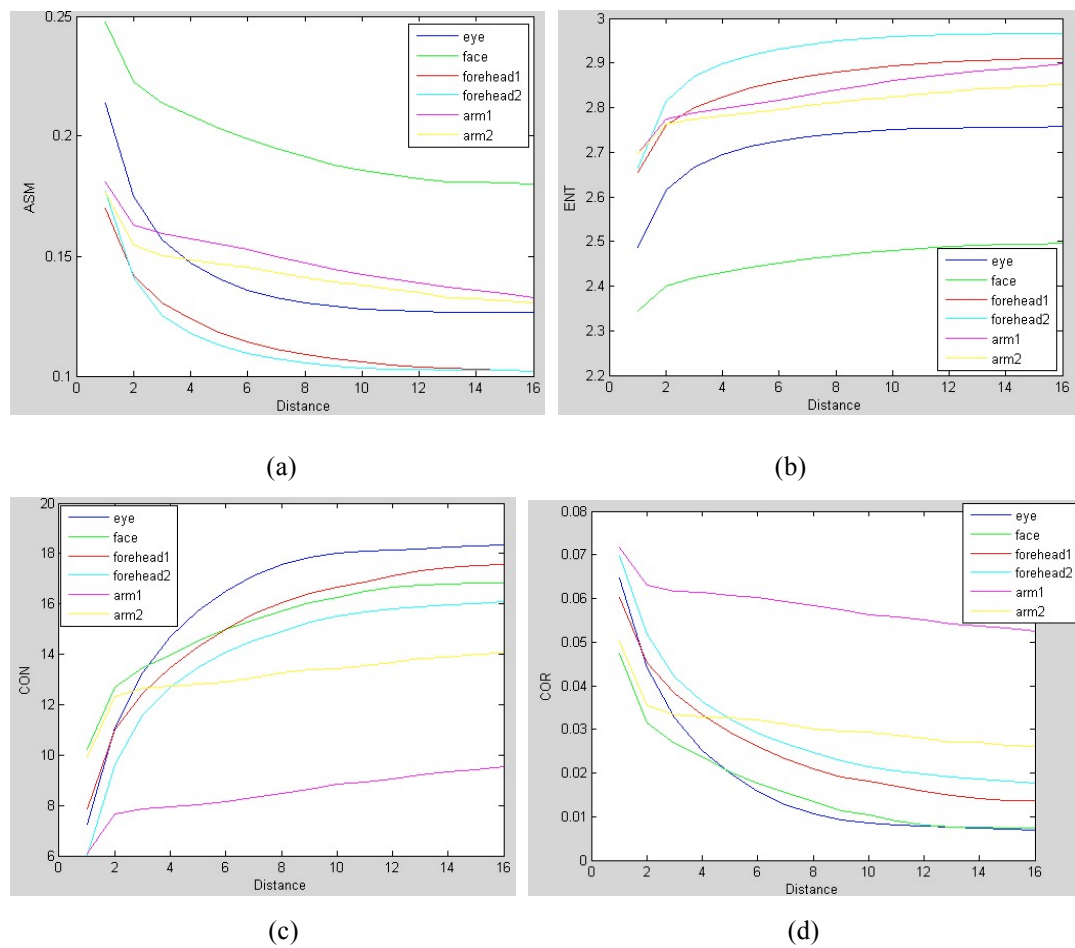
(a)                                               (b)

(c)                                               (d)

***Figure 4.11*** *The trend graph of feature vectors with different distance values (a) The ASM with different distance values (b) The ENT with different distance values (c) The CON with different distance values (d) The COR with different distance values*

## 4.3 Conclusions

In summary, a new mathematical algorithm based on Grey Level Co-occurrence Matrix (GLCM) has been developed for analyzing grayscale capacitive skin images. Four different GLCM feature vectors, which are angular second moment, entropy, contrast and correlation, are used in the study. The effects of GLCM displacement distance parameter on feature vectors are discussed. The results show that GLCM can

separate the skin texture information from solvent penetration information in the same skin image, which make it a potentially useful tool for studying skin texture as well as skin solvent penetrations. Comparing with other skin texture analysis techniques, such as physical measurements, photographs, and silicone molds [73], GLCM can extract more texture information based on different feature vectors [74]. Combining with tape stripping, GLCM can also generate solvent concentration profiles at different depths within stratum corneum, which is very important in trans-dermal drug delivery studies.

# Chapter 5 Portable Opto-Thermal Radiometry with Infrared Emitter and PbS Detector

The OTTER technology described in chapter 2 has been a powerful tool for skin measurements. But it is still a bench-top technology, due to the size of the laser, power supply, liquid nitrogen cooled MCT detector, and external cooling water system etc., which limit its usages only within the laboratory. The aim of this chapter is to further improve the OTTER technology, by design and develop a portable opto-thermal radiometry instrument which can work outside the laboratory and at room temperature. Figure 5.1 shows the initial design schematic diagram.
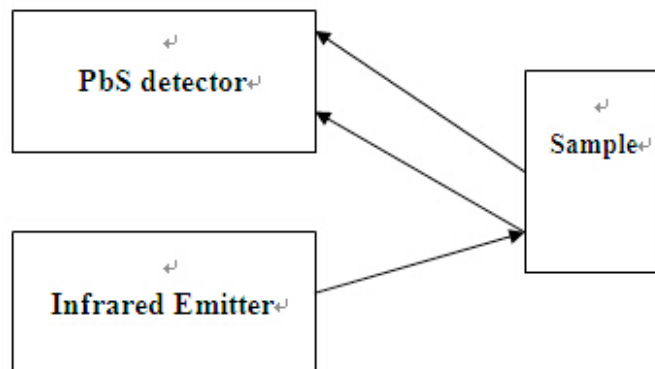


**Figure 5.1** *The initial design schematic diagram of the portable opto-thermal radiometry instrument.*

It uses a modulated broadband Infrared Emitter to heat up the sample surface, and a PbS (lead sulphide) detector to detect the corresponding blackbody radiation from the sample. PbS detector can detect a range of different wavelengths signals, and hence can generate the spectra of materials.

This chapter will first introduce its design principle and then present the experimental results.

## 5.1 Infrared Emitter and PbS detector

### 5.1.1Infrared radiation

An important characteristic of electromagnetic radiation is wavelength. The Electromagnetic radiation can be classified according to wavelength. There are several categories of the radiation, for example, infrared, visible, or microwave.
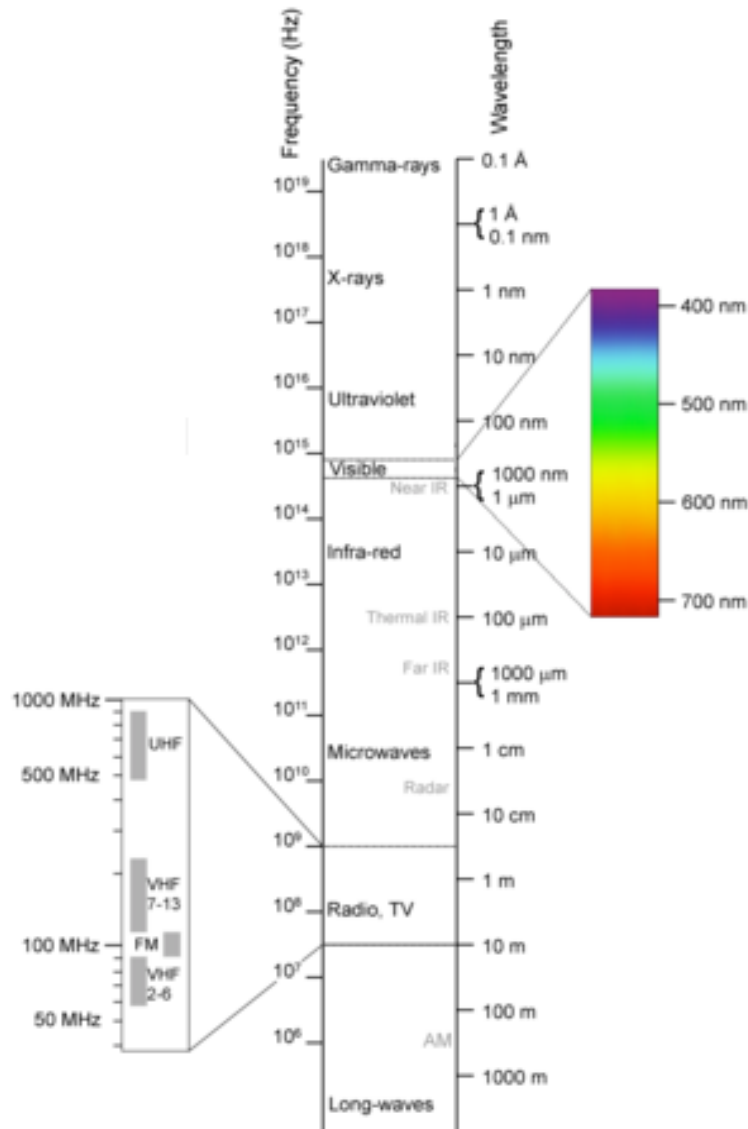


***Figure 5.2*** *Electromagnetic spectrum [78]*

Figure 5.2 shows that Infrared radiation is the electromagnetic waves in the wavelength region longer than the visible light wavelengths, lying from 0.75 *um* to 1000 *um*. The Infrared radiation [75-77] can be classified into one of several categories according to the different wavelength region, for example, the near infrared (from 0.75 *um* to 3 *um*), the middle infrared (from 3 *um* to 6 *um*), and the far infrared (from 6 *um* to 15 *um*). Also, even longer wavelength regions are sometimes referred to as ultra far infrared, but this is not a universally accepted term.

Infrared radiation has the following characteristics: (1) invisible to human eyes (2) small energy (3) long wavelength (4) emitted from all kinds of objects.

## 5.1.2 Infrared Emitter

Semiconductor-based infrared emitters [79] are classified as incoherent and coherent sources. Incoherent sources which have the ability to modulate the infrared radiation quickly and to look cold as well as hot relative to the background (negative luminescence) are mainly based on diode structures. They also have greater power efficiency. Coherent sources or lasers produce a very high spectral intensity of infrared over a small spectral bandwidth. Electrically pumped lasers, optically pumped lasers and quantum cascade lasers are three main lasers for the coherent sources. Infrared Emitter which is used in this chapter belongs to incoherent sources.

The structure of an infrared emitter is similar to the diode. Figure 5.3 indicates that electrons are injected into the p-type side and holes are injected into the n-type side. Some of these carriers recombine radioactively leading to infrared emission.
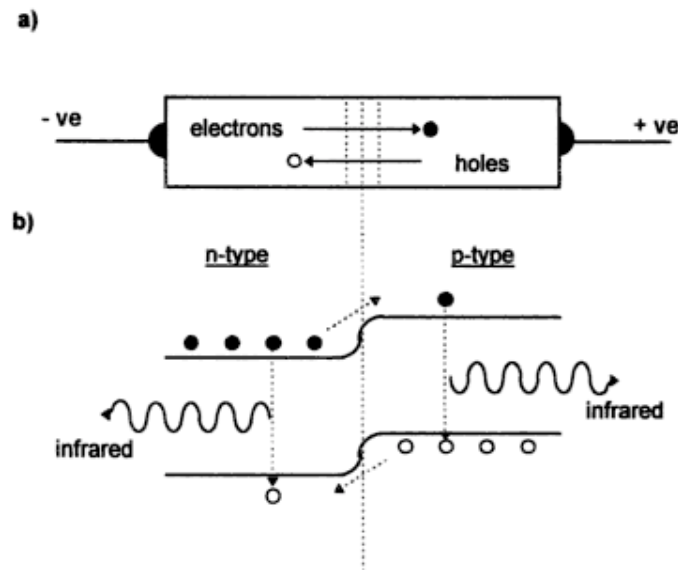
**Figure 5.3** *Operation of an infrared Emitter a) schematic diagram b) band diagram [80]*

## 5.1.3 PbS detector

Infrared detectors are classified into thermal types and quantum types. Thermal detectors perform by the temperature rise induced in an active element by the absorption of incident radiation. Thermal detectors do not require cooling, but have disadvantages that response time is slow and detection capability is low. In contrast, even though quantum detectors' photo sensitivity is dependent on wavelength, they offer better detection performance and a faster response speed. In general, quantum detectors must be cooled for accurate measurement, except for detectors used in the near infrared region. Types of infrared detectors [81-84] are shown in Table 5.1.

| Type | | | Detector | Spectral response (μm) | Operating temperature (K) | $D^*(cm \cdot Hz^{1/2}/W)$ |
|---|---|---|---|---|---|---|
| Thermal type | Thermocouple · Thermopile Bolometer Pneumatic cell Pyroelectric detector | | Golay cell, condenser-microphone PZT, TGS, LiTaO³ | Depends on window material | 300 300 300 300 | $D^* (\lambda,10,1) = 6 \times 10^8$ $D^* (\lambda,10,1) = 1 \times 10^8$ $D^* (\lambda,10,1) = 1 \times 10^9$ $D^* (\lambda,10,1) = 2 \times 10^8$ |
| Quantum type | Intrinsic type | Photoconductive type | PbS PbSe InSb HgCdTe | 1 to 3.6 1.5 to 5.8 2 to 6 2 to 16 | 300 300 213 77 | $D^* (500,600,1) = 1 \times 10^9$ $D^* (500,600,1) = 1 \times 10^8$ $D^* (500,1200,1) = 2 \times 10^9$ $D^* (500,1000,1) = 2 \times 10^{10}$ |
| | | Photovoltaic type | Ge InGaAs Ex. InGaAs InAs InSb HgCdTe | 0.8 to 1.8 0.7 to 1.7 1.2 to 2.55 1 to 3.1 1 to 5.5 2 to 16 | 300 300 253 77 77 77 | $D^* (\lambda p) = 1 \times 10^{11}$ $D^* (\lambda p) = 5 \times 10^{12}$ $D^* (\lambda p) = 2 \times 10^{11}$ $D^* (500,1200,1) = 1 \times 10^{10}$ $D^* (500,1200,1) = 2 \times 10^{10}$ $D^* (500,1000,1) = 1 \times 10^{10}$ |
| | Extrinsic type | | Ge : Au Ge : Hg Ge : Cu Ge : Zn Si : Ga Si : As | 1 to 10 2 to 14 2 to 30 2 to 40 1 to 17 1 to 23 | 77 4.2 4.2 4.2 4.2 4.2 | $D^* (500,900,1) = 1 \times 10^{11}$ $D^* (500,900,1) = 8 \times 10^9$ $D^* (500,900,1) = 5 \times 10^9$ $D^* (500,900,1) = 5 \times 10^9$ $D^* (500,900,1) = 5 \times 10^9$ $D^* (500,900,1) = 5 \times 10^9$ |

**Table 5.1** *Types of infrared detectors and their characteristics [85]*

There are three main characteristics of infrared detector, namely, photo sensitivity, noise equivalent power (NEP) and D*:

(1) Photo sensitivity (Responsivity)

Photo sensitivity (Responsivity) is the output voltage (or output current) per watt of incident energy when noise is not a consideration.

$$R = \frac{S}{PA} \tag{5.1}$$

Where S is the signal output, P is the incident energy and A is detector active area.

(2) Noise equivalent power: NEP

This is the quantity of incident light equal to the intrinsic noise level of a detector. In other words, this is the quantity of incident light when the signal-to-noise ratio (S/N) is 1.

$$NEP = \frac{PA}{S/N \cdot \sqrt{\Delta f}} \tag{5.2}$$

where $N$ is the noise output and $\Delta f$ is the noise bandwidth.

(3) Detectivity: D* (D-star)

$D^*$ is the photo sensitivity per unit active area of a detector, which makes it easier to compare the characteristics of different detectors. In many detectors, NEP is proportional to the square root of the detector active area, so D* is defined by the following equation.

$$D^* = \frac{S/N \cdot \sqrt{\Delta f}}{P \cdot \sqrt{A}} = \frac{\sqrt{A}}{NEP} \qquad (5.3)$$

Under normal circumstances, the D* of a detector irradiated by a blackbody source is expressed in the format of D* (A, B, C), for example, as D* (500 °K, 1000 Hz, 1 Hz), where 500 °K is the blackbody source temperature, 1000 Hz is the chopping frequency and 1 Hz is the noise equivalent bandwidth. It can be said that a larger value of D* indicates a better detector element.

When selecting infrared detectors for testing, it is also important to consider other characteristics, for example, spectral response which defines the sensitivity of a detector to radiation at a various wavelengths wavelength, response time, cooling method, number of elements (single element, one-dimensional array, two-dimensional array, etc.)

A PbS detector from CalSensors (Camarillo, CA, USA) is used in this study. The PbS detector is a photoconductive detector which is a semiconductor with holmic contacts to form a two-port electrical device. The resistance is reduced when infrared radiation enters the detecting elements. Compared with other detectors in the same wavelength region, the PbS detector has superior features, such as higher detection capability and faster response speed. Although PbS detector performs at room temperature, the dark resistance, photo sensitivity and response characteristics will change depending on the temperature. Therefore, care is required to ensure the best results.

## 5.2 The Drive Circuits for Infrared Emitters and PbS detector

*5.2.1 The Drive Circuit for Infrared Emitters*

The emission source is composed of a PIRE plus high-speed infrared emitter with integrated drive electronics. The components have been designed as a system to provide maximum output over a range of pulsing speeds. The Infrared Emitter has been designed to optimize both heat-up and cool-down performance of the filament, producing typical pulsing speeds of 180Hz at 50% modulation depth. The associated drive electronics are matched to the emitter to provide the optimal drive waveform over a range of frequencies and ensure peak output temperatures at all frequencies. Together these components provide a convenient source of pulsed infrared energy which can be used to improve the performance of infrared detection systems. The key features of this Infrared Emitter are:

1) Fast pulse rates, up to 180Hz with 50% modulation depth;

2) Adjustable pulse rates with 0 to 5V control circuitry;

3) Compact, reduced footprint solution;

4) Broadband output with 88% emissivity;

5) Low overall system cost;

6) Typ. MTTF of >26,000 hrs at max rated power.

and another parameters of it are shown in table 5.2:

| Specification | Minimum | Typical | Maximum |
|---|---|---|---|
| Emitter Voltage | 3V | | 12V |
| Pulse Frequency Range | 2Hz | 100Hz | 200Hz |
| Frequency Control Voltage | 0V | 2.5V | 5V |
| Emitter Resistance | | 2.5Ω | |
| Peak Emitter Current (12V) | | | 5A |
| Average Emitter Current (12V) | 10mA | | 220mA |
| Output Enable Voltage | 0V (disable) | | 5V (enable) |
| Filament Temperature (12V) | | | 1000°K |
| Filament Emissivity | | 88% | |
| Operating Temperature | -30°C | | +100°C |
| Lifetime (MTTF) | 26,000 Hrs | | |
| Spectral Output (with Sapphire Window) | 0.35µm | | 6µm |

***Table 5.2** the data sheet of the Infrared Emitter [86]*

The Figure 5.4 shows the drive circuit for this Infrared Emitter. The LM7805 is a voltage regulator chip, which can change 12 volt voltage into 5 volt. The C1, C2, C3 and C4 are power supply decoupling capacitors. This drive circuit can generate the pulse signal of 100Hz.
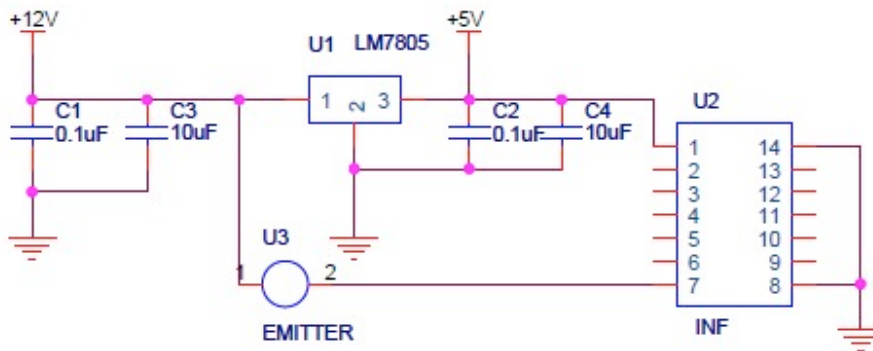


***Figure 5.4*** *the drive circuit for Infrared Emitter*

## 5.2.2 The Drive Circuit for PbS detector

A high sensitivity PbS single channel detector AP-15 [87] is used in this chapter. The key features of this detector are:

1) Highest sensitivity detector operating across 1-5 micron region;

2) Provides high signal to noise performance for wide measurement dynamic range;

3) Fastest response speed for mid-IR applications;

4) High reliability for long life;

5) Consistent repeatable results minimize testing.

The main parameters of the detector are shown in Table 5.3:

| Model # | Part # | Element Size (mm) | Op. Temp. (°C)[3] | Wave-length (pk signal, μm) | D* (cm Hz$^{1/2}$/W) | | Responsivity (λpk, 650Hz, V/W) | | Dark Resistance (@23°C, MΩ/sq) | Time Constant (μs) | ΔT at max cool (°C) | Std Pkg (TO) |
|---|---|---|---|---|---|---|---|---|---|---|---|---|
| | | | | | (λpk, 650Hz, 1Hz) | (500K, 650Hz, 1Hz) | Min | Typ | | | | |
| AP Series - Ambient PbS detectors[1,3] | | | | | | | | | | | | |
| AP-15 | 40361 | 1x1 | | | | | 5.3 x10⁵ | 8.0 x10⁵ | | | | 5 |
| AP-18 | 40364 | | | | | | | | | | | 8 |
| AP-25 | 40128 | 2x2 | | | 8x10¹⁰ min 1x10¹¹ typ | | 2.7x10⁵ | 4.0 x10⁵ | | | | 5 |
| AP-28 | 40365 | | +23 | 2.4 typ | | 7.5x10⁹ min 9.4x10⁸ typ | | | 0.5 - 2.0 1.0 typ | 200 typ 400 max | N/A | 8 |
| AP-35 | 40363 | 3x3 | | | | | 1.7x10⁵ | 2.6 x10⁵ | | | | 5 |
| AP-38 | 40366 | | | | | | | | | | | 8 |
| AP-68 | 40368 | 6x6 | | | 7x10¹⁰ min | | 9 x10⁴ | 1.4 x10⁴ | | | | 8 |
| AP-103 | 40338 | 10x10 | | | 6x10¹⁰ min | | 5 x10⁴ | 7.5 x10⁴ | | | | 3 |

1 Specifications apply at a bias voltage of 50V/mm across a detector and 1Mohm load resistor (in series) or 25v/mm directly across the detector

2 Specifications apply at max cooling with a heat sink at +25℃. Typical cooler at max cooling: AT1 -0.8V@2.0A, AT2S- 1.9V@ 1.4A

3 Max rated element temperature is 65 ℃.

***Table 5.3*** *the data sheet of the PbS detector [88]*

The thermal emission decay signal associated with the time dependent temperature field comes from the transient thermal radiation. According to Baltes [89], Kirchhoff's law can be used to non-equilibrium emissions, provided that the absorption also includes the stimulated emission as negative absorption. In this situation, Kirchhoff's law can be represented as:

$$\frac{\varepsilon^{'}}{\beta} = W_{BB} \tag{5.4}$$

where $\varepsilon^{'}$ is the emission coefficient defined as the radiant power per in the unit wavelength interval emitted into unit solid angle form a unit volume. $W_{BB}$ is described by Planck's formula and represents the spectral emissive power of a blackbody:

$$W_{BB}(\lambda, T) = \frac{2hc^2}{\lambda^5} \frac{1}{e^{\frac{hc}{KT\lambda}} - 1} \tag{5.5}$$

If the temperature deviations are much smaller than the initial temperature $T$ , $W_{BB}$ can be represented as a Taylor series and $\delta W_{BB}$ expressed as:

$$\delta W_{BB} \cong \frac{\partial W_{BB}}{\partial T} \theta(z,t) = B(\lambda,T)\theta(z,t) \tag{5.6}$$

where

$$B(\lambda,T) = \frac{W_{BB}}{T} \frac{hc}{KT\lambda} \frac{\exp(\frac{hc}{KT\lambda})}{\left[\exp(\frac{hc}{KT\lambda})-1\right]} \tag{5.7}$$

Eq. (5.6) and Eq. (5.7) can be used to calculate the total hemispherical power emitted by a unit surface element per unit wavelength interval. Using numerical integration, the total hemispherical power within the 1-3.3 $\mu m$ spectral intervals for 1K temperature variation at room temperature (293K) emitted by 1 $m^2$ blackbody is:

$$\delta W(\delta T) = \int_{0.000001}^{0.0000033} \frac{2h^2c^3}{KT^2\lambda^6}\delta T \frac{e^{\frac{hc}{KT\lambda}}}{(e^{\frac{hc}{\lambda KT}}-1)^2} d\lambda = 0.0115\,W/m^2 \tag{5.8}$$

Where h is Plank's constant, c is speed of light in vacuum.

The detector area which is chosen in this chapter is 1 $mm^2$ and if we ignore losses, the radiant power P which reaches the infrared detector is $1.15\times10^{-8}\,W$. Using the responsivity data form table 5.2 we can calculate the signal amplitude from the detector:

$$U = P \times \mathrm{Re}\,sponsivity = 0.0092V \tag{5.9}$$

The above equation shows that the value given by the detector is too small for direct digitization. In this case, a preamplifier is needed.

Figure 5.5 shows the schematic diagram of the preamplifier employed. The improved design is based on a proven design developed by Berg et al (2000) [90, 91]. It consists of two stages. The first stage uses an AD797 which is a very low noise, low distortion

operational amplifier. The amplification factor of this stage has to be as high as possible, so that the noise added by the following stage becomes negligible. An amplification factor of 101 had been set for this stage and the bandwidth is 1.5MHz. C22 in this stage is used to filter the high frequency noise. The second stage uses an OPA37 to provide a further amplification factor of 11 and a low impedance unity gain output buffer to prevent overloading of the AD797. Overall, the amplification factor of the preamplifier is 1100.
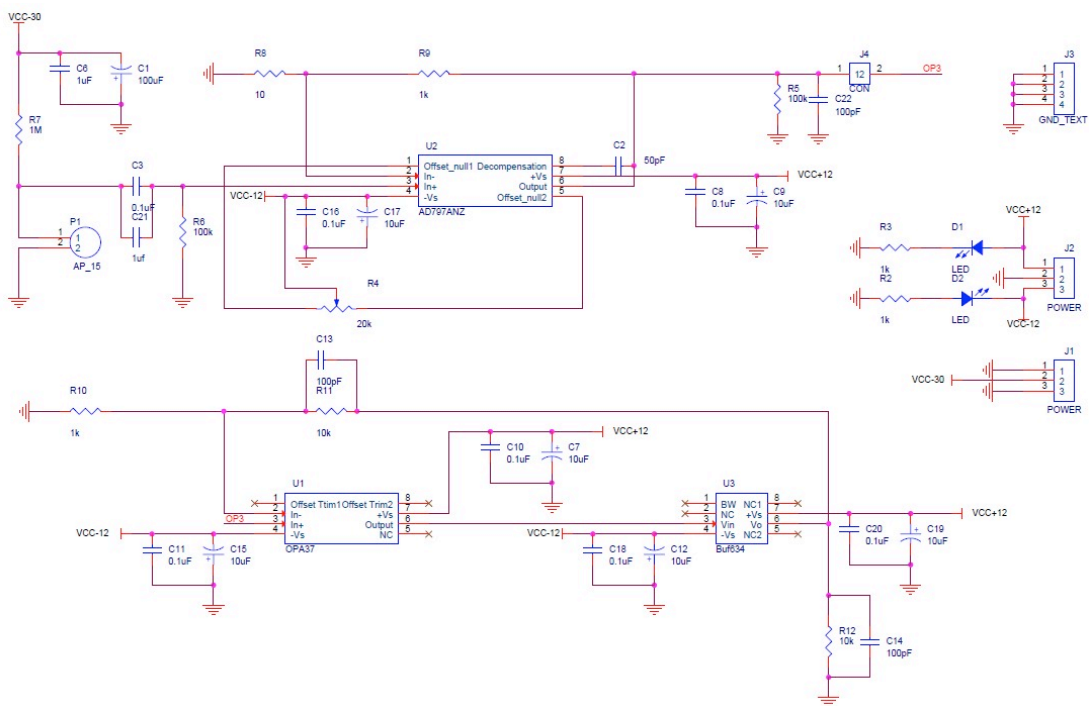


**Figure 5.5** *the drive circuit for PbS detector*

## 5.3 Results and Discussions

Figure 5.6 shows the PCB modules of the modulated Infrared Emitter and PbS detector, as well as the measurement setup. In this experiment, various of material have been tested, such as hand, forearm, thumb, white paper, aluminum, dry cardboard and wood etc. Figure 5.7 shows the measurement signal when no objects are placed in front of the Infrared Emitter and PbS detector. Figure 5.8 shows the signal when the PbS detector is facing directly to the Infrared Emitter. Figure 5.9

shows the signals of different materials when the amplification factor of the preamplifier is 100.
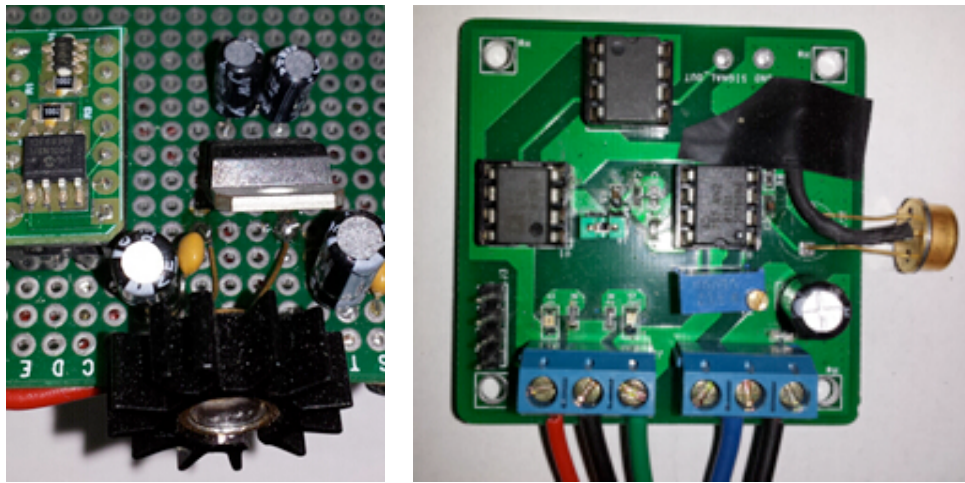


(a)

(b)
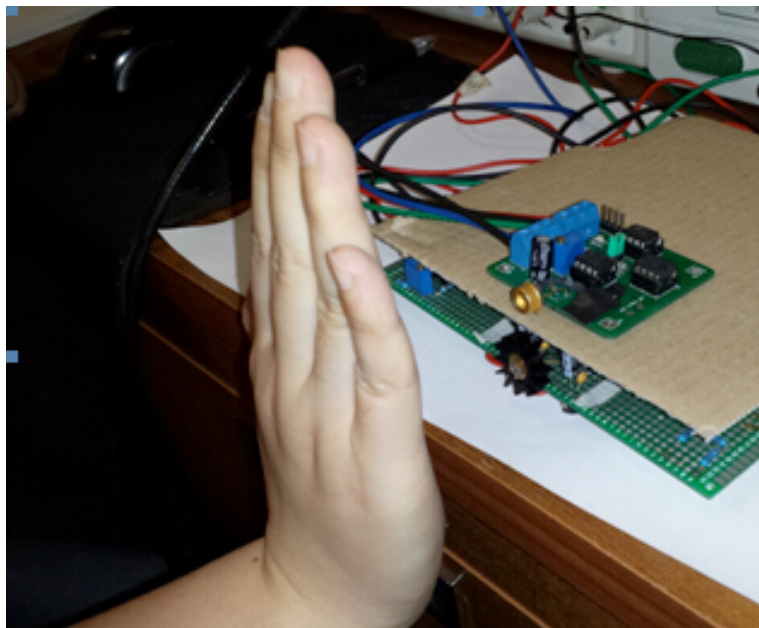


(c)

***Figure 5.6*** *The portable opto-thermal radiometry with a modulated Infrared Emitter and a room temperature PbS detector, (a) the PCB module of the modulated Infrared Emitter, (b) the PCB module of PbS detector, (c) the measurement setup using hand as a sample.*
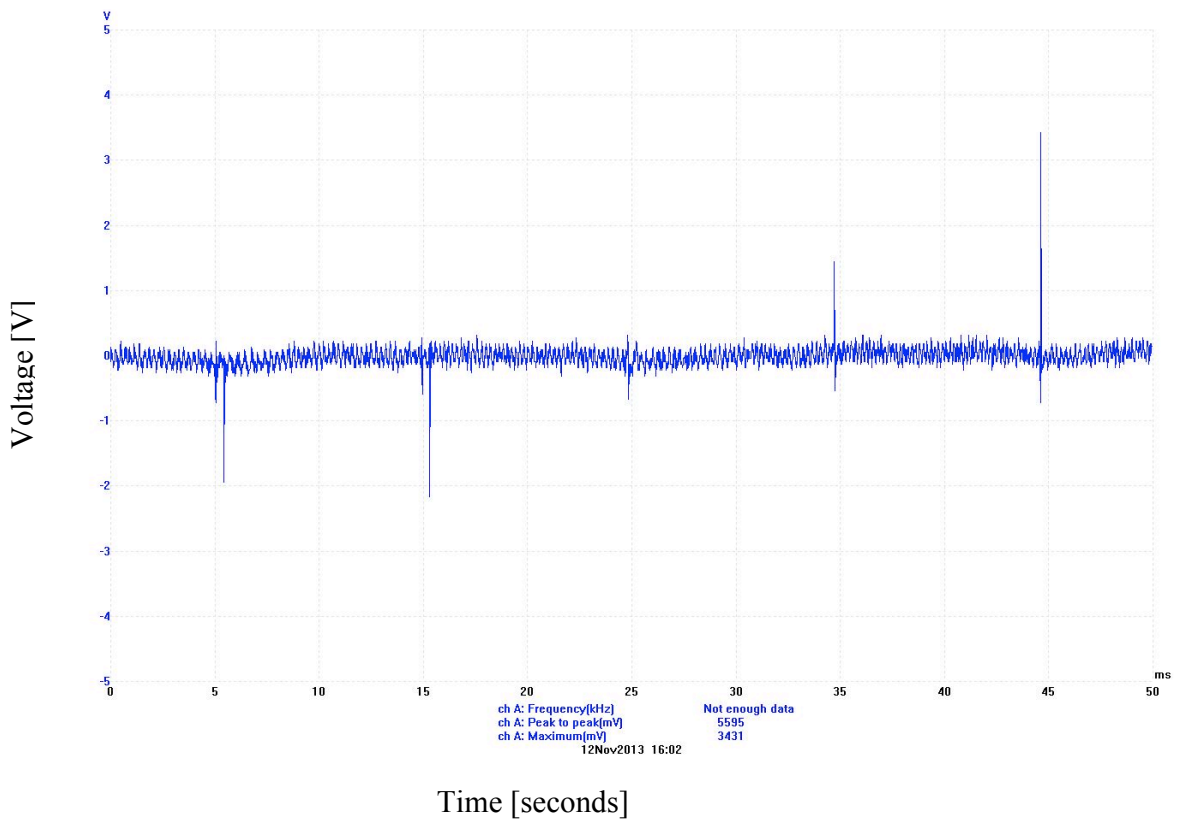
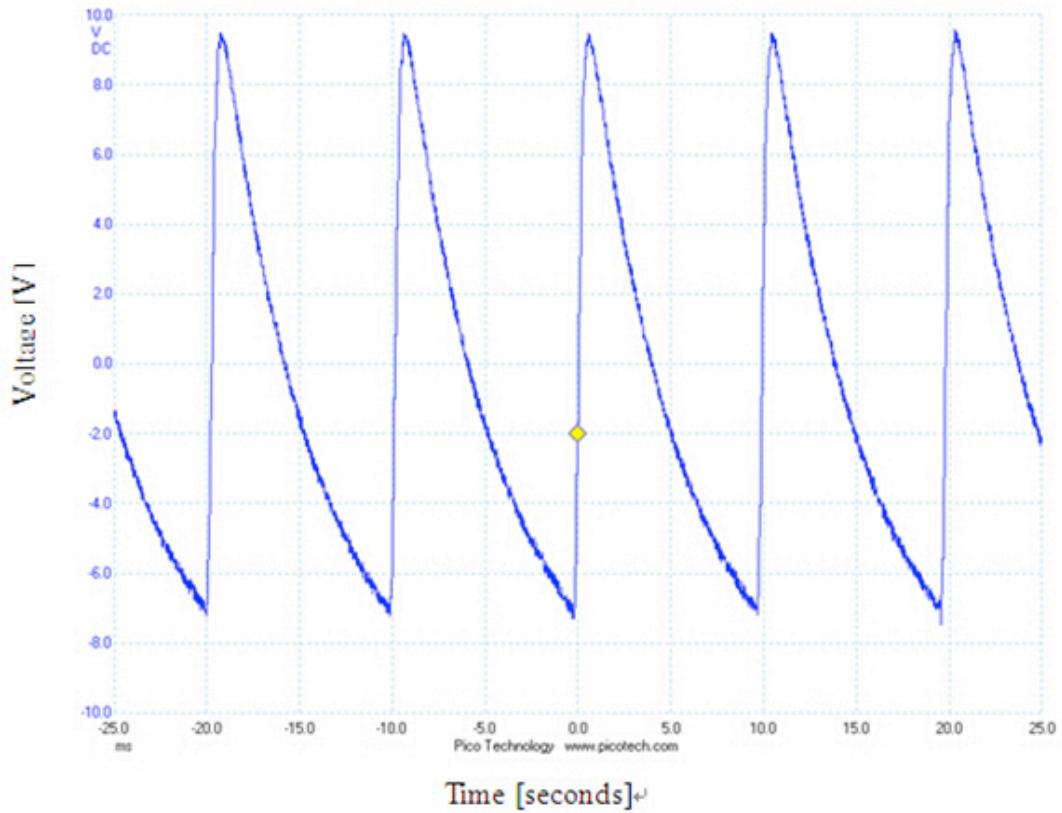**Figure 5.7** *The signal when no objects are placed in front of the Infrared Emitter and PbS detector*



**Figure 5.8** *The signal when the PbS detector is facing directly to the Infrared Emitter.*
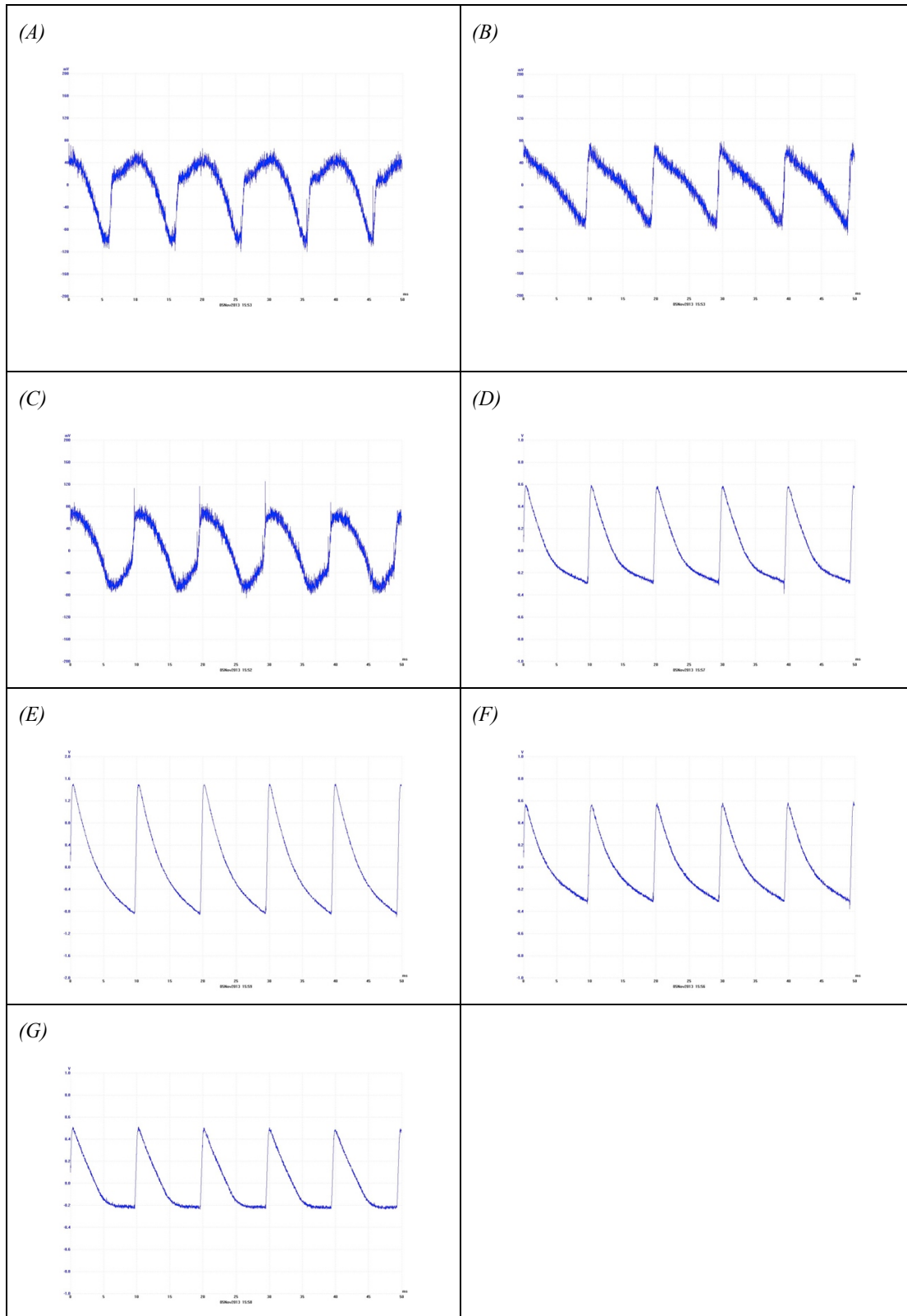
(A)

(B)

(C)

(D)

(E)

(F)

(G)

**Figure 5.9** *The measurement signals when the amplification factors are 100.    (A) back of hand; (B) forearm; (C) thumb; (D) white paper; (E) aluminum; (F) dry cardboard; (G) wood.*

81

Figure 5.10 shows the synchronized test results of different materials over one period of time when the amplification factor of the preamplifier is 1100. The results show that different materials have different peak amplitudes. Figure 5.11 shows the corresponding peak to peak values of the signals. The results show that aluminum has the biggest peak value within the seven different materials, whilst skin, particularly thumb skin, has the lowest peak values. The peak amplitude detected by the oscilloscope is proportional to reflection, refraction and the blackbody radiation. When the infrared radiation from Infrared Emitter reaches sample surface, some of the radiation will be reflected, some will be refracted and some will be absorbed, which in turn increase the sample surface temperature, and hence increase the blackbody radiation. Some of the refracted radiation in the sample will also be reflected at the internal sample and eventually go back into air. Through analyzing the shape of the infrared radiation from the sample, we can study the sample's optical and thermal properties, the thickness of the sample and its layer structure.

Comparing with OTTER, this new portable instrument is much smaller and cheaper. It can measure the differences of different samples, but it can't differentiate emitted infrared radiation from the reflected from sample surface and refracted radiation from inside sample. The peak amplitude value is dominantly determined by the optical reflection. In the future work, by using optical gratings or filters, it is possible to distinguish the infrared emission signal from reflected and refracted signals.
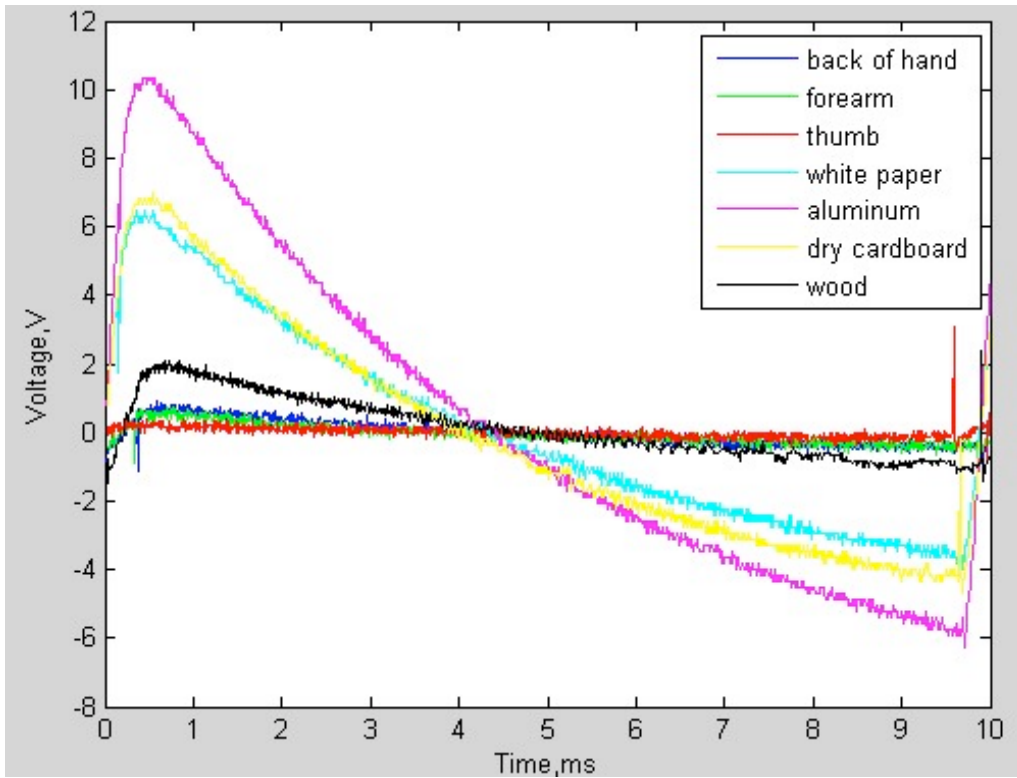
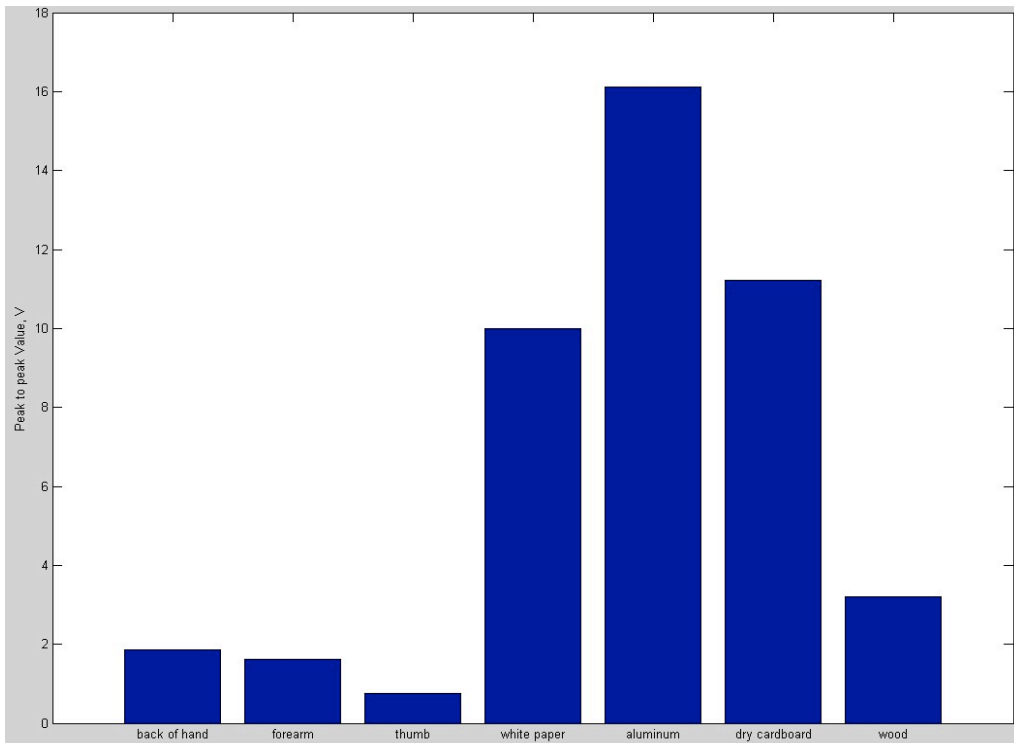**Figure 5.10** *The synchronized signals of different materials when the amplification factors are 1100.*



**Figure5.11** *The peak to peak values of measurement signals of the different materials.*

## 5.4 Conclusions

In summary, a new portable opto-thermal radiometry instrument has been designed and developed. It centres on a modulated broadband Infrared Emitter and a room temperature PbS detector. The drive circuit for the Infrared Emitter and the pre-amplifier circuit for PbS detector have been designed, and the corresponding PCB modules are developed. Different materials, such as the back of hand, forearm, thumb, white paper, aluminum, dry cardboard and wood etc. have been used for test measurements. The test results show that the peak to peak values of signals detected by PbS detector of the different materials are significantly different. The different peak to peak values reflect the different infrared reflection and infrared radiation intensity of different materials. More studies are needed, in order to have better understanding of the signals and extract infrared emission information from the different materials.

## Chapter 6 Skin Hydration and Solvent Penetration Experiments

The aims of this chapter are to develop new measurement methodologies to study the skin hydration and solvent penetrations by using OTTER, AquaFlux and capacitive contact imaging based on Fingerprint sensors, and to have a better understanding of capacitive imaging measurements. Five different experiments are performed in this chapter. The results show the capacitive contact imaging based on Fingerprint sensors is a powerful tool for studying skin hydration and skin solvent penetrations. Combining with AquaFlux and OTTER we can also get extra information on skin barrier functions.

## 6.1 Tape Stripping Measurements by Using AquaFlux and Fingerprint Sensor

The purpose of this experiment is to investigate how the skin hydration and TEWL (trans-epidermal water loss) change at different depth of skin. The skin hydration is measured by using capacitive contact imaging based on Fingerprint sensor and TEWL is measured by AquaFlux. The different skin depth is achieved by using traditional tape stripping, where each tape strip removes a several layers of skin cells.

In this measurement, two skin sites marked as control site and stripping site were chosen on the left volar forearm near the elbow. The tape stripping was only performed on the stripping site, with control site as a reference. The ambient temperature was 23.0$^{\circ}$C and relative humidity (RH) is 49%. The hydration measurements and the TEWL measurements were performed before and after the tape stripping, with totally 14 strips applied. Each tape strip removes about 1 $\mu m$ thickness of skin, so 14 strips removes about 14 $\mu m$ thickness of skin. This is still

well within stratum corneum, which is about 20 $\mu m$ in thickness on volar forearm.



| Before | strip 1 | strip 2 | strip 4 |



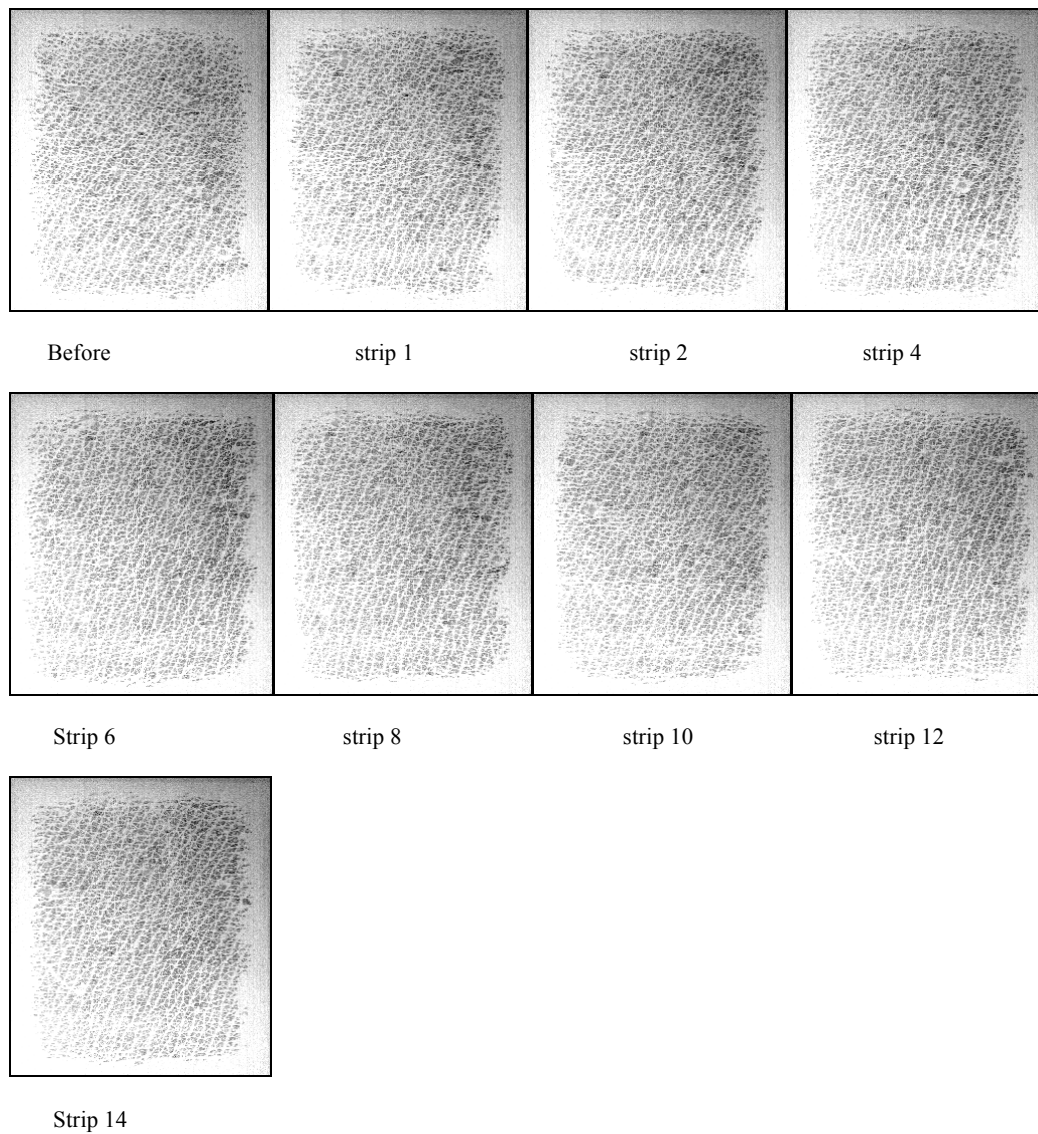| Strip 6 | strip 8 | strip 10 | strip 12 |



Strip 14

***Figure 6.1:*** *Capacitive skin images of control site before and after tape stripping.*

Figure 6.1 shows the images of the control site, before and after tape stripping. The results show that the capacitive images of the control site did not change very much during the measurements.
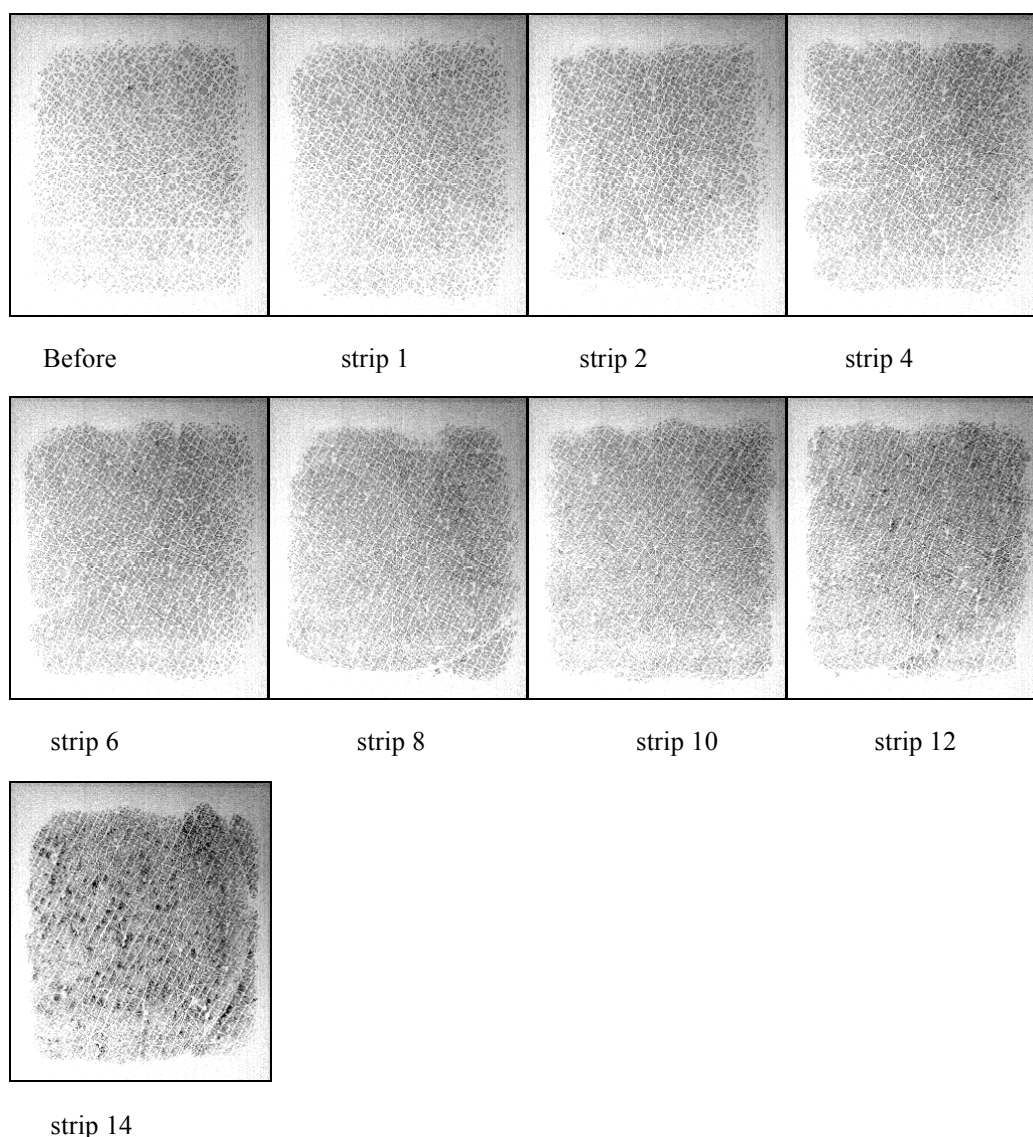
Before          strip 1          strip 2          strip 4

strip 6          strip 8          strip 10          strip 12

strip 14

**Figure 6.2** *Capacitive skin images of the stripping site before and after tape stripping.*

Figure 6.2 shows the capacitive images of the stripping site, before and after the tape stripping. Major changes start after 10<sup>th</sup> tape strip.

Figure 6.3 show the corresponding grayscale values of the capacitive images shown in Figure 6.1 and 6.2. The grayscale values on control site did not change very much as expected. The grayscale values on stripping site increased slowly at beginning and then increased significantly after the tenth strip.
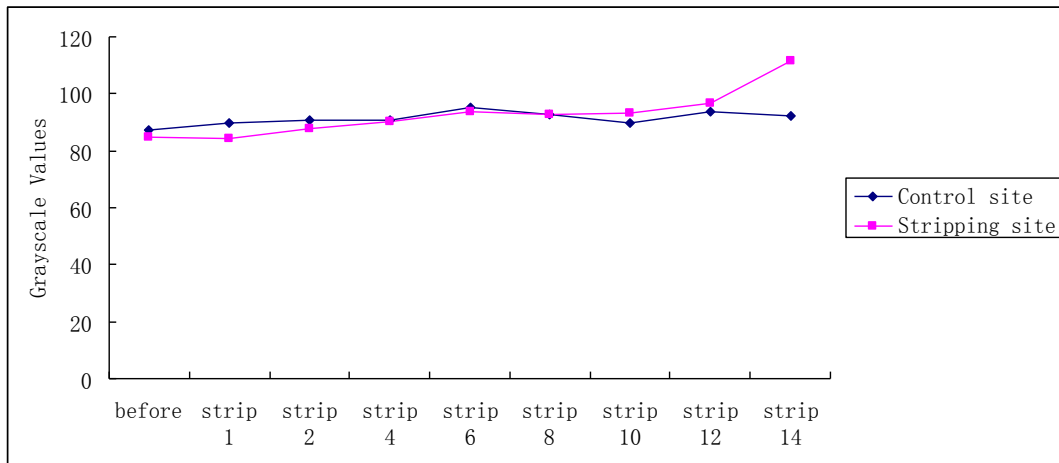
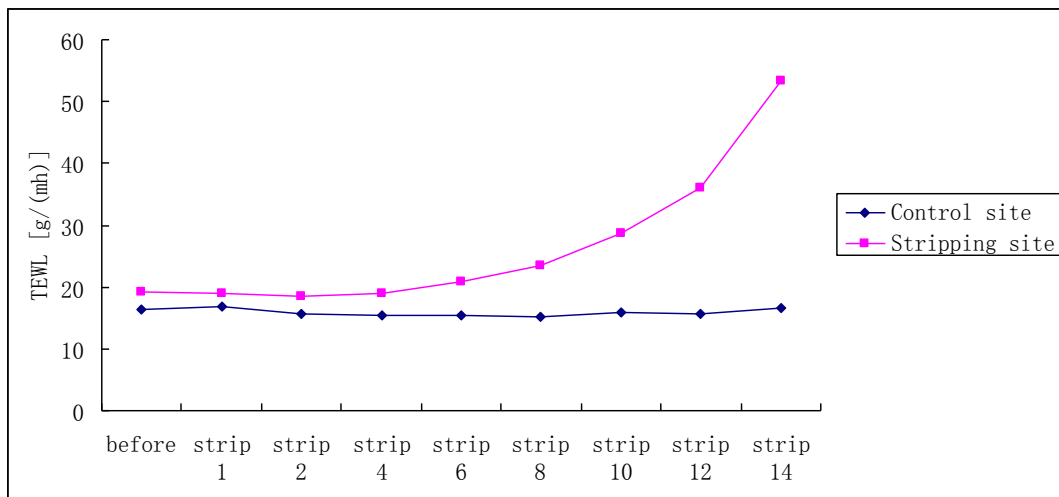***Figure 6.3*** *The grayscale values before and after tape stripping.*



***Figure 6.4***: *TEWL values before and after tape stripping.*

Figure 6.4 show the corresponding TEWL values on two different skin sites measured by AquaFlux. Again, the TEWL values on control site did not change very much as expected. The TEWL values on stripping site increased slowly at the beginning and then increased significantly after the tenth strip. It is interesting to point out that both Figure 6.3 and 6.4 agree with other very well, which suggests that stratum corneum is dry outside and wet inside, and the skin barrier function is not on the stratum corneum surface, but at the inside of stratum corneum, somewhere around 10 $\mu m$ in depth.

## 6.2 Skin Solvent Penetration with Tape Stripping

The purposes of this experiment are to investigate the potential of combining OTTER and capacitive contacting imaging based on Fingerprint Sensors for solvent penetration measurements, and to investigate the solvent concentration depth profiles.

Three different skin sites on left volar forearm are chosen for study, two as test sites and one as control site. Two solvents, DMSO (dimethyl sulfoxide) and EG (ethylene glycol) are used in this study. First, a small amount of solvent is applied to the left volar forearm for 5 minutes. After the skin surface is wiped dry, tape stripping is performed, with totally 12 strips. OTTER and capacitive contact imaging measurements are performed both before and after the solvent applications, and after each tape strip. Two different wavelengths (9.5 $\mu m$ and 13.1 $\mu m$) are chosen for each measurement of OTTER.



**Before**          **After (DMSO)**          **Strip 1**          **Strip 2**

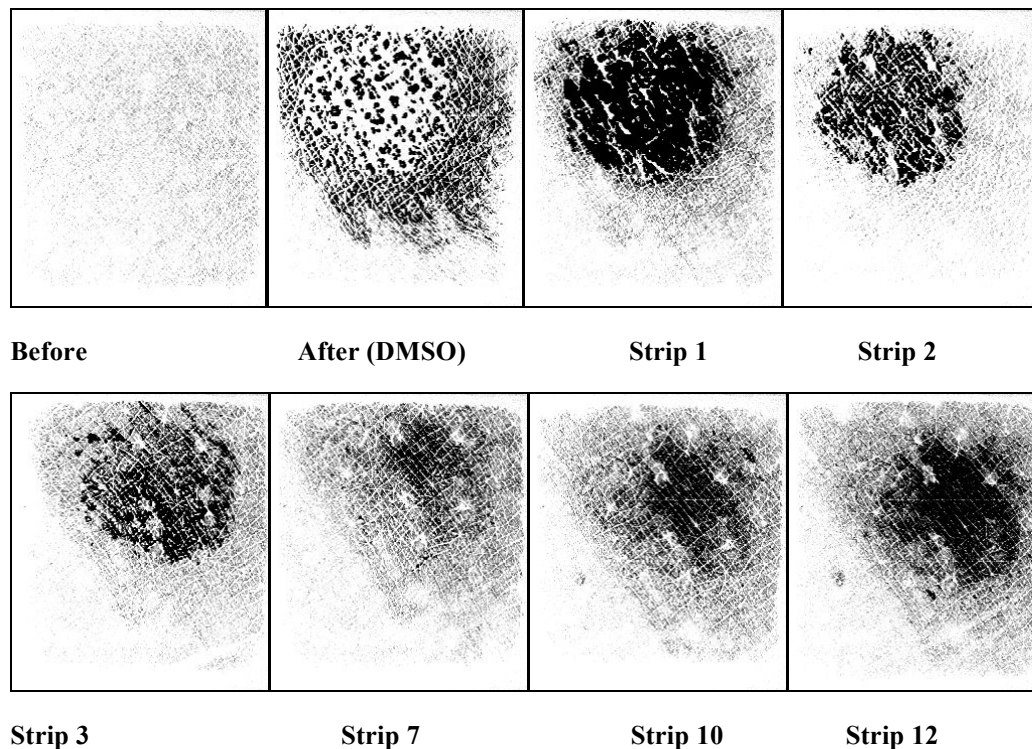**Strip 3**          **Strip 7**          **Strip 10**          **Strip 12**

***Figure 6.5*** *Capacitive skin images before and after DMSO applications, and subsequently during tape stripping.*

89

Figure 6.5 shows the grayscale capacitive skin images of the skin test site before and after DMSO application, and subsequently during tape stripping. The increased darkness after DMSO application reflects the DMSO concentration in skin, which then gradually decreased as tape stripping number increased. This suggests DMSO concentration level decreases as depth increases. DMSO residue is still visible after 10 strips. However, the increase of darkness after 10th tape strip is due to increase of water content, as Fingerprint sensor can not differentiate between water and DMSO.
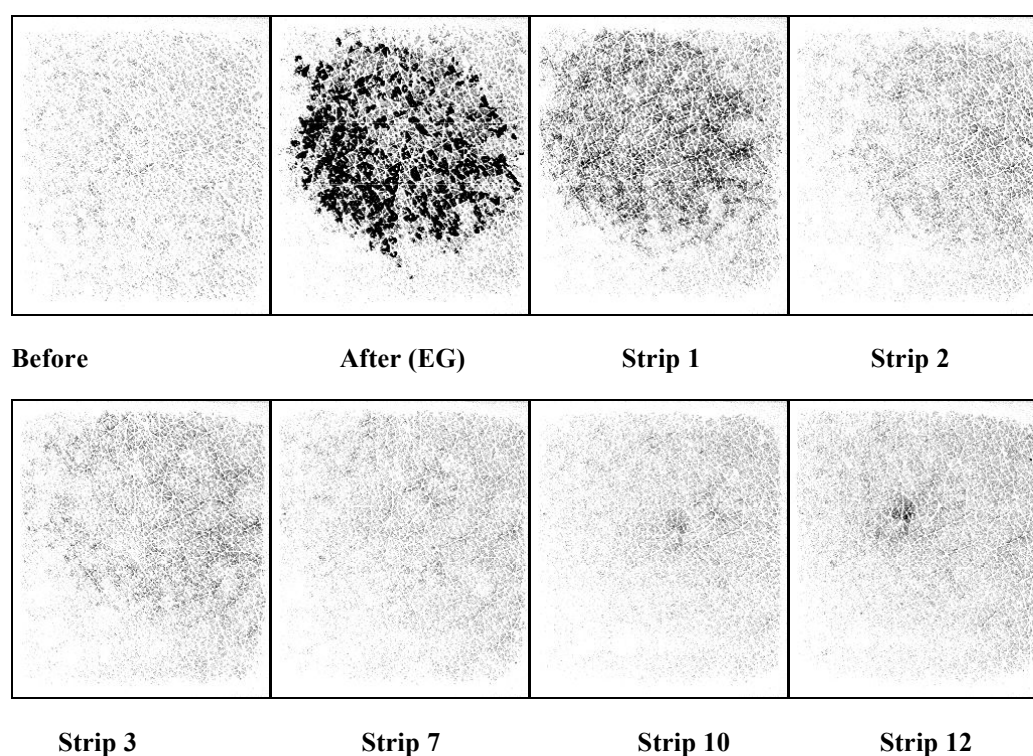


| **Before** | **After (EG)** | **Strip 1** | **Strip 2** |

| **Strip 3** | **Strip 7** | **Strip 10** | **Strip 12** |

**Figure 6.6** *Capacitive skin images before and after EG applications, and subsequently during tape stripping.*

Figure 6.6 shows the grayscale skin images before and after EG applications, and subsequently during tape stripping. Again, the increased darkness after EG application reflect the EG concentration level in stratum corneum. Compared to Figure 6.5, this figure indicates EG penetrates less and shallower than DMSO, as DMSO residue is

still visible after 10 strips ($\sim 10 \, \mu m$), whilst EG residue disappears after 5 strips ($\sim 5 \, \mu m$).



| Before | After | Strip 1 | Strip 2 |
|--------|-------|---------|---------|

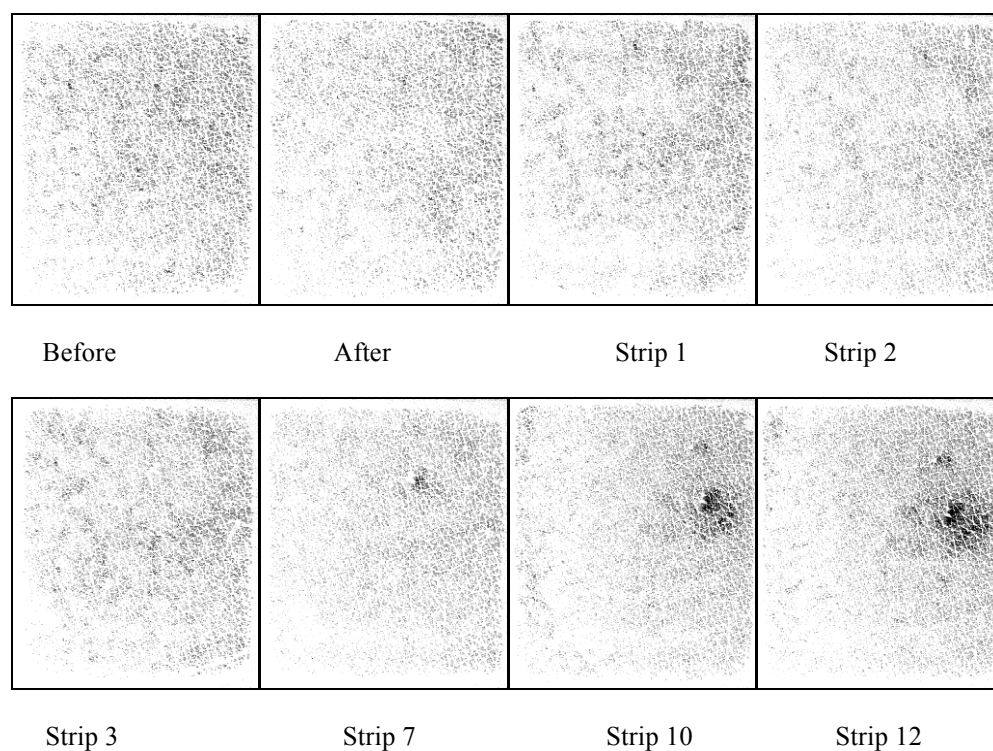| Strip 3 | Strip 7 | Strip 10 | Strip 12 |
|---------|---------|----------|----------|

**Figure 6.7** *Fingerprint skin images for the control sites*
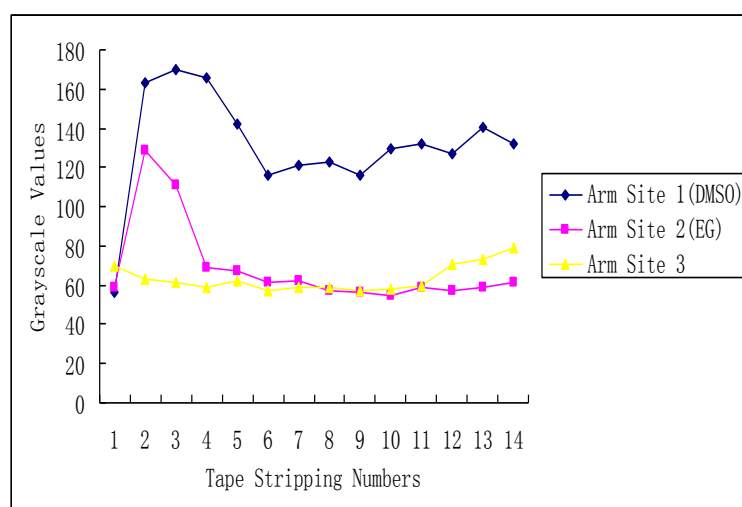


**Figure 6.8** *Grayscale values from Fingerprint sensor before and after DMSO / EG application and*

*subsequent tape stripping*

Figure 6.7 shows the images of the control site, before and subsequently after tape stripping. The gradually increased darkness reflects the increase of water content during tape stripping, and major increase is about after 10th tape strip. Figure 6.8 shows the corresponding grayscale values of the images shown in Figure 6.5, 6.6 and 6.7. The results also confirm that DMSO penetrated more and deeper into stratum corneum that EG.
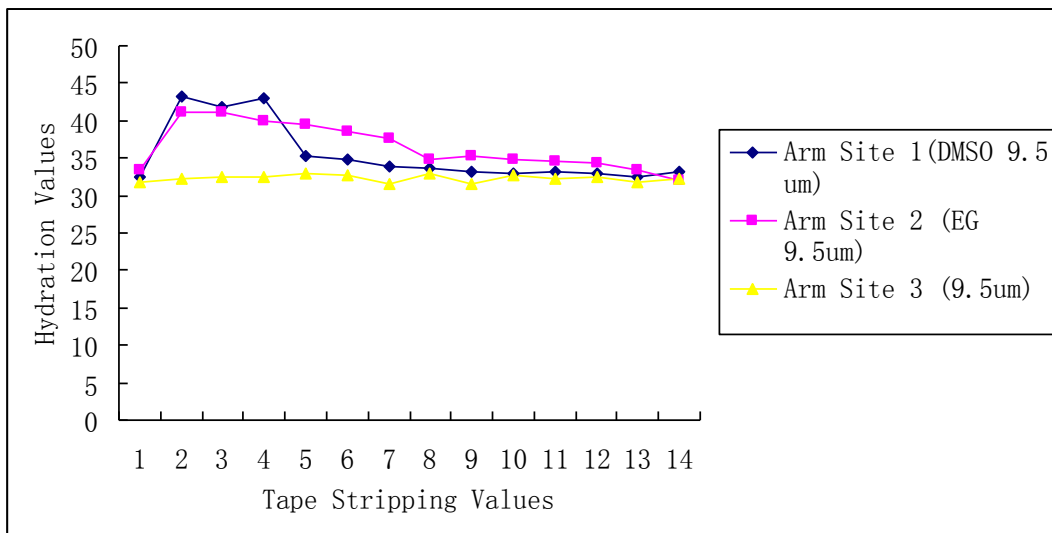


**Figure 6.9** *Concentration results from OTTER (9.5 $\mu m$) before and after DMSO / EG application and*
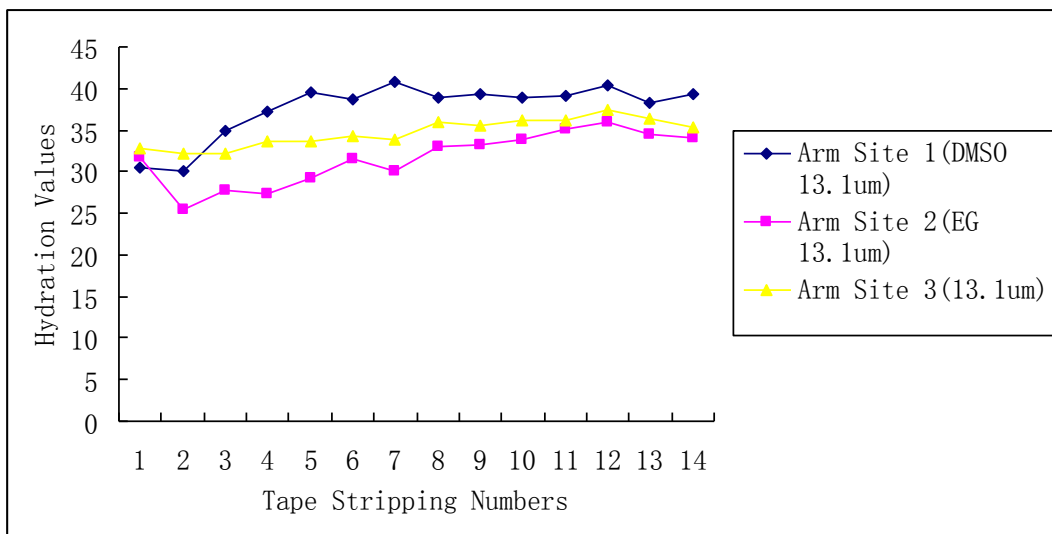
*subsequent tape stripping*



**Figure 6.10** *Concentration results from OTTER (13.1 $\mu m$) before and after DMSO / EG application*

*and subsequent tape stripping*

Figure 6.9 shows the OTTER results from three different skin sites at 9.5 *μm* detection wavelength, which reflects more about the solvent content in skin. Figure 6.10 shows the OTTER results from three different sites at 13.1 *μm* detection wavelength, which clearly reflect more about the water content in skin.
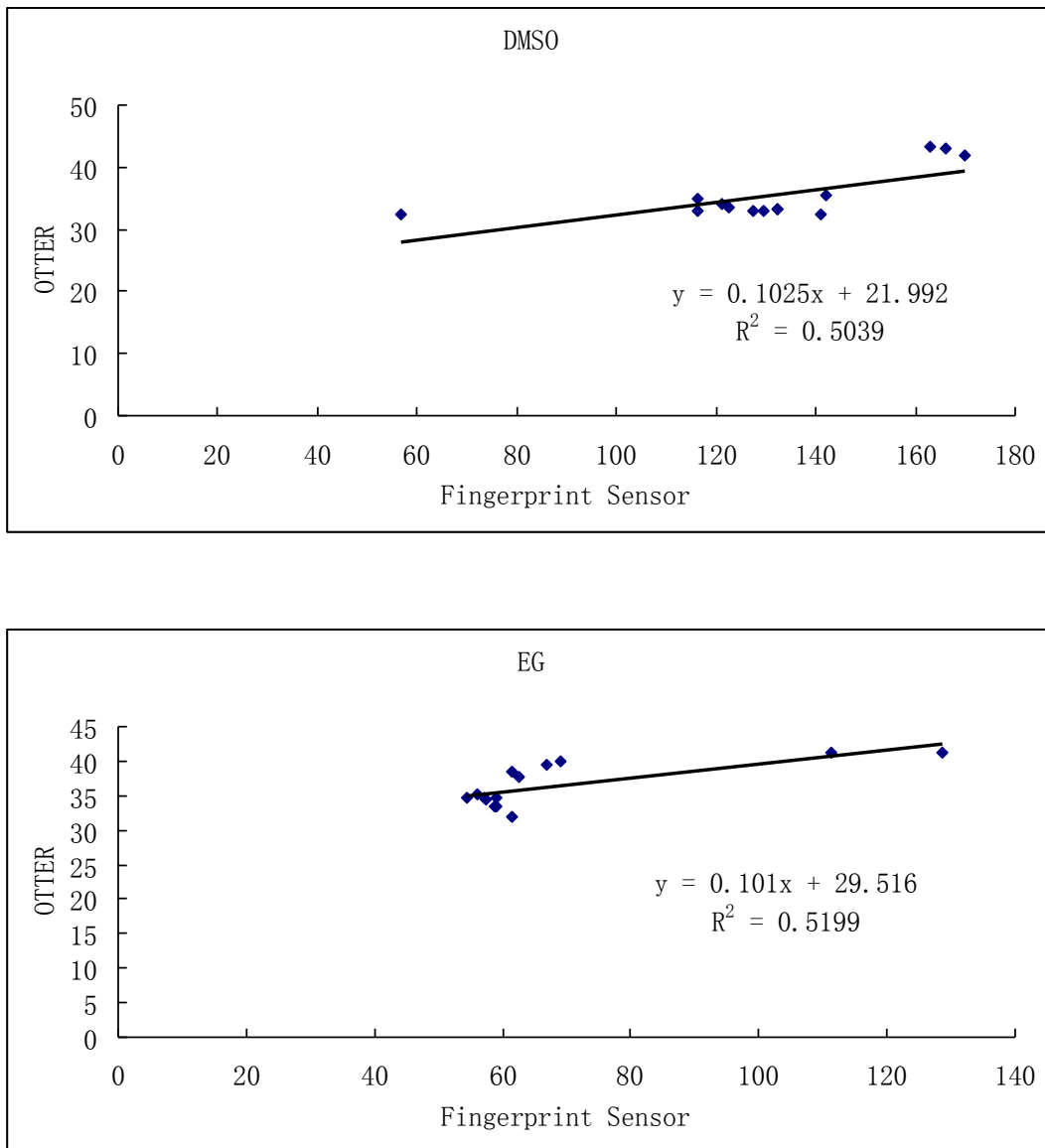


*Figure 6.11 The correlations between Fingerprint sensor and OTTER*

Figure 6.11 shows the correlations between capacitive contact imaging based on Fingerprint sensors and OTTER. The results indicate that there are some correlations

between grayscale results and OTTER results. The reason that fitted curves are not going through the origin (0, 0) is because that the fingerprint sensor is not calibrated; our next task is to calibrate technology so that we can get the absolute solvent quantity results.

## 6.3 Measuring the Detection Depth of Fingerprint Sensor

The purpose of this experiment is to measure the detection depth of Fingerprint Sensor.
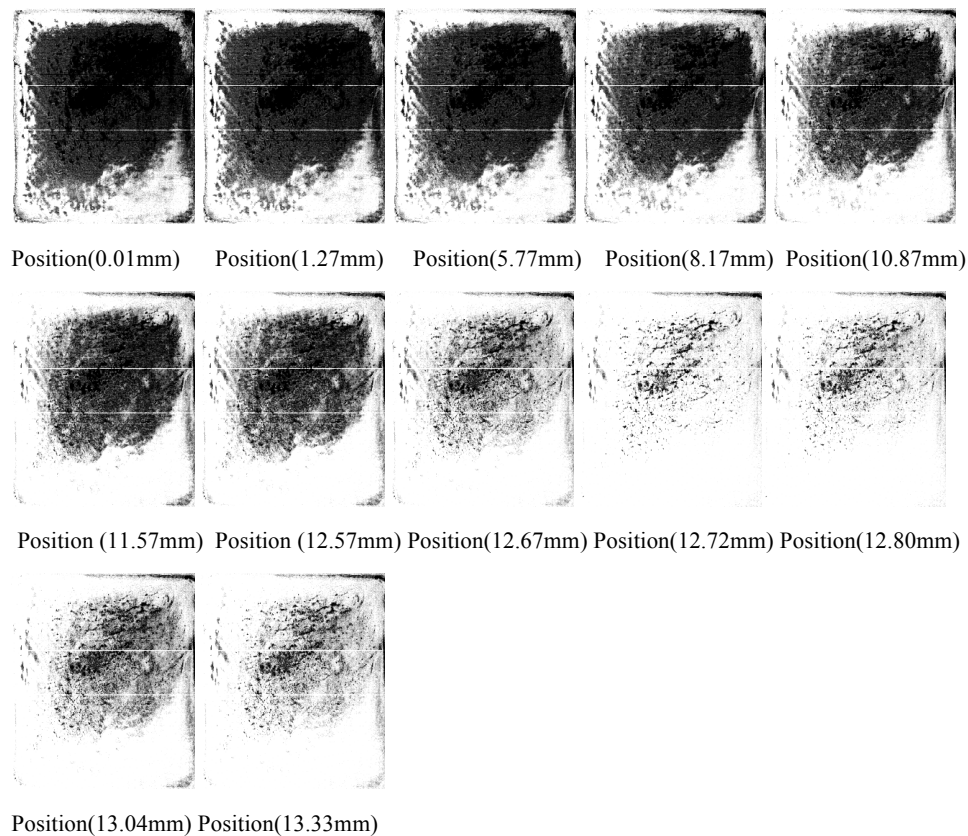
Position(0.01mm)    Position(1.27mm)    Position(5.77mm)    Position(8.17mm)    Position(10.87mm)

Position (11.57mm)  Position (12.57mm)  Position(12.67mm)  Position(12.72mm)  Position(12.80mm)

Position(13.04mm)  Position(13.33mm)

***Figure 6.12*** *Capacitive cheese images at different distances from the Fingerprint sensor surface.*

A piece of sliced cheddar cheese (Tesco supermarket, $3cm \times 3cm$ in area, and $3mm$ in thickness) and Fingerprint Sensor are fixed on a micro-positioner. At first, the piece of cheese is in good contact with the Fingerprint Sensor surface, then use micro-positioner to gradually pull the cheese away from the Fingerprint Sensor surface, and

images were recorded at each position.

Figure 6.12 shows the images at different distances from the Fingerprint sensor surface. It can be seen visually from this figure that the image quality becomes worse at position  ($12.67\,mm$). The little black dots after position ($12.67\,mm$) are due to cheese residue left on the Fingerprint sensor surface at the beginning of the measurements.
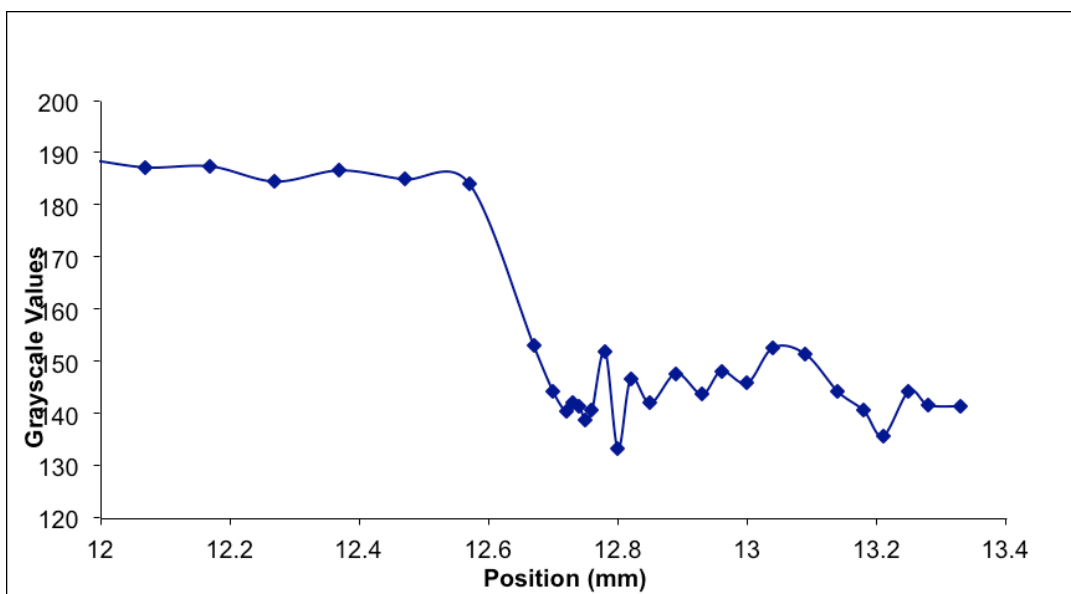


*Figure 6.13 Grayscale values at different distances from the Fingerprint sensor surface*

Figure 6.13 shows the corresponding grayscale values from Fingerprint sensor at different positions. From the above two figures, it suggests that position ($12.67\,mm$) is likely to be the position that cheese is just above to leave the sensor surface, and position ($12.72\,mm$) is likely the position that cheese is just out of the sensor detection range, the distance between the two position is about $50\,\mu m$, which agrees well with the expected detection depth ($50\,\mu m$) according to the sensor pixel geometry.

## 6.4 The effect of Discharge time, Discharge current, and Gain

The purpose of this experiment is to investigate the effects of the Fingerprint sensor's three parameters, namely, discharge time, discharge current and gain.
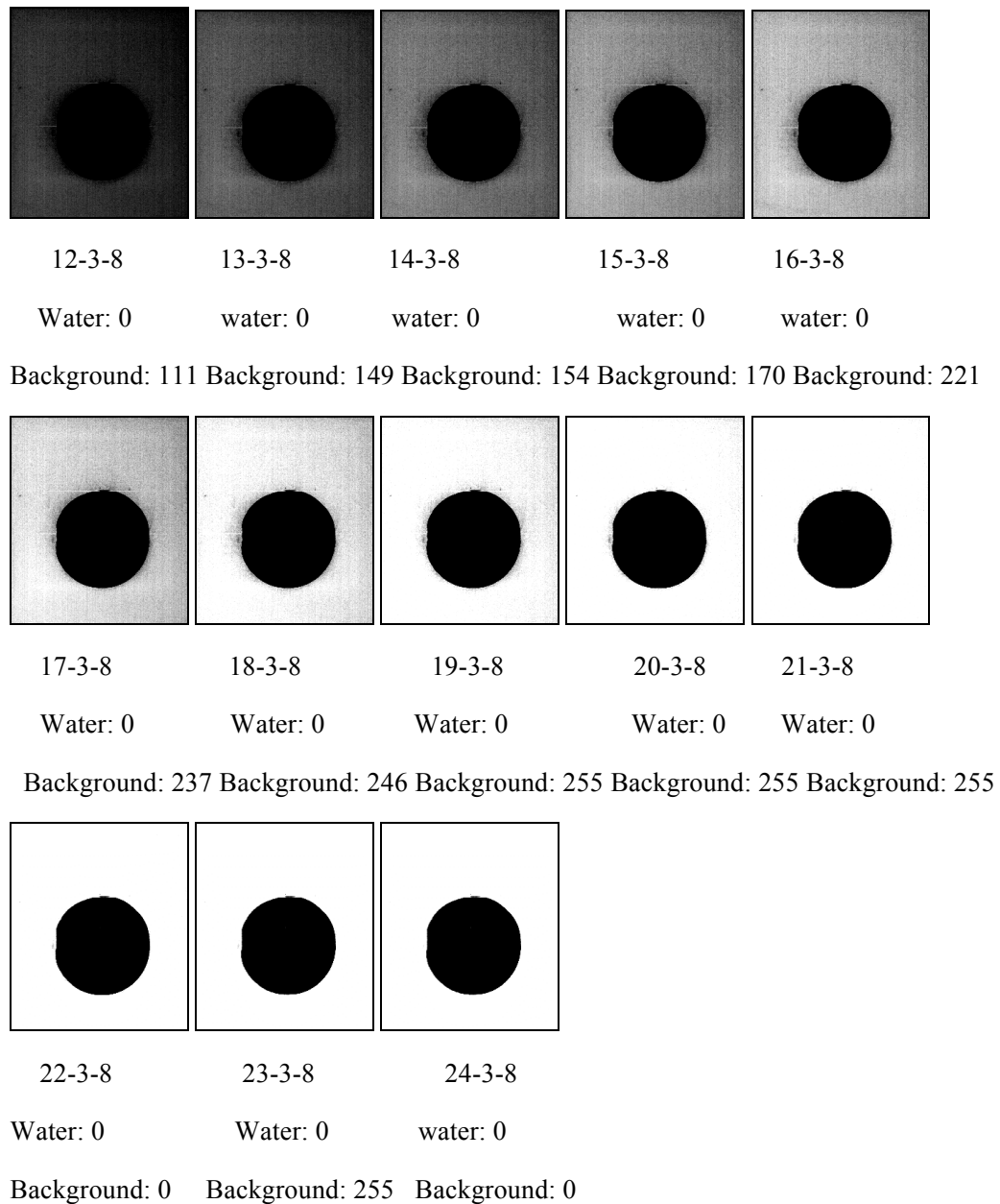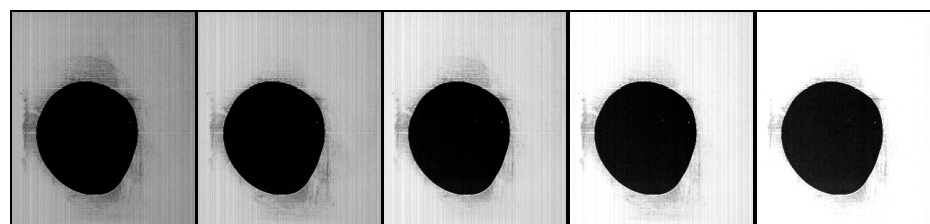


| 12-3-8 | 13-3-8 | 14-3-8 | 15-3-8 | 16-3-8 |
|--------|--------|--------|--------|--------|
| Water: 0 | water: 0 | water: 0 | water: 0 | water: 0 |

Background: 111 Background: 149 Background: 154 Background: 170 Background: 221



| 17-3-8 | 18-3-8 | 19-3-8 | 20-3-8 | 21-3-8 |
|--------|--------|--------|--------|--------|
| Water: 0 | Water: 0 | Water: 0 | Water: 0 | Water: 0 |

Background: 237 Background: 246 Background: 255 Background: 255 Background: 255



| 22-3-8 | 23-3-8 | 24-3-8 |
|--------|--------|--------|
| Water: 0 | Water: 0 | water: 0 |

Background: 0   Background: 255   Background: 0

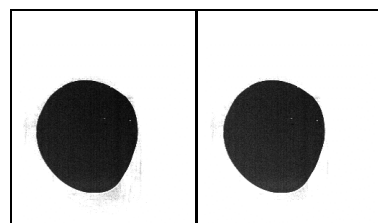**Figure 6.14** *Images of water at different discharge times, with discharge current =3, and gain =8.*

At first, a drop of water is added on the surface of the Fingerprint sensor. Then, the images are recorded at different values of the discharge time, discharge current and gain.

Figure 6.14 shows the images with different discharge times. For example, in 12-3-8, 12 is the discharge time's value, 3 is the discharge current's value and 8 is the gain's value. Below each image are the grayscale values for water and background. When the discharge time's value is 22, water is most clear in the picture and the contrast between water and background is best, so the results show that discharge time 22 gives the best image.



| 12-4-11 | 13-4-11 | 14-4-11 | 15-4-11 | 16-4-11 |
|---------|---------|---------|---------|---------|
| Water: 0 | Water: 0 | Water: 0 | Water: 0 | Water: 0 |

Background: 164 Background: 189 Background: 221 Background: 240 Background: 255



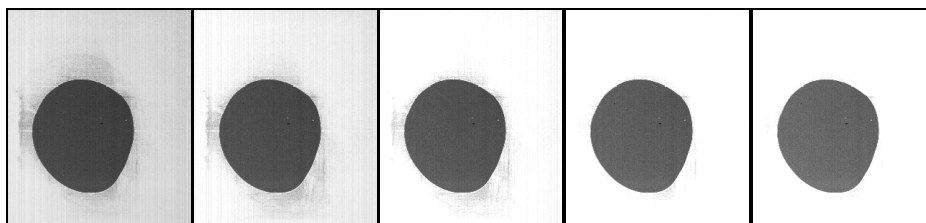| 17-4-11 | 18-4-11 |
|---------|---------|
| Water: 36 | Water: 43 |

Background: 255 Background: 255

***Figure 6.15** Images of water at different discharge times.*

Figure 6.15 shows the images with changing discharge time. For example, in 12-4-11, 12 is the discharge time's value, 4 is the discharge current's value and 11 is the

discharge gain's value. Below each image are the grayscale values for water and background. The results show that discharge time 18 gives the best image.
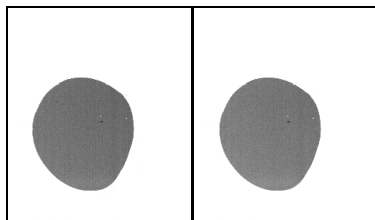
Figure 6.16 shows the images with changing discharge time. For example, in 12-4-10, 12 is the discharge time's value, 4 is the discharge current's value and 10 is the gain's value. Below each image are the grayscale values for water and background. The results show that discharge time 15 gives the best image.

| 12-4-10 | 13-4-10 | 14-4-10 | 15-4-10 | 16-4-10 |
| --- | --- | --- | --- | --- |
| Water: 80 | Water: 96 | Water: 107 | Water: 116 | Water: 130 |
| Background: 224 | Background: 240 | Background: 255 | Background:255 | Background: 255 |

| 17-4-10 | 18-4-10 |
| --- | --- |
| Water: 145 | Water: 153 |
| Background: 255 | Background: 255 |

**Figure 6.16** *Images of water at different discharge times.*

From the three different experiments indicated above, it can be concluded that discharge time 22 gives the best image.

Figure 6.17 shows the images at different discharge currents. For example, in 22-2-8, 22 is the discharge time's value, 2 is the discharge current's value and 8 is the gain's value. Below each image are the grayscale values for water and background. The results show that discharge current 3 gives the best image.
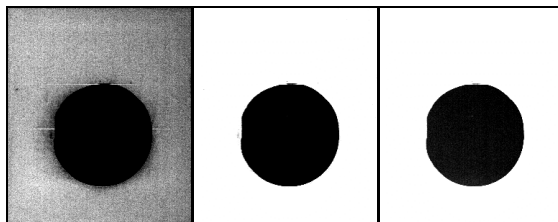


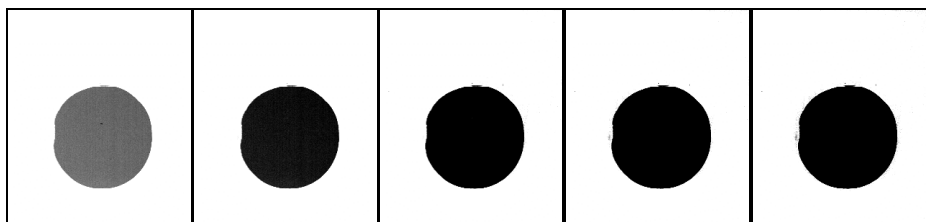22-2-8          22-3-8          22-4-8

Water: 0          water: 0          water: 0

Background: 233   Background: 255   Background: 255

*Figure 6.17 Image by changing the discharge current's value*



22-3-10          22-3-11          22-3-12          22-3-13     22-3-14

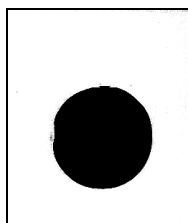Water: 120       water: 44        water: 0         water: 0    water: 0

Background: 255 Background: 255 Background: 255 Background: 255 Background: 255



22-3-15

Water: 0

Background: 255

*Figure 6.18 Image by changing the discharge gain's value*

Figure 6.18 shows the images with changing gain. For example, in 22-3-10, 22 is the discharge time's value, 3 is the discharge current's value and 10 is the gain's value. Below each image are the grayscale values for water and background. The results show that gain 11 gives the best image.

Figure 6.19 shows the images with changing discharge gain. For example, in 15-4-8, 15 is the discharge time's value, 4 is the discharge current's value and 8 is the gain's value. Below each image are the grayscale values for water and background. The results show that discharge gain 11 gives the best image.
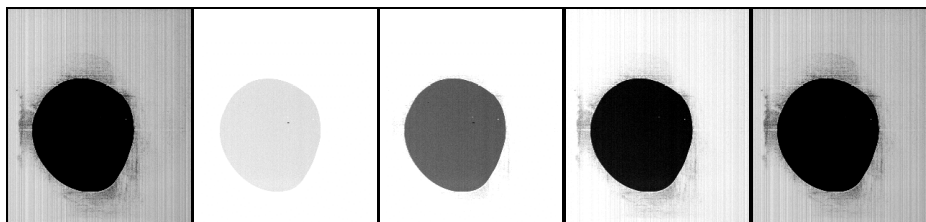


      15-4-8            15-4-9         15-4-10          15-4-11          15-4-12

   Water: 0       Water: 227     Water: 115     Water: 21        Water: 0

Background: 208 Background: 255 Background: 255 Background: 245 Background: 193
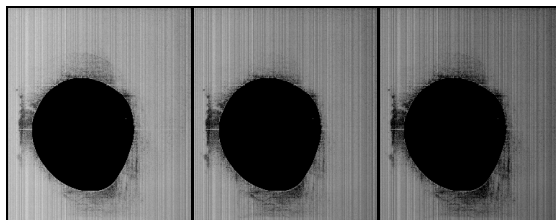


   15-4-13            15-4-14            15-4-15

   Water: 0       Water: 0       Water: 0

Background: 161 Background: 146 Background: 123

*Figure 6.19 Image by changing the discharge gain's value*

From the three different experiments indicated above, it can be concluded that the gain 11 gives the best image.

## 6.5 Solvent Penetrating Through The Membrane

The purpose of this experiment is to evaluate the suitability of using capacitive contact imaging based on Fingerprint Sensors to study the permeation of selected solvents through silicone membranes. Six different solvents with different dielectric constants were selected for this test (Table 6.1)

| Solvent | Dielectric constant |
|---|---|
| Water | 80 |
| Ethanol | 24.55 |
| Butanol | 18 |
| Heptanol | 11.75 |
| Decanol | 8.1 |
| Propylene Glycol | 32.1 |

***Table 6.1** the dielectric constants for the used solvents.*

A piece of silicone membrane ($100 \, \mu m$ in thickness) is fixed on the Fingerprint Sensor surface and a regular hexagonal steel sleeve was put on the top of membrane. At first, a small quantity of butanol is dropped into the chamber of the sleeve; when the sleeve is full, the measurement started and continued for about 1000 sec. The same process is repeated for decanol, heptanol, PG., water and ethanol.

Figure 6.20 shows the capacitive images after butanol application. It can be seen visually from this figure that butanol starts to penetrate through the membrane at about 440s.

Figure 6.21 shows the capacitive images after decanol application. It can be seen visually from this figure that decanol has not penetrated through the membrane.
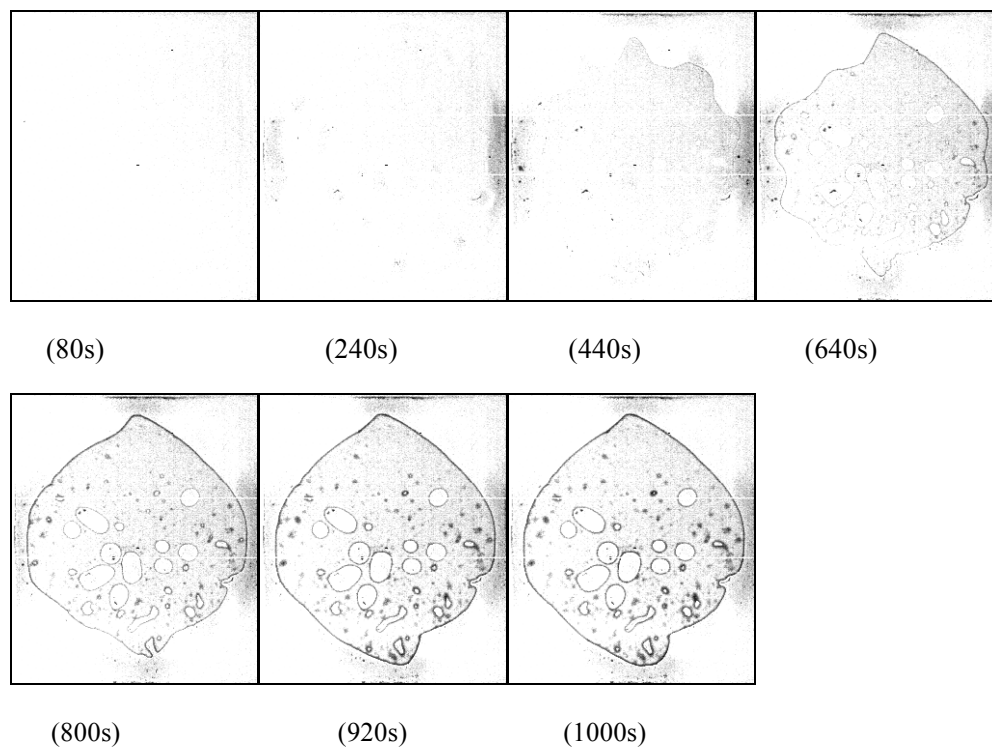
|              |              |              |              |
|:------------:|:------------:|:------------:|:------------:|
| (80s)        | (240s)       | (440s)       | (640s)       |

| (800s)       | (920s)       | (1000s)      |
|:------------:|:------------:|:------------:|

**Figure 6.20** *Capacitive images after butanol application.*



|              |              |              |              |
|:------------:|:------------:|:------------:|:------------:|
| (80s)        | (240s)       | (440s)       | (640s)       |

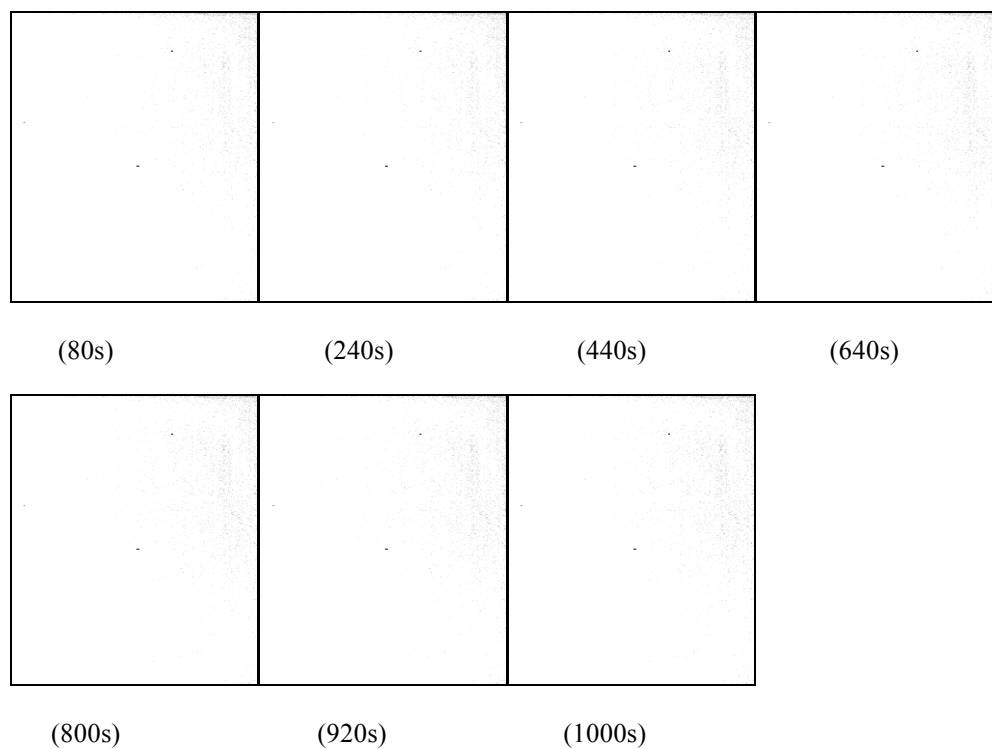| (800s)       | (920s)       | (1000s)      |
|:------------:|:------------:|:------------:|

**Figure 6.21** *Capacitive images after decanol application.*

Figure 6.22 shows the capacitive images after heptanol application. The same as the decanol showed above, the penetration ability of heptanol through the membrane is also very limited. It has not penetrated the membrane during the experimental time.
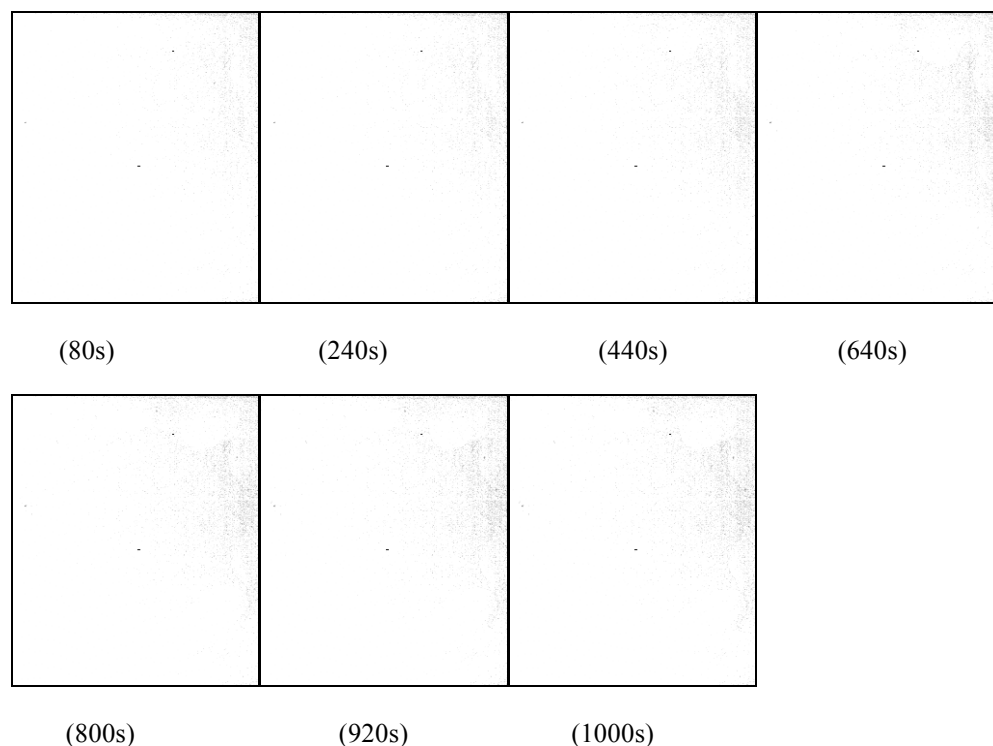


|  (80s)  |  (240s)  |  (440s)  |  (640s)  |



|  (800s)  |  (920s)  |  (1000s)  |

***Figure 6.22*** *Capacitive images after heptanol application.*

Figure 6.23 shows the capacitive images after PG application. It can be seen visually from this figure that PG starts to penetrate through the membrane at about 240s.
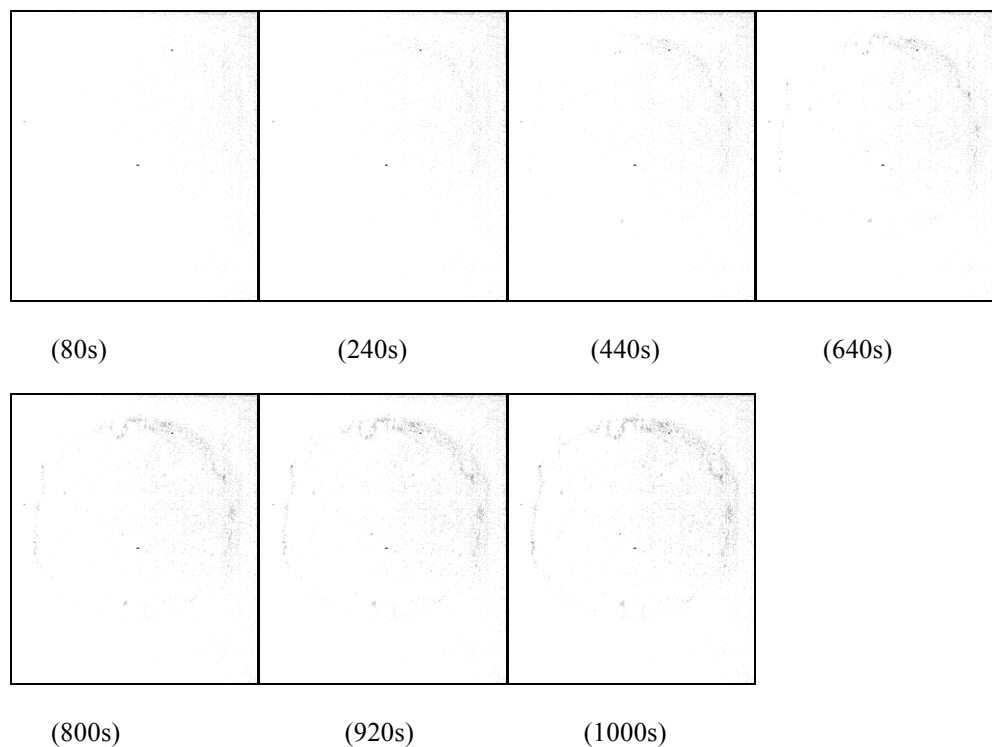
(80s)          (240s)          (440s)          (640s)



(800s)          (920s)          (1000s)

**Figure 6.23** *Capacitive images after PG application.*

Figure 6.24 shows the capacitive images after water application. It can be seen visually from this figure that water starts to penetrate through the membrane very quickly and has strong penetration ability.
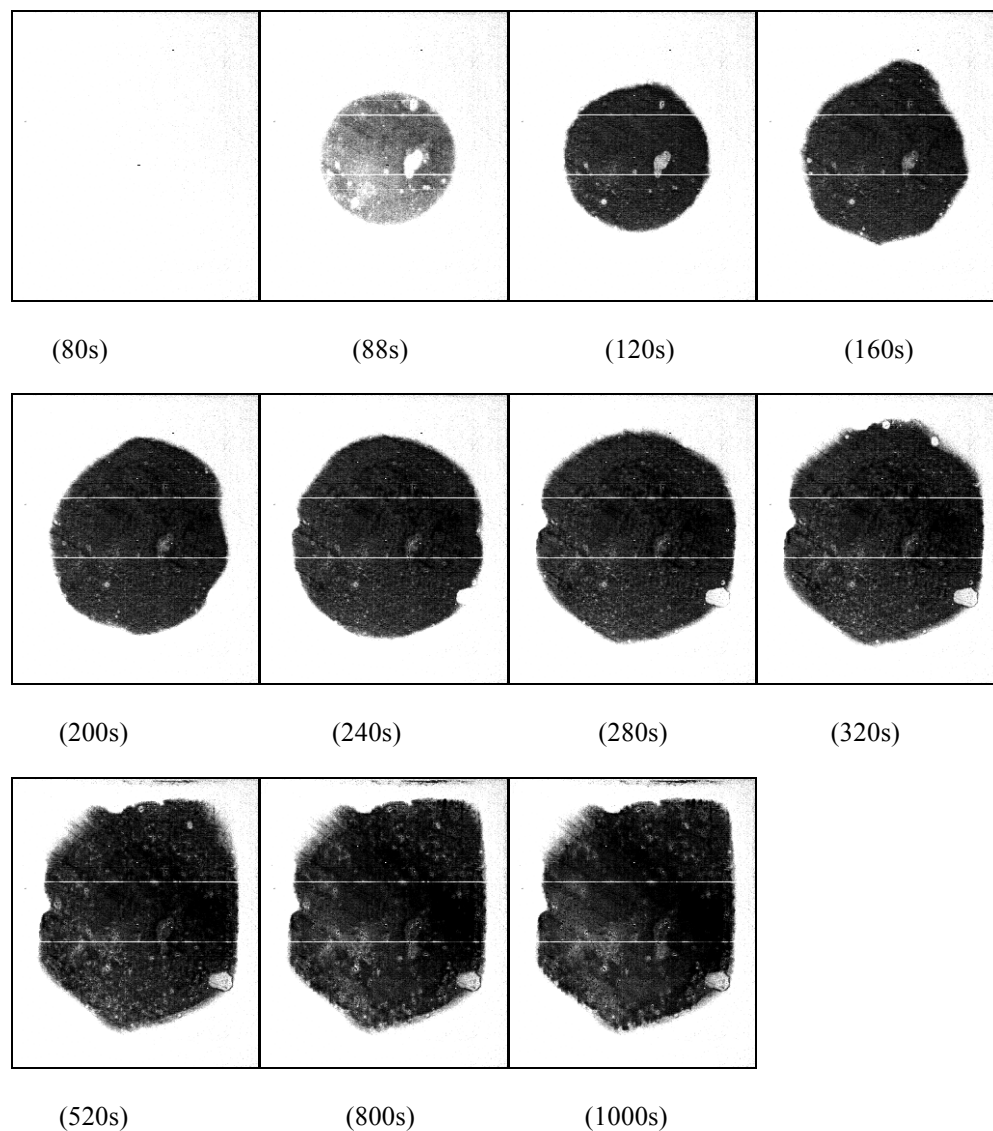
|  (80s)  |  (88s)  |  (120s)  |  (160s)  |



|  (200s)  |  (240s)  |  (280s)  |  (320s)  |



|  (520s)  |  (800s)  |  (1000s)  |

**Figure 6.24** *Capacitive images before and after water application.*

Figure 6.25 shows the capacitive images after ethanol application. It can be seen visually from this figure that ethanol starts to penetrate through the membrane at about 160s and has strong penetration ability, too.
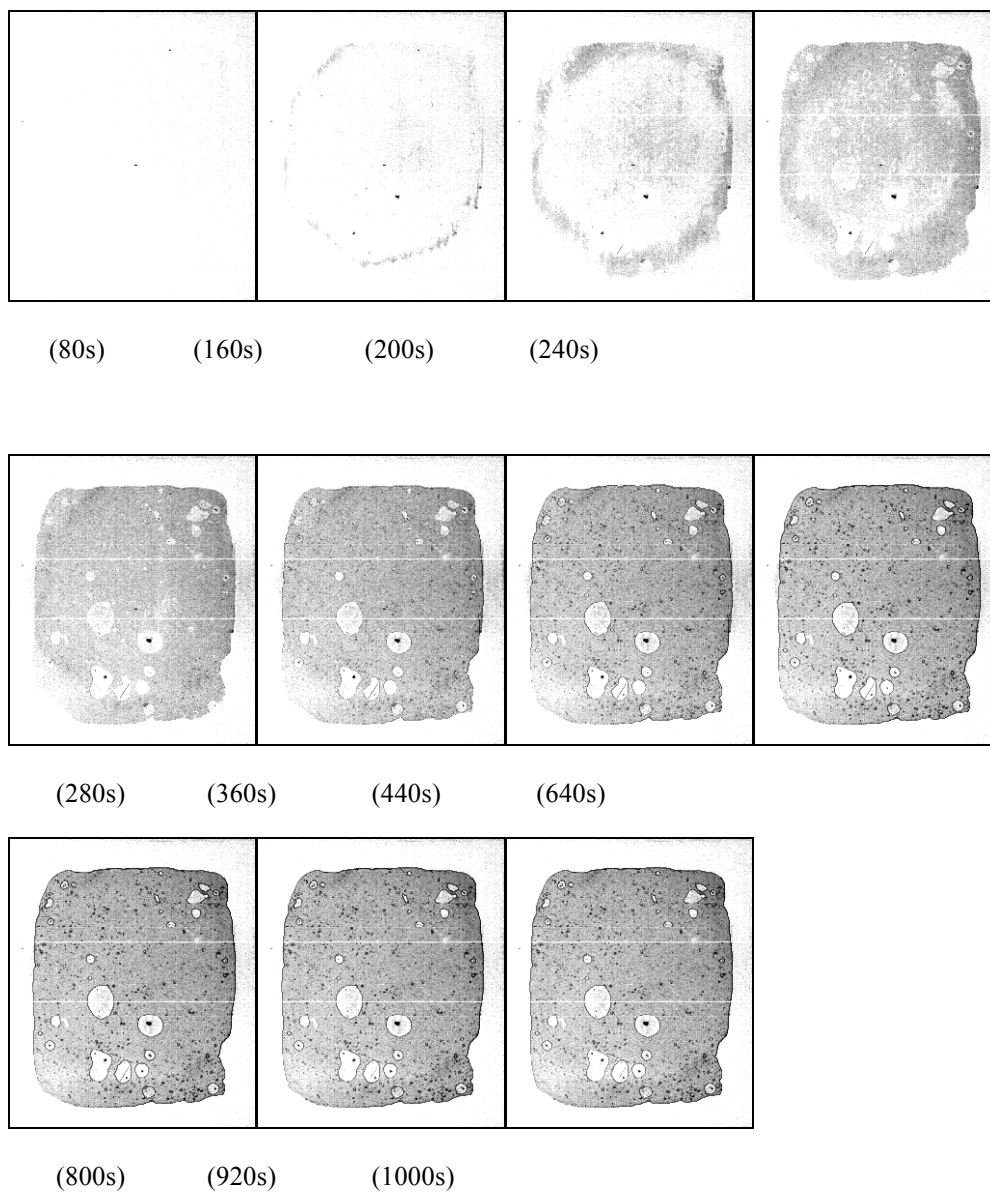
(80s)　　　　(160s)　　　　(200s)　　　　(240s)

(280s)　　　　(360s)　　　　(440s)　　　　(640s)

(800s)　　　　(920s)　　　　(1000s)

***Figure 6.25*** *Capacitive images after ethanol application.*

***Figure 6.26*** *Grayscale values for Fingerprint images before and after butanol application*



***Figure 6.27*** *Grayscale values for Fingerprint images before and after decanol application*

Figure 6.26 and 6.27 show the grayscale values for the capacitive images after butanol and decanol applications.
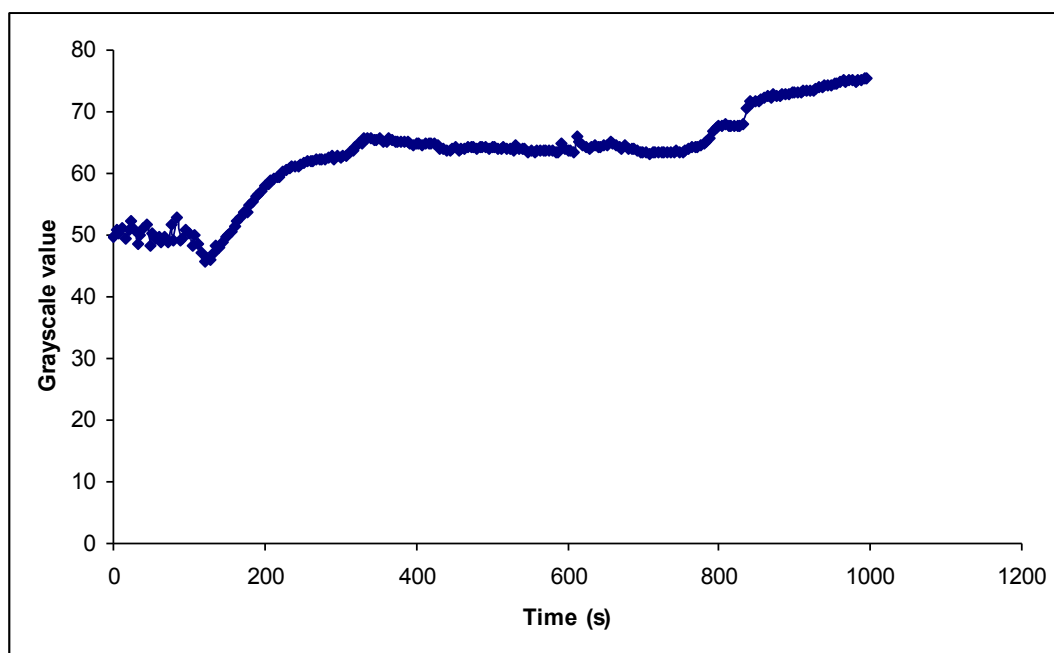
***Figure 6.25*** *Grayscale values for Fingerprint images before and after heptanol application*
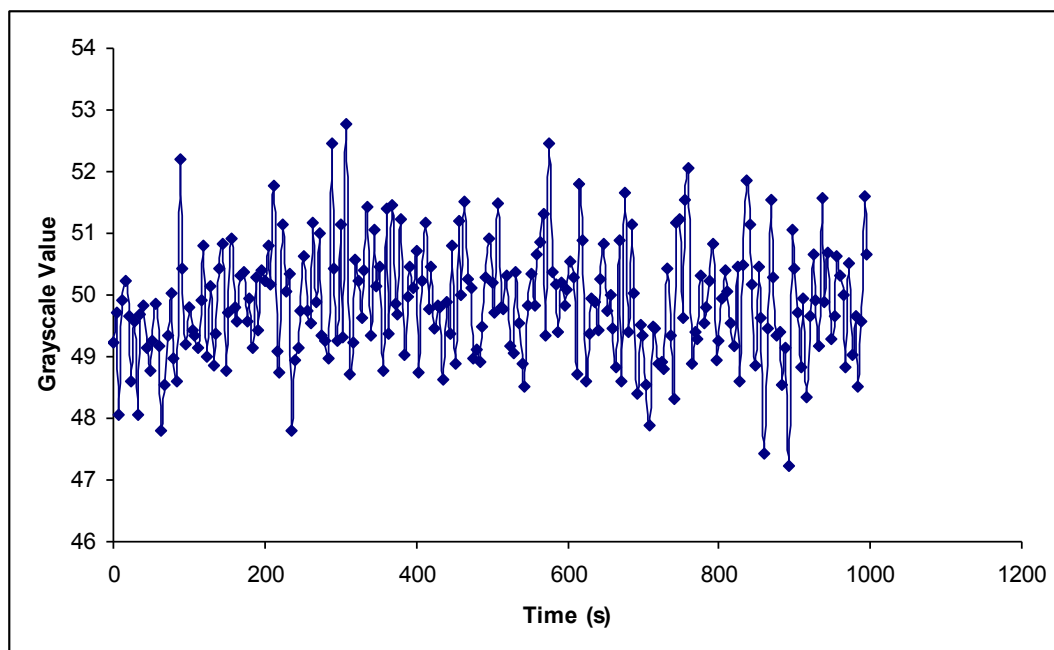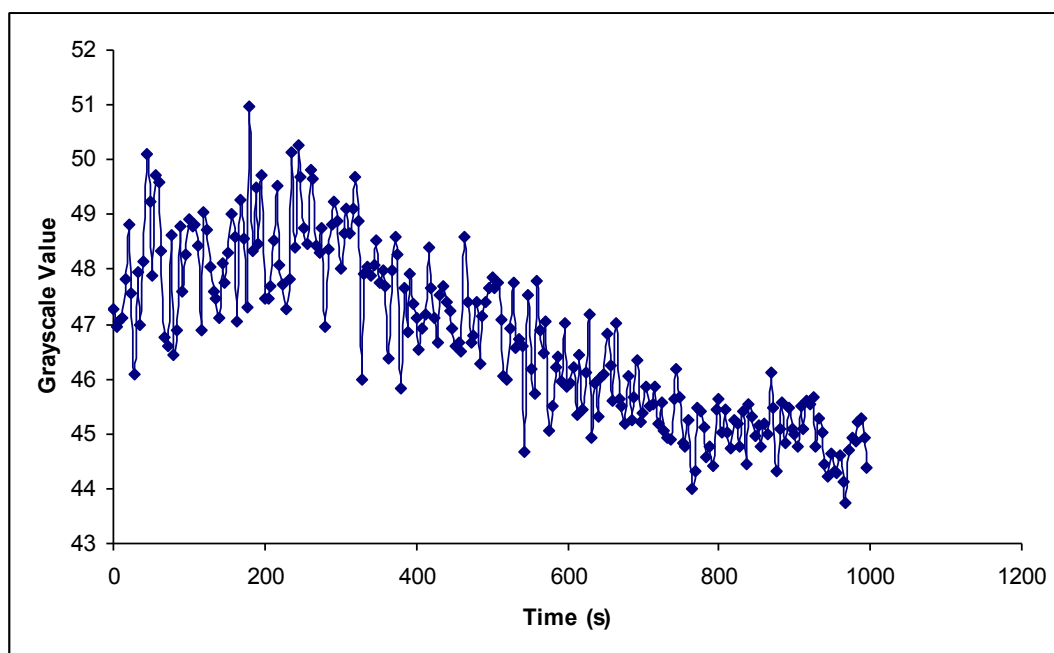


***Figure 6.26*** *Grayscale values for Fingerprint images before and after PG application*

Figure 6.25 and 6.26 show the grayscale values for the capacitive images after heptanol and PG applications.

***Figure 6.27*** *Grayscale values for Fingerprint images before and after water application*



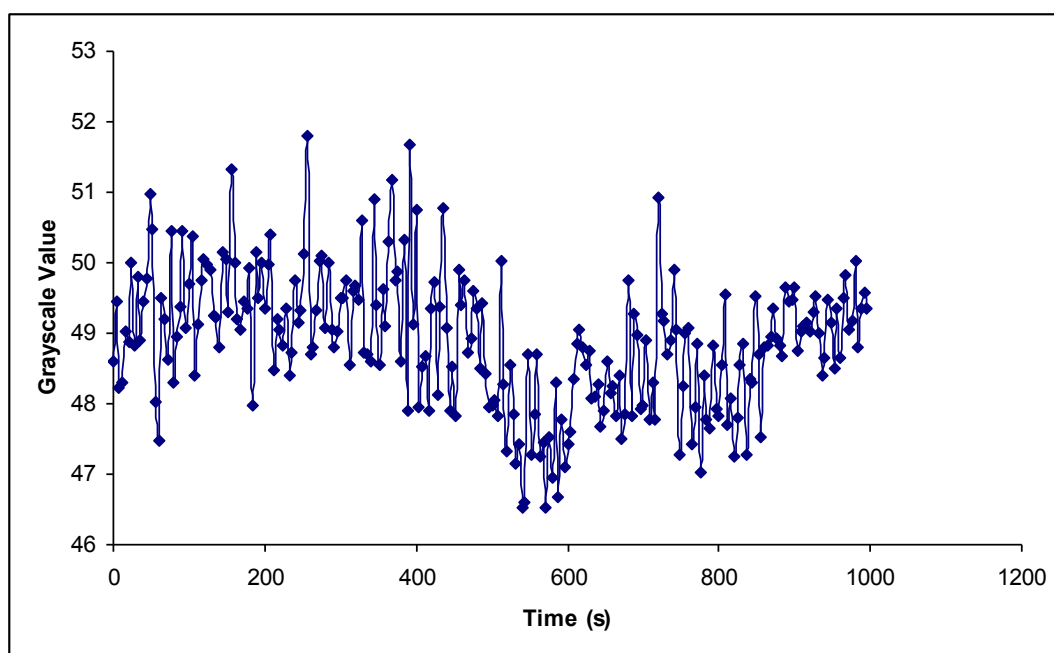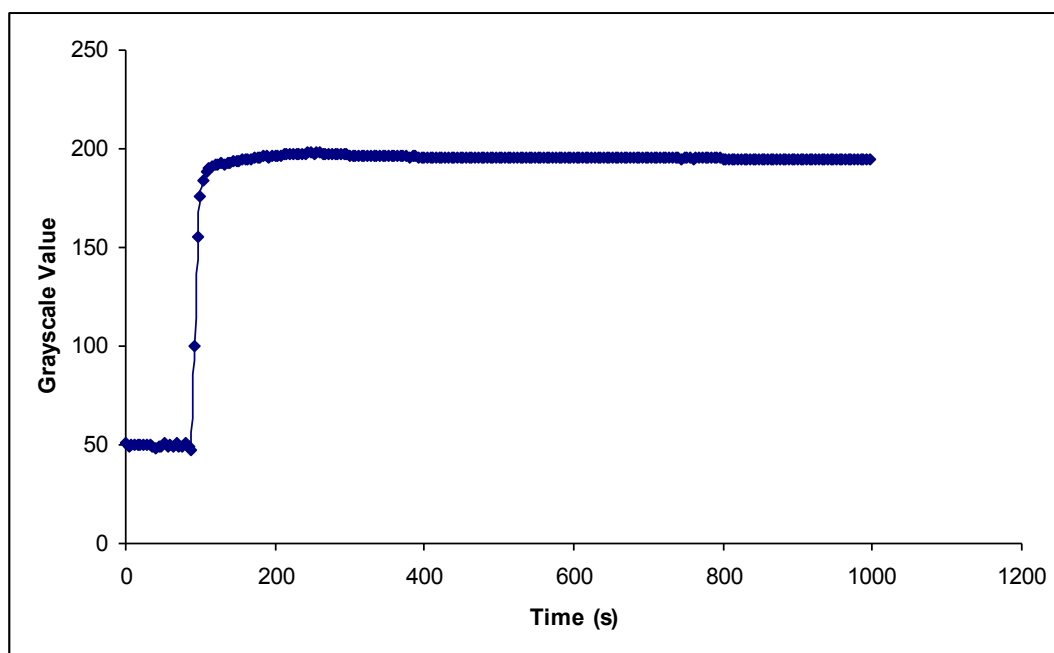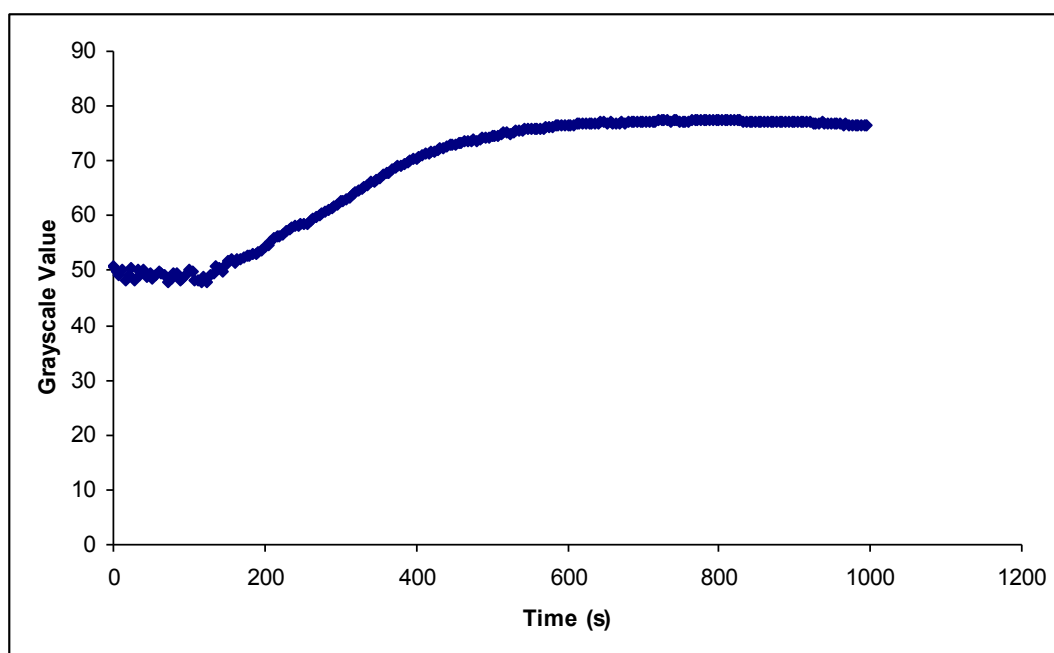***Figure 6.28*** *Grayscale values for Fingerprint images before and after ethanol application*

Figure 6.27 and 6.28 show the grayscale values for the capacitive images after water and ethanol applications.

## 6.6 Conclusion

In summary, five experiments are performed in order to develop new methodologies for skin hydration and solvent penetration measurements by using OTTER, AquaFlux and capacitive contact imaging based on Fingerprint sensors, as well as to have better understanding of capacitive contact imaging measurements. The results show that the combination of AquaFlux and capacitive contact imaging is very useful for studying the skin hydration and TEWL changed at different skin depth through tape stripping. The results also show that the combination of OTTER and capacitive contact imaging is very useful for studying the solvent penetration through skin, and again, through tape stripping, solvent concentration depth profiles within skin can be obtained. The first two experiments have demonstrated that capacitive contact imaging could be a powerful tool for skin hydration and solvent penetration measurements, due to its imaging capabilities. Although there are other imaging techniques, such as stimulated Raman scattering microscopy [92], can be used for solvent penetration, our capacitive contact imaging is much cheaper, smaller and easier to operate. In order to have a better understanding of the capacitive contact imaging measurements, the detection depth of Fingerprint sensors, and effects of Fingerprint sensors' configuration parameters, namely, discharge time, discharge current and gain, were also studied, and the best values were chosen for the measurements. Finally, solvent penetration through silicone membrane was studied, six solvents with different dielectric constants were used, and the results demonstrated that capacitive contact imaging can be effectively used for this kind of measurements.

# Chapter 7 The Comparison of Three Algorithms for Image Retrieval

In chapter 3, an effective image retrieval algorithm based on Gabor wavelet transform has been developed for retrieving skin images, particularly for grayscale capacitive skin images. It is also found that the Grey level co-occurrence matrix (GLCM) algorithm, described in chapter 4, can also be used for image retrieval purposes. The aim of this chapter is conduct a comparison study, in order to compare these two algorithms with other existing algorithms, such as Principal Component Analysis (PCA), in order to understand better the performance of each algorithm, the pros and cons of each algorithm, and to find out which algorithm is suitable for what types of images. This chapter will first introduce the background of Principal Component Analysis (PCA), and then show the comparison results.

## 7.1 The theory of Principal Component Analysis (PCA)

The following introduces the principles of Principal Component Analysis (PCA), Grey level co-occurrence matrix (GLCM) and Gabor wavelet transform.

### 7.1.1 The Principal Component Analysis (PCA)

The Principal Component Analysis (PCA) [93-97] is a common and effective method based on the covariance matrix of variable to process, compress and extract the information. It provides a roadmap for how to reduce a complex data set to a lower dimension and has been abundantly applied in face recognition.

The basic principle of this method is: it uses the K-L transformation to extract the main ingredient of face images, which constitutes the eigenfaces space, and then projects the test images and training images to this space and gets two different groups of projection coefficients. Finally, it recognizes the image by comparing their projection coefficients. The detailed implementation steps are as follows [98, 99]:

1. Assuming that the training database consists of k samples, each sample size is $m \times n$, and then the training sample matrix is represented as:

$$x = (x_1, x_2, ..., x_k)^T \tag{7.1}$$

where the $x_i$ is a one-dimensional sample whose number of rows is $m \times n$ and the number of columns is 1.

2. Define the sample average vector

$$\psi = \frac{1}{k} \sum_{i=1}^{k} x_i \tag{7.2}$$

3. Calculate the difference between each sample and the sample average vector

$$d_i = x_i - \psi \qquad i = 1, 2, ..., k \tag{7.3}$$

4. Compute the covariance matrix

$$C = \frac{1}{k} \sum_{i=1}^{k} d_i d_i^T = \frac{1}{k} AA^T$$

$$A = (d_1, d_2, ..., d_k) \tag{7.4}$$

5. Compute the eigenvector $V_i$ and eigenvalue $\lambda_i$ of the covariance matrix, select p feature values which are greater than 1 and their corresponding eigenvectors to constitute the eigenfaces space

$$w = (u_1, u_2, ..., u_p) \tag{7.5}$$

where $u_i = \frac{1}{\sqrt{\lambda_i}} AV_i (i = 1, 2, ..., p)$

6. Project the difference between each sample and the sample average vector to the eigenfaces space

$$\Omega_i = w^T d_i \, (i = 1,2,...k) \tag{7.6}$$

7. Project the difference between the test sample $\Gamma$ and the sample average vector to the eigenfaces space

$$\Omega^\Gamma = w^T (\Gamma - \psi) \tag{7.7}$$

8. Calculate the Euclidean distance $\varepsilon_i$ between $\Omega_i$ and $\Omega^\Gamma$

$$\varepsilon_i^{\,2} = \left\| \Omega_i - \Omega^\Gamma \right\|^2 \, (i = 1,2,...,k) \tag{7.8}$$

*7.1.2 The principals of Grey level co-occurrence matrix (GLCM) and Gabor wavelet transform*

The principals of Grey level co-occurrence matrix (GLCM) and Gabor wavelet transform have been given the detailed introduction in chapter 3 and 4. After extracting the feature vectors, according to 7.1.1, using the Euclidean distance to measure the similarity.

**7.2 Results and Discussions**

As the first step to evaluate the algorithms, a database containing sixty images are used in this study, the database images are in JPEG format, including thirteen different digital colour human face images, four different digital colour skin cancer images, four different digital colour skin disease images and the rest of them are skin greyscale capacitive images which were captured from Fingerprint sensor [48]. Figure 7.1 shows some sample images from the database.
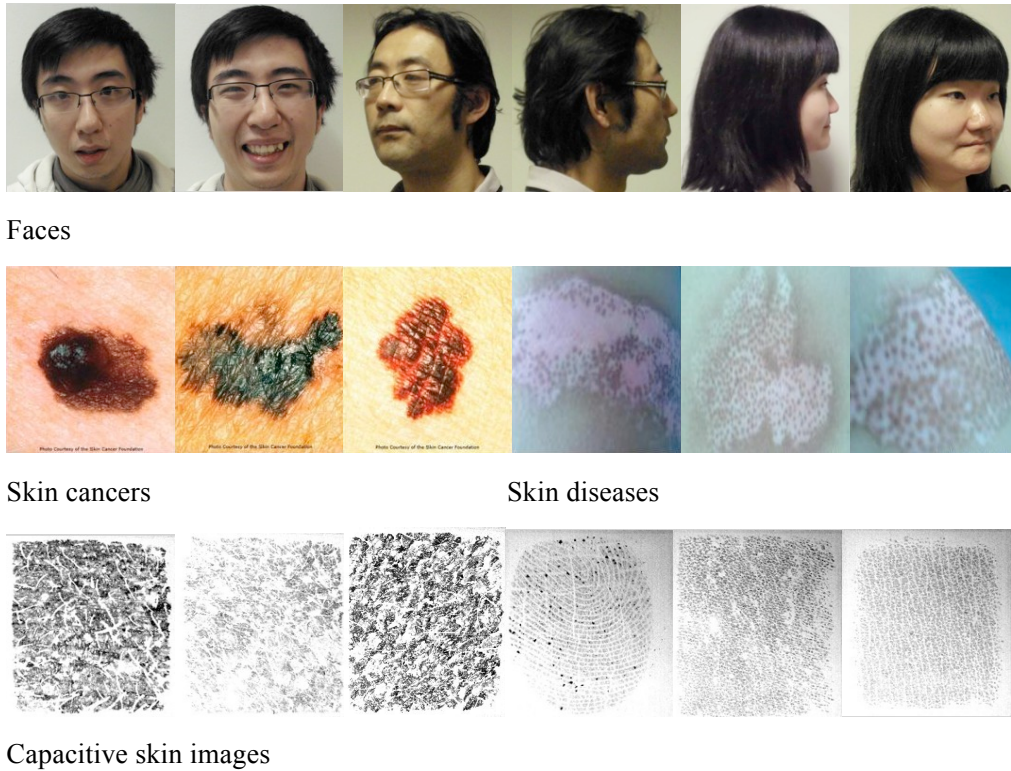
Faces



Skin cancers                                    Skin diseases



Capacitive skin images

***Figure 7.1*** *Sample images from the database*

Figure 7.2 shows the GUI (graphical user interface) for preliminary results on image retrieval using the PCA, GLCM and Gabor wavelet transform. In the GUI window, the upper left image in the first row is the query image and the others in the second row are the results of retrieved images from the image database. The best three retrieved images are shown for illustration. The retrieved images are ranked in descending order according to the similarity of their feature vectors to those of the query image, i.e. the most similar, the second similar, and the third similar images. In this study, for reasons of simplicity, the query images are also from the database, and therefore the most similar result should always be the image itself. Time 1 represents the total time used to calculate the feature vectors of all the images in the database and Time 2 shows the computing time used to calculate the similarity of the feature vectors of all the images in the database to the feature vectors of the query image.
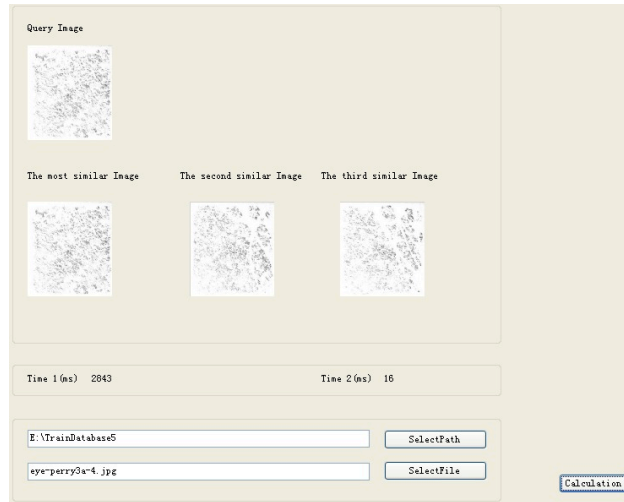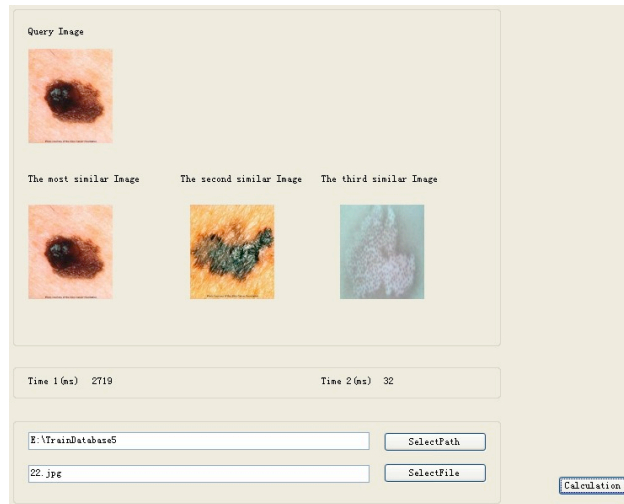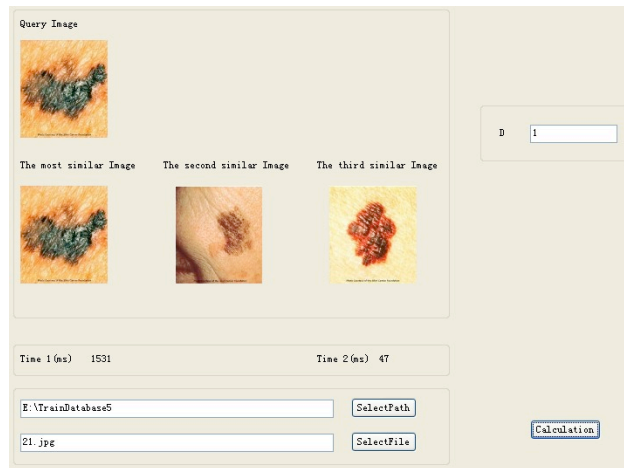
(a)
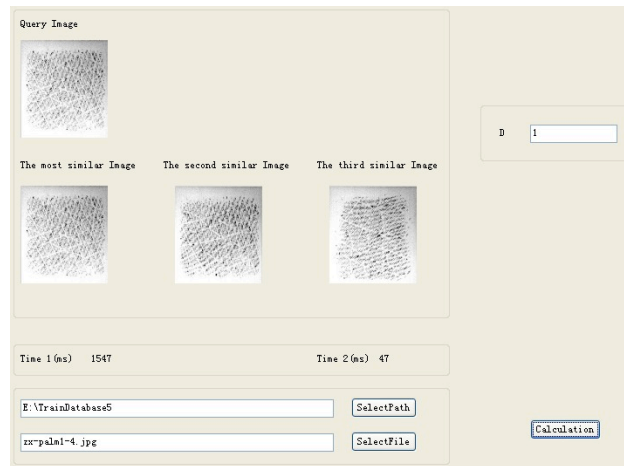
(b)

(c)

**Figure 7.2** *Capacitive skin image retrieval results using PCA, GLCM and Gabor wavelet transform.*

Figure 7.2 shows the retrieval results of three different algorithms for grayscale capacitive skin images which were captured from the Fingerprint sensor. The query images are grayscale capacitive skin images captured from finger, eye, face, forehead, neck, volar forearm and palm. Because of space limitation, this chapter only lists the retrieval results of grayscale capacitive skin images of eye, palm and forehead. Other retrieval results are available in the Appendix 1. Clearly, in this case, all three algorithms can correctly retrieve grayscale capacitive skin images from eye, palm and forehead, despite the similarity of these images. If the successful retrieval rate is defined by correctly retrieving the most and the second similar images, then the performance of three algorithms can be compared. There are totally 33 grey capacitive skin images in the database, and the number of successful retrieval image completed by PCA, GLCM and Gabor wavelet transform are 17, 25 and 31, respectively. Therefore, although results show that the three different algorithms could be used for the retrieval of the different parts of the human body skin, Gabor wavelet transform has the highest retrieval accuracy rate for capacitive skin images.

Figure 7.3 and Figure 7.4 are the results of skin cancer/disease image retrieval. The query images in Figure 7.3 are all skin cancer images. From the results, most of the three retrieved images are skin cancer images. The query images in Figure 7.4 are skin disease images of leucoderma. From the results, except the retrieval result of PCA, the three most similar images are all leucoderma images. According to the retrieval success rate defined as above, there are eight skin disease images in the database, and the number of successful retrieval image completed by PCA, GLCM and Gabor wavelet transform are 3, 6 and 5, respectively. The results show that the three different algorithms could be potentially used for skin disease diagnostics, but GLCM is the most accurate for retrieving of skin cancer/diseases images.

(a)



(b)
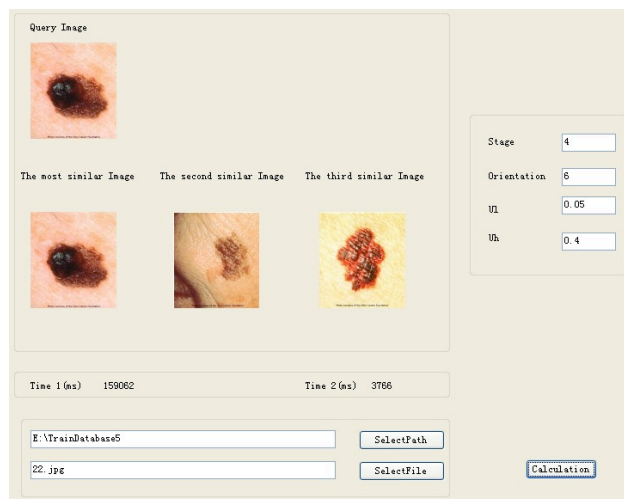


(c)

***Figure 7.3*** *Skin cancer image retrieval results using PCA, GLCM and Gabor wavelet transform.*

(a)



(b)



(c)

***Figure 7.4****Skin disease image retrieval results using PCA, GLCM and Gabor wavelet transform.*
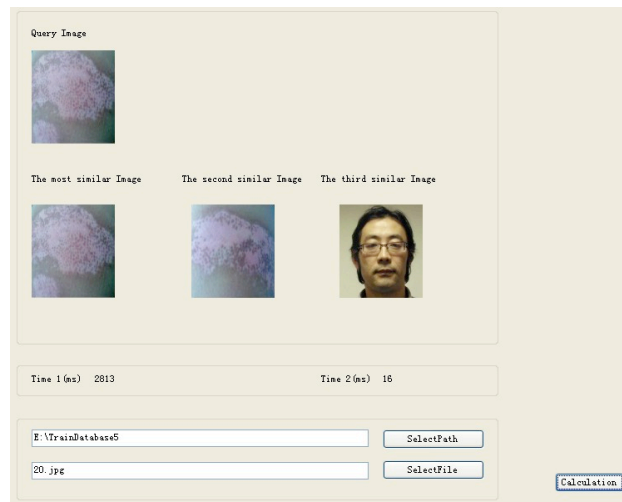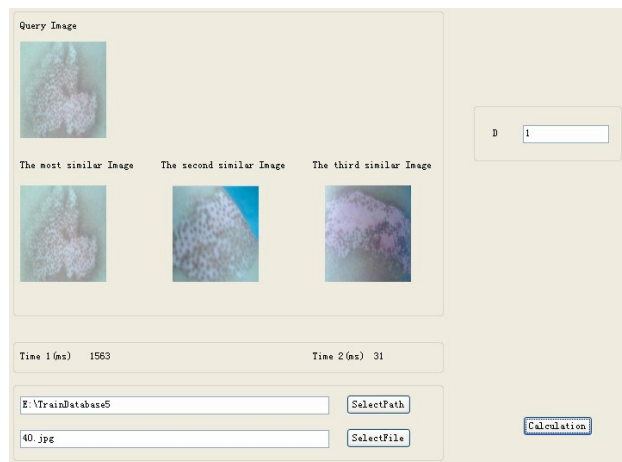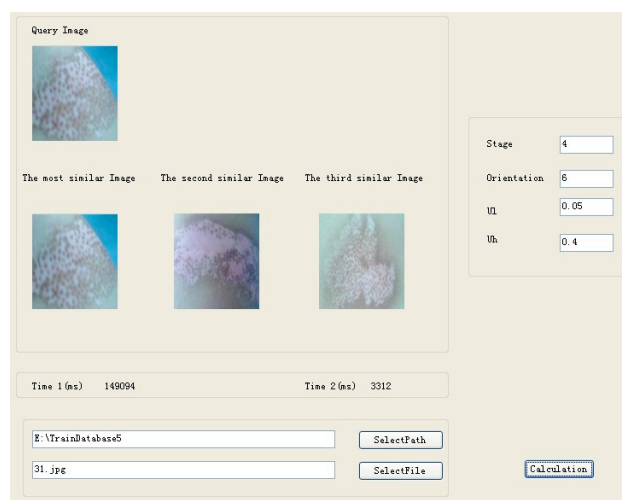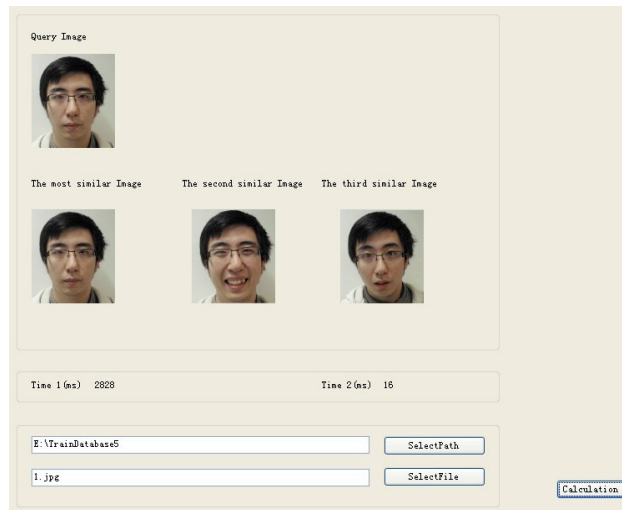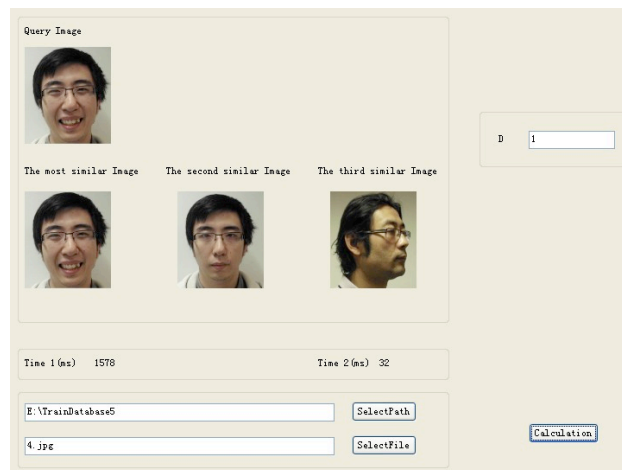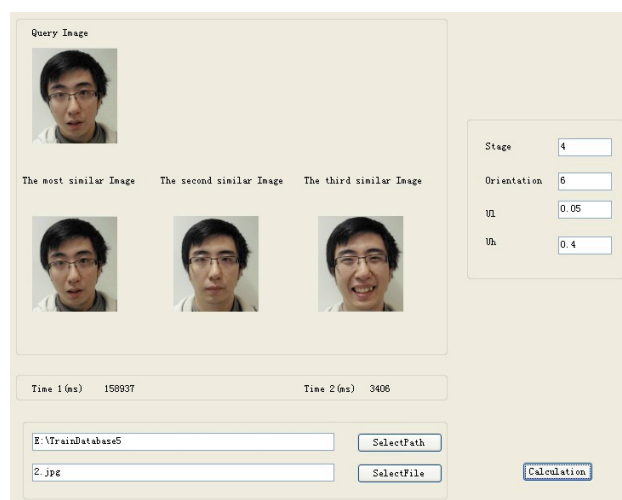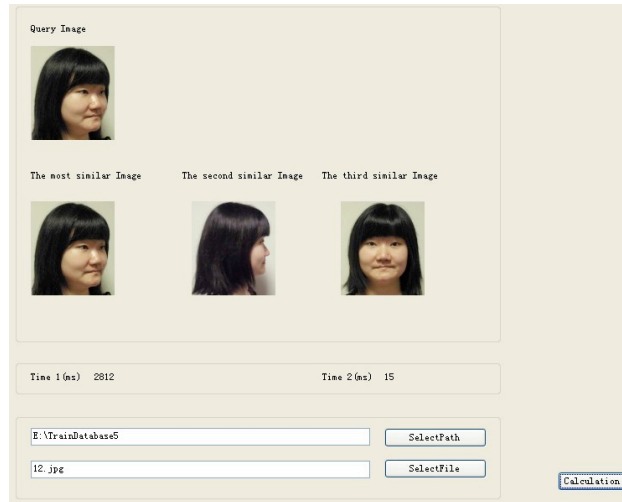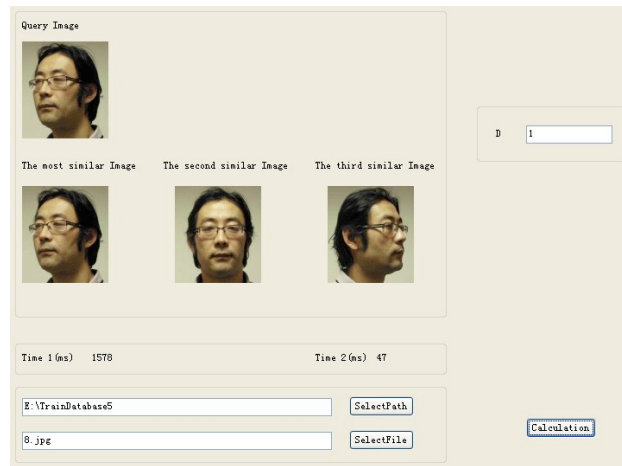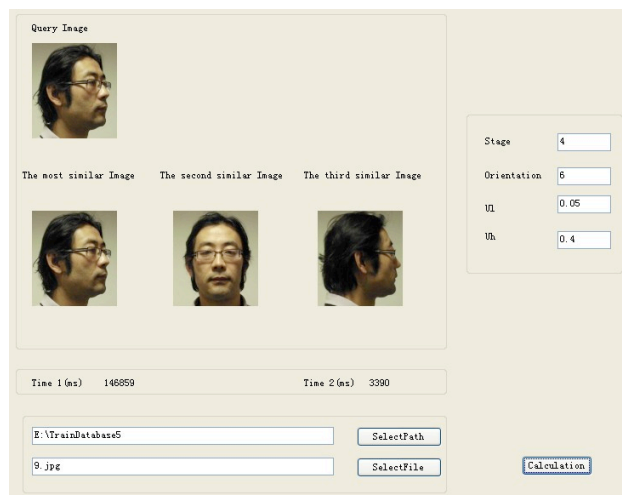
(a)



(b)



(C)

***Figure 7.5*** *Face image retrieval results using PCA, GLCM and Gabor wavelet transform.*

(a)



(b)



(C)

***Figure 7.6*** *Face image retrieval results using PCA, GLCM and Gabor wavelet transform.*

Figure 7.5 shows the retrieval results for query images using human faces with different expressions. Human face images in the database are with three different facial expressions: smile, non-smile and surprised. From the retrieval results, the three most similar images are the same person with different facial expressions. By calculating the successful retrieval rate, it can be concluded that PCA is the most accurate for human faces with different expressions retrieval.

Figure 7.6 shows the retrieval results for query images using human faces with different orientations, i.e. left facing, front facing, right facing. From the retrieval results, the three most similar images are all the same person with different orientations. There are 10 human face images with different orientations in the database, the number of successful retrieval image completed by PCA, GLCM and Gabor wavelet transform are 4, 3 and 6, respectively. In this case, Gabor wavelet transform has the best retrieval accuracy rate. The results show that all the three different algorithms have certain reference value for human face recognitions.

Table 7.1 and 7.2 compare the Time 1 and Time 2 of using three different algorithms to retrieve different grayscale capacitive skin images captured from face, finger, neck and volar forearm. Time 1 represents the total time used to calculate the feature vectors of all the images in the database and Time 2 represents the computing time used to calculate the similarity of the feature vectors of all the images in the database to the feature vectors of the query image. In table 7.1, the results show that GLCM is the fastest for calculating the feature vectors of database images, whilst Gabor wavelet transform is the slowest. In table 7.2, the results show that PCA is the fastest for retrieving images, and Gabor wavelet transform is the slowest. For more image retrieval results, see Appendix 1.

|  | PCA | GLCM | Gabor Wavelet Transform |
|---|---|---|---|
| Face | 2594 | 1406 | 132953 |
| Finger | 2594 | 1406 | 134765 |
| Neck | 2594 | 1406 | 136734 |
| Volar forearm | 2594 | 1406 | 133328 |

**Table 7.1** *Time 1 (ms) - the total time used to calculate the feature vectors of all the images in the database*

|  | PCA | GLCM | Gabor Wavelet Transform |
|---|---|---|---|
| Face | 16 | 47 | 3094 |
| Finger | 15 | 31 | 3031 |
| Neck | 16 | 46 | 3078 |
| Volar forearm | 15 | 31 | 3140 |

**Table 7.2** *Time 2 (ms) - the computing time used to calculate the similarity of the feature vectors of all the images in the database and the feature vectors of the query image.*

## 7.3 Conclusions

In summary, a comparison study of three different algorithms, e.g. Principal Component Analysis (PCA), Grey level co-occurrence matrix (GLCM) and Gabor wavelet transform, on image retrieval has been conducted. Four different types of images, face images, skin cancer images, skin disease images, and capacitive skin images, are used in the study. The results show that different algorithms have different performances. In the term of computing time, Gabor wavelet transform is the slowest in both database calculation and image retrieval. GLCM is the fastest for database calculation, and PCA is the fastest for image retrieval. In the term of successful retrieval rate, Gabor wavelet transform is the highest for retrieving capacitive skin images, GLCM is the highest for retrieving skin cancer / disease images, PCA is the highest for retrieving facial images with different expressions, and

Gabor wavelet transform is the highest for retrieving facial images with different orientations. Table 7.3 shows a quick summary of the performance of each algorithm.

|  | Time 1 | Time 2 | Image type 1 | Image type 2 | Image type 3 | Image type 4 | Image type 5 |
|---|---|---|---|---|---|---|---|
| Gabor wavelet transform | Slow | Slow | Average | Best | Best | Average | Average |
| GLCM | Fast | Fast | Worst | Worst | Average | Best | Best |
| PCA | Medium | Medium | Best | Average | Worst | Worst | Worst |

**Table 7.3** *The performance of each algorithm. Time 1 represents the total time used to calculate the feature vectors of all the images in the database, Time 2 represents the computing time used to calculate the similarity of the feature vectors of all the images in the database and the feature vectors of the query image, i.e. retrieval time. Image type 1 to image type 5 are human face images with different expressions, human face images with different orientations, grey capacitive skin images of skin textures of the different parts of human body, skin diseases and cancer images.*

# Chapter 8 Conclusions and Future Works

## 8.1 Conclusions

This thesis is concentrated on skin hydration and solvent penetration measurements by Opto-thermal Radiometry, AquaFlux and capacitive contact imaging based on Fingerprint Sensors. A variety of theoretical and experimental investigations have been performed, conclusions are as following:

In the theoretical investigation, three different mathematical algorithms were developed for analyzing skin images. Firstly, a content-based image retrieval algorithm using 2D Gabor wavelet texture feature was developed. The results show that it can be very useful for human face recognition, facial expression recognition, skin cancer and skin disease diagnostics. The results also show that Gabor wavelet transform is particularly effective for retrieving grayscale skin capacitive images of the different parts of human body, which are very similar in texture. Secondly, an algorithm based on Grey level co-occurrence matrix (GLCM) has been developed specially for analyzing capacitive skin images. The results show that GLCM algorithm can effectively separate the skin texture information from the solvent penetration information from the same skin images, which makes it very useful for studying skin texture, as well as studying solvent penetrations through both skin and membranes. It is found that GLCM can also be used for image retrieval.

Finally, a comparison study, to compare the performance of Gabor wavelet transform, Grey level co-occurrence matrix (GLCM) and Principal Component Analysis (PCA) for image retrieval, has been conducted. Four different types of images, e.g. human faces, skin cancers, skin diseases, and capacitive skin images are used. The results show that although Gabor wavelet transform is the slowest, it is the most efficient for retrieving capacitive skin images and human facial images with different orientations.

GLCM is medium fast, but very effective for retrieving skin cancer images and skin disease images. PCA is the fastest, and very efficient for human facial images with different expressions.

For opto-thermal radiometry hardware design research, in order to overcome the limitations of the existing bench-top OTTER technology, a new low cost, portable opto-thermal radiometry instrument has been designed and a prototype has been developed. It uses a modulated broadband Infrared Emitter to heat up the sample surface, a room temperature PbS detector to pick up the blackbody radiation of the sample. The initial study shows that it can work on a range of different materials such as the back of hand, forearm, thumb, white paper, aluminum, dry cardboard and wood, which makes it a potential useful tool for non-destructive testing for arbitrary materials.

In experimental investigation, various *in-vivo* and *in-vitro* experiments are performed in order to develop new methodologies for skin hydration and solvent penetration measurements by using OTTER, AquaFlux and capacitive contact imaging based on Fingerprint sensors, as well as to have a better understanding of capacitive contact imaging measurements. The results have demonstrated that capacitive contact imaging could be a very useful tool for skin hydration and solvent penetration measurements, due to its imaging capabilities. The results show that detection depth of Fingerprint sensor was about $50\,\mu m$, which mean the capacitive contact imaging is mainly measuring the top part of epidermis. The effects of Fingerprint sensors' configuration parameters, namely, discharge time, discharge current and gain, were also studied, in order to have a better understanding of the capacitive contact imaging measurements, and the best values were chosen for the measurements.

**8.2 Future Work**

For the future work, the following are suggested:

*A: Improvements for portable Opto-thermal radiometry instrument*

In order to get more accurate results, on the one hand, the preamplifier section will be further improved to filter more noise; on the other hand, before the signal reaches the detector, it will be collected by a parabolic mirror and then sent to PbS detector through a diffraction grating, which will distinguish the infrared emission signal from reflected and refracted signals.

*B: Investigate new methodologies for solvent penetration measurements through skin by using AquaFlux and capacitive contact imaging based on Fingerprint sensors.*

Solvent penetration is a heavily researched area. More new solvents will be investigated for solvent penetration measurements, both through skin and membranes. Different types of membranes can also be investigated in these experiments.

*C: New mathematical algorithms for skin image processing*

In image retrieval investigation, although Gabor wavelet transform is a powerful tool which is adapted to extract features for capacitive skin image retrieval, the nonorthogonality of the Gabor wavelet implies that there is redundant information in the filtered images. In order to solve this problem, some algorithms, such as AdaBoost will be applied to eliminate redundant information, which will reduce the computation time and improving the retrieval accuracy.

For skin research, the research on human skin roughness is of great interest in several

different research fields, such as Clinical Science and Pharmaceutics. For future work, Gabor wavelet transform, Grey level co-occurrence matrix (GLCM) and other algorithms for the human texture analysis, such as Markov Random Field will be applied in skin capacitive images captured by Fingerprint sensors. Through comprehensive analysis of the results, it should be able to get more accurate characteristic parameters for human skin roughness study.

# References

[1] Swarbrick, J. and Boylan, "Permeation Enhancement through Skin", Encyclopedia of Pharmaceutical Technology, <u>11</u>, pp. 449-492, 1995.

[2] Van De Graaff KM, Fox SI, "Concepts of Human Anatomy & physiology", Wm C Brown Publishers, 1995.

[3] Sotiropoulou, P.A., Blanpain, C., "Development and homeostasis of the skin epidermis", Cold Spring Harb Perspect Biol. <u>4</u>(7), 2012.

[4] William, A.C., Barry, B.W., "Skin Absorption Enhancers", Critical Reviews in Therapeutic Drug Carrier Systems, <u>9</u>(3,4), pp. 305-353,1992.

[5] Junqueira, L.C., Carneiro J., "Basic Histology", 12$^{th}$ edition, Prentice Hall, USA 2009.

[6] Geerligs, M., "Skin layer mechanics", Universiteitsdrukkerij TU Eindhoven, Eindhoven, The Netherlands, 2009.

[7] Barry, B.W., "Dermatological Formulations (Percutaneous Absorption)", New York: Taylor & Francis, 1983.

[8] Ng, J., Rohling, R., Lawrence, P.D., "Automatic measurement of human subcutaneous fat with ultrasound", IEEE Trans Ultrason Ferroelectr Freq Control. 56(8), 2009.

[9] Warner, Myers and Taylor, "Water concentration profile across human skin", The Journal of Investigative Dermatology. <u>90</u>, pp.199-224, 1988.

[10] Spencer, T.S., Linamen, C.E., Akers, W.A., Jones, H.E., "Temperature dependence of water content of stratum corneum. Br J Dermatol", <u>93</u>, pp. 159-164, 1975.

[11] Blank, I.H., Moloney, J., Emslie, A.G., Simon, I., Apt, C., 'The diffusion of water across the stratum corneum as a function of its water content", J .Invert. Dermatol..<u>82</u>, pp. 188-194, 1984.

[12] Tsai, J., Weiner, N.D., Flynn, G.L. and Ferry, J., "Properties of adhesive tapes used for stratum corneum stripping", International Journal of Pharmaceutics, 72, pp. 277-231, 1991.

[13] Anderson, R.L, Cassidy, J.M., Hansen, J.R. and Yellin, W., "Hydration of Stratum Corneum. Biopolymers", 12, pp. 2789-2802, 1973.

[14] Xiao, P. and Imhof, R.E., "Opto-thermal measurement of stratum corneum thickness and hydration depth profile", SPIE Proc, 2970, pp. 276-86, 1997.

[15] Opto-Thermal Transient Radiometry (OTTER) ,
http://ecce3.lsbu.ac.uk/staff/xiaop/Research/otter.html [access date: 12/ 09/ 2013]

[16] Imhof, R.E., Birch, D.J.S., Thornley, F.R., Gilchrist, J.R. and Strivens, T.A., "Opto-thermal transient emission radiometry", Journal of Physics E: Scientific Instruments, 17 (6), pp. 521-525, 1984.

[17] Xiao, P., Gull, S.F. and Imhof, R.E., "Opto-Thermal Inverse Modelling Using a Maximum Entropy Approach", Analytical Sciences, 17, pp. s394-s397, 2001.

[18] Imhof, R.E., Zhang, B. and Birch, D.J.S., "Progress in Photothermal and Photoacoustic Science and Technology . ed Mandelis A (Englewood Cliffs USA: PTR Prentice Hall), pp.185-236, 1994.

[19] Xiao, P., Imhof, R.E., "Opto-thermal measurement of water distribution within the stratum corneum", Skin Bioengineering Techniques and Applications in Dermatology and Cosmetology, Curr Probl Dermatol, Basel: Karger, 26, pp.48-60, 1998.

[20] AquaFlux, http://www.biox.biz/Products/AquaFlux/AF200Page01.php [access date: 12/ 09/ 2013]

[21] Imhof, R.E., O'Driscoll, D., Xiao, P. and Berg, E., "New sensor for water vapour flux", Sensors and their Applications X, pp. 173-177, IoP Publishing, 1999.

[22] Nuutinen, J., Alanen, E., Autio, P., Lahtinen, M.R., Harvima, I. and Lahtinen, T., "A Closed unventilated chamber for the measurement of transepidermal water loss", Skin Research and Technology, 9, pp. 85-89, 2003.

[23] Agner, T., Held, E., West, W. and Gray, J., "Evaluation of an experimental patch test model for the detection of irritant skin reactions to moisturisers", Skin Research

Technology, 6, pp. 250-254, 2000.

[24] http://www.ee.washington.edu/research/seal/projects/moisture sensing /
projecttoverview. htm [access date : 31/ 1/ 2014].

[25] Fingerprint Sensor for Skin Hydration Imaging,
http://ecce3.lsbu.ac.uk/staff/xiaop/Research/epsilon.html [access date: 31/ 1/ 2014]

[26] Singh, H., "Development of a Measurement Instrument Using Capacitance
Sensors Techniques to Image and Measure the Skin Surface Hydration". Ph.D thesis,
London South Bank University, November 2010.

[27] Singh, H., "Development of a Measurement Instrument Using Capacitance
Sensors Techniques to Image and Measure the Skin Surface Hydration", PhD Thesis,
London South Bank University, November 2010.

[28] Singh, H., Xiao, P., Berg, E.P., and Imhof, R.E., "Skin Capacitance Imaging for
Surface Profiles and Dynamic Water Concentration Measurements", ISBS
Conference, Seoul, Korea, May 7-10, 2008.

[29] Ou, X., Pan, W., Xiao, P., "In vivo skin capacitive imaging analysis by using
grey level cooccurrence matrix (GLCM)", International Journal of Pharmaceutics,
460, pp. 28-32, 2014.

[30] Xiao P., Ou X., Ciortea L.I., Berg E.P., Imhof R.E., "In Vivo Skin Solvent
Penetration Measurements Using Opto-thermal Radiometry and Fingerprint Sensor".
Int J Thermophys. 33, pp.1787–1794, 2012.

[31] Wang, J.Z.. "Integrated Region-Based Image Retrieval. Boston:Kluwer
Academic". 2001, 1-5.

[32] Haralick, R.M., Shanmugam, K., and Dinstein, I., "Texture features for image
classification". IEEETrans. Syst. Man Cybern. SMC(8), 1973,11, 610–621.10.

[33] Hayes, K.C., Shah, Jr. A.N., and Rosenfeld, A., "Texture coarseness: further
experiments". IEEETrans SMC-4, 467-472.

[34] Yang, J., Liu, L., Jiang T., and Fan, Y., "A modified Gabor filter design method
for fingerprint image enhancement. Pattern Recognition Letters", 24(12),
pp.1805-1817, 2003.

[35] Daugman, J.G., "Uncertainty relation for resolution in space, spatial frequency,

and orientation optimized by twodimensional visual cortical filters", Journal of The Optical Society of America, 2(7), pp.1160-1169, 1985.

[36] Kruizinga, P., Petkov, N., and Grigorescu, S.E., "Comparison of texture features based on Gabor filters", Proceedings of the 10th International Conference on Image Analysis and Processing, pp.142-147, 1999.

[37] Sifuzzaman, M., Islam, M.R., and Ali, M.Z., "Application of Wavelet Transform and its Advantages Compared to Fourier Transform", Journal of Physical Sciences, 13, pp. 121-134, 2009.

[38]Wavelet Transform,

http://www.cse.iitm.ac.in/~vplab/courses/CV_DIP/PDF/Lect-wavelet_filt.pdf  [access date: 31/ 2 / 2014]

[39] Smith, J.R., "Integrated Spatial and Feature Image System: Retrieval, Analysis and Compression". Ph.D thesis, Columbia University, 1997.

[40] Thangairulappan, K., Jeyasingh, J.B.V., "Face Representation Using Combined Method of Gabor Filters, Wavelet Transformation and DCV and Recognition Using RBF", Journal of Intelligent Learning Systems and Applications, 4, pp.266-273, 2012.

[41] Deng, Y., "A Region Representation for Image and Video Retrieval". Ph.D thesis, University of California, Santa Barbara, 1999.

[42] Dimai, A., "Rotation Invariant Texture Description using General Moment Invariants and Gabor Filters". Proc. Of the 11th Scandinavian Conf. on Image Analysis. I, 6, pp.391-398, 1999.

[43] Liu, Z, "An Improved Face Recognition Method Based on Gabor Wavelet Transform and SVM", Fifth International Symposium on Computational Intelligence and Design (ISCID), 10, pp.378– 381, 2012.

[44] Fischer, S., "Minimum entropy transform using Gabor wavelets for image compression", 11th International Conference on Image Analysis and Processing and Proceedings, 9,428 – 433, 2001.

[45] Kamarainen, J.K., Kyrki, V., " Invariance Properties of Gabor Filter- Based Features- Overview and Applications", IEEE Transactions on Image Processsing, 15, 2006.

[46] Manjunath, B.S., and Ma, W.Y., "Texture features for browsing and retrieval of image data", IEEE Trans. Pattern Anal. Machine Intell, 8, pp.837–842, 1996.

[47] Yu, L., and Meng, X.P., "Image texture feature detection based on Gabor filter", Journal og Changchun University of Technology (Natural Science Edition). 29(1), pp. 78-81, 2008.

[48] Skin cancer and skin diseases images:

http://skincancer.about.com/od/symptoms/ss/mole_all.htm [access date: 31/ 1/ 2014]

[49] Li, Y., Meng, X.P., "Image texture feature detector based on Gabor filter", Journal of Changchun University of Technology (Natural Science Edition), 29 (1), pp.78-81, 2008.

[50] Anne, H., Solberg, S., "Jain A.K. Texture fusion and feature selection applied to SAR imagety [J]", IEEE transaction on Geoscience and Remote sensing, 35(2), pp.475-478, 1997.

[51] Leveque, J.L., Querleux, B., SkinChip, a new tool for investigating the skinsurface in vivo. Skin Res. Technol. 9, pp.343–347, 2003.

[52] Batisse, D., Giron, F., Leveque, J.L., "Capacitance imaging of the skin surface". SkinRes. Technol. 12, pp.99–104, 2006.

[53] Xiao, P., Singh, H., Zheng, X., Berg, E.P., Imhof, R.E., "In-vivo skin imaging forhydration and micro relief measurements", In: Stratum Corneum V Conference,Cardiff, UK, 2007.

[54] Bevilacqua, A., Gherardi, A., "Characterization of a capacitive imaging systemfor skin surface analysis". In: First International Workshops on Image ProcessingTheory, Tools & Applications, 2008.

[55] Singh, H., Xiao, P., Berg, E.P., Imhof, R.E., "Skin capacitance imaging for surfaceprofiles and dynamic water concentration measurements". In: ISBS Conference, Seoul, Korea, 2008.

[56] Xiao, P., Lane, M.E., Abdalghafor, H.M., "Membrane solvent penetration mea-surements using contact imaging". In: Stratum Corneum VII Conference, Cardiff, UK, 2012.

[57] Xiao, P., Ou, P., Ciortea, L.I., Berg, E.P., Imhof, R.E., "In-vivo skin solvent

penetra-tion measurements using opto-thermal radiometry and fingerprint sensor". Int.J. Thermophys, <u>33</u>, pp.1787–1794, 2012.

[58] Haralick, R.M.,"Textural features for image classification", IEEE Trans. Syst.Man Cybern., SMC 3, pp.610–621, 1973.

[59] Haralick, R.M., "Computer classification of reservoir sandstones", IEEE Trans.Geosci. Electron. <u>11</u>, pp.171–177, 1973.

[60] Haralick, R.M., "Statistical and structural approaches to texture". Proc. IEEE <u>67</u>, pp.786–804, 1979.

[61] Ulaby, F.T., Kouyate, F., Brisco, B., Williams, T.H.L., IEEE Trans. Geosci. RemoteSens. GE-24, pp.235–245, 1986.

[62] Siew, L.H.,"Texture measures for carpet wear assessment", IEEE Trans. PatternAnal. Mach. Intell. <u>10</u>, pp.92–105, 1988.

[63] Parekh, R., "Using texture analysis for medical diagnosis", IEEE MultiMedia, <u>19</u>, pp.28–37, 2012.

[64] Zhu, L.q., "Auto-classification of insect images based on color his-togram and GLCM", In: 2010 Seventh International Conference onFuzzy Systems and Knowledge Discovery (FSKD), <u>6</u>, pp. 589–2593, 2010.

[65] Kekre, H.B., Thepade, S.D., Sarode, T.K., and Suryawanshi, V., "Image Retrieval using Texture Features extracted from GLCM, LBG and KPE", International Journal of Computer Theory and Engineering, <u>2</u>, pp. 1793-8201, 2010.

[66] Gonzalez, R.C., and Woods, R.E., "Digital Image Processing", Third Edition. Prepared by Pearson Education. pp. 142-161, 2007.

[67] Gao, C., Hui, X., "GLCM-based texture feature extraction". Comp. Syst. Appl. <u>19</u>, pp.195–198, 2010.

[68] Baraldi, A., "An investigation of the textural characteristics associated with graylevel cooccurrence matrix statistical parameters", IEEE Trans. Geosci. RemoteSens. <u>33</u>, pp.293–304., 1995.

[69] Kekre, H.B., Thepade, S.D., Sarode, T.K. and Suryawanshi, V., "October. ImageRetrieval using Texture Features extracted from GLCM, LBG and KPE", Interna-tional Journal of Computer Theory and Engineering, <u>2</u>(5), pp. 1793-8201,

2010.

[70] Conners, R.W., "A theoretical comparison of texture algorithms", IEEE Trans.Pattern Anal. Mach. Intell., PAMI 2, pp.204–222, 1980.

[71] Tahir, M.A., "An FPGA based co-processor for GLCM texture features mea-surement", In: Proceedings of the 2003 10th IEEE International Conference onElectronics, Circuits and Systems, 2003. ICECS 2003, 3(14–17), pp.1006–1009, 2003.

[72] Bremananth, R., "Wood Species Recognition Using GLCM and Correlation", Advances in Recent Technologies in Communication and Computing, 2009. ARTCom '09. International Conference on. pp. 615 - 619 , 2009.

[73] Xu, S.F., Wu, S.L., Li, H., "An analysis on Human Skin Texture based on Gray-level Co-occurrence Matrix", ACTA Laser Biology Sinica, 20, pp.324-327, 2011.

[74] Philippe, P., Ohanian and Richard, C.D., "Performance Evaluation for Four Classes of Textural Features", Pattern Recognition, 25 (8), pp.819-833, 1992.

[75] Simon, I., "Infrared Radiation", D. Van Nostrand Company, USA, 1966.

[76] Hackforth, H.L., "Infrared Radiation", Literary Licensing, LLC, 2012.

[77] Vignola, F., Michalsky, J., Stoffe, T., "Taylor and Francis Group", USA, 2012.

[78] Electromagnetic spectrum: http:// www. Unwittingvictim.com/ Absorbers.html [access date: 31/ 1/ 2014]

[79] Cook, D., "Intermediate Robot Building", springer, USA, 2010.

[80] Capper, P., Elliott, C.T., "Infrared Detectors and Emitters: Materials and Devices: Materials and Devices", Kluwer Academic Publishers, 2001.

[81] Rogalski, A., "Infrared Detectors, Second Edition", CRC Press, 2011.

[82] Driggers, R.G., "Encyclopedia of Optical Engineering", CRC Press, 2003.

[83] Piotrowski, J., Rogalski, A., "High- operating- temperature Infrared", SPIE, 2007.

[84] Rogalski, A., Adamiec, K., "Narrow-gap Semiconductor Photodiodes", SPIE, 2000.

[85] INFRARED EMISSION: A NEW POSSIBLE APPROACH TO PARTICLE

DETECTORS,http://www.slac.stanford.edu/pubs/icfa/fall98/paper2/paper2.html

[access date: 31/ 1/ 2014]

[86] Lasercomponents:

http://www.lasercomponents.com/de/?embedded=1&file=fileadmin/user_upload/hom
e/Datasheets/cal/infrared-emitter-pire-plus.pdf&no_cache=1 [ access date: 31/ 1/
2014];

[87] Lasercomponents , http://www.lasercomponents.com/uk/product/pbs-1-33-um/
[access date: 31/ 1/ 2014];

[88] Lasercomponents:

http://www.lasercomponents.com/fileadmin/user_upload/home/Datasheets/cal/pbs-det
ector-specifications.pdf [access date: 31/ 1/ 2014];

[89] Baltes, H.P., Prog. Opt., 13,3,1979.

[90] Notingher, I., "New Instrument for Thermal Emission Decay Fourier Transform
Infrared Spectroscopy and Applications", Ph.D. thesis, London South Bank
University, 2001.

[91] Berg, E.P., O'Driscoll, D., and Imhof, R.E., "Fast, low noise preamplifiers for
pulsed Opto-thermal radiometry", Photoacoustic and photothermal Phenomena: 10th
International Conference, 1999.

[92] Saar, B.G., Contreras-Rojas, L.R., Xie, X.S., Guy, R.H., "Imaging Drug Delivery
to Skin with Stimulated Raman Scattering Microscopy", Molecular Pharmaceutics, 8
(3), pp. 969-975, 2011.

[93] Principal Component Analysis:

http://people.maths.ox.ac.uk/richardsonm/SignalProcPCA.pdf [access date: 20/ 3/
2014];

[94] Ilin, A., Raiko, T., "Practical Approaches to Principal Component Analysis in the
Presence of Missing Values", Journal of Machine Learning Research. 11 ,
pp.1957-2000, 2010.

[95] A tutorial on Principal Components Analysis:

http://www.cs.otago.ac.nz/cosc453/student_tutorials/principal_components.pdf
[access date: 20/ 3/ 2014];

[96] Baldland, P., Hornikp, K., "Neural Networks and Principal Component Analysis: Learning from Examples Without Local Minima", Neural Networks. <u>2</u>, pp. 53-58, 1989.

[97] Jolliffe, I.T.; Trendafilov, N.T., Uddin, M. "A modified principal component technique based on the LASSO", Journal of Computational and Graphical Statistics, <u>12</u>(3), pp. 531–547, 2003.

[98] An introduction to Principal Component Analysis (PCA): http://spider.ipac.caltech.edu/staff/fmasci/home/statistics_refs/PrincipalComponentAnalysis.pdf [access date: 20/ 3/ 2014];

[99] Wolds, W., Esbensen, K., Geladi, P., "Principal Component Analysis", Chemometrics and Intelligent Laboratory Systems, <u>2</u>, pp. 37-52, 1987.
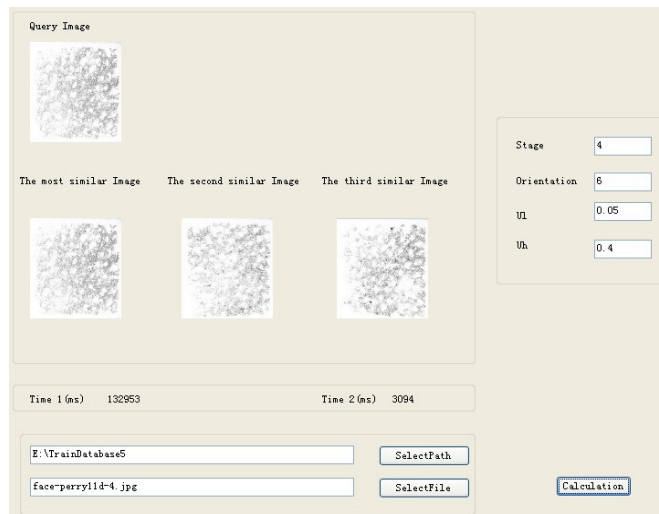
## APPENDIX 1

The images shown below indicate the retrieval results of three different algorithms, namely, PCA, GLCM and Gabor wavelet transform for grayscale capacitive skin images, as described in chapter 7. The query images are grayscale capacitive skin images captured from skin sites on finger, eye, face, forehead, neck, volar forearm and palm. For the details of the GUI (graphical user interface), see chapter 7.
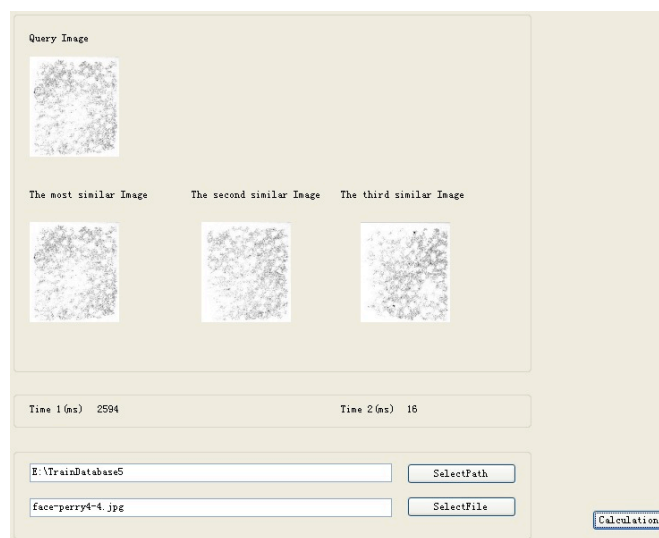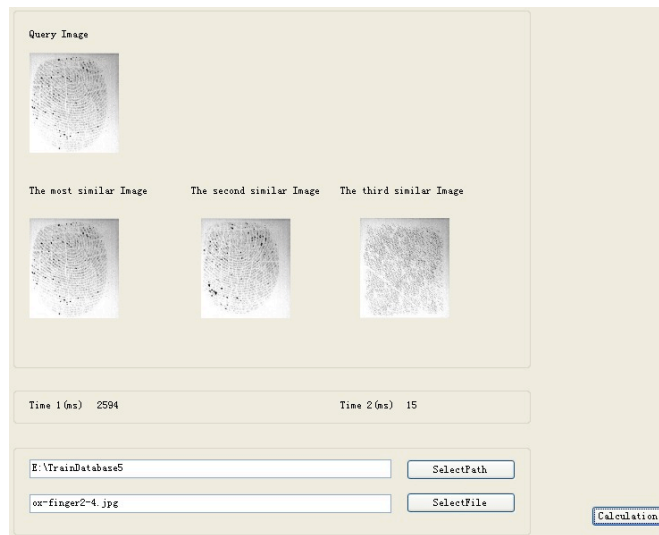


(a) PCA- face
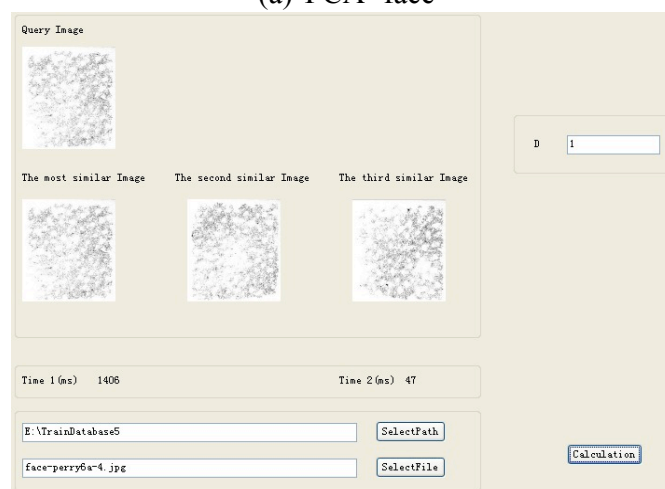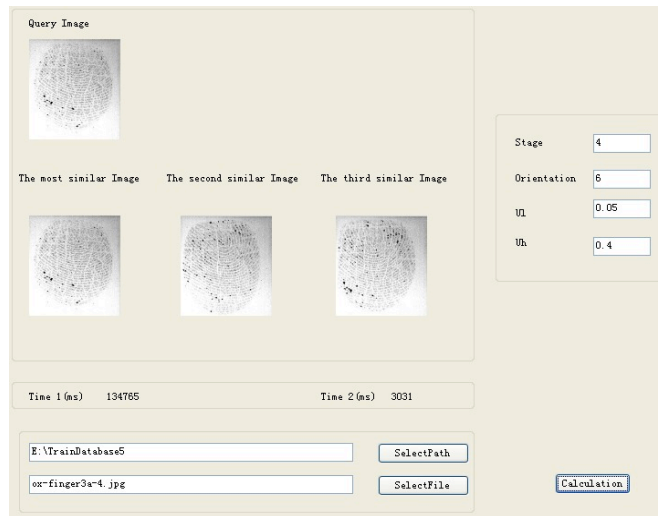


(b) GLCM- face

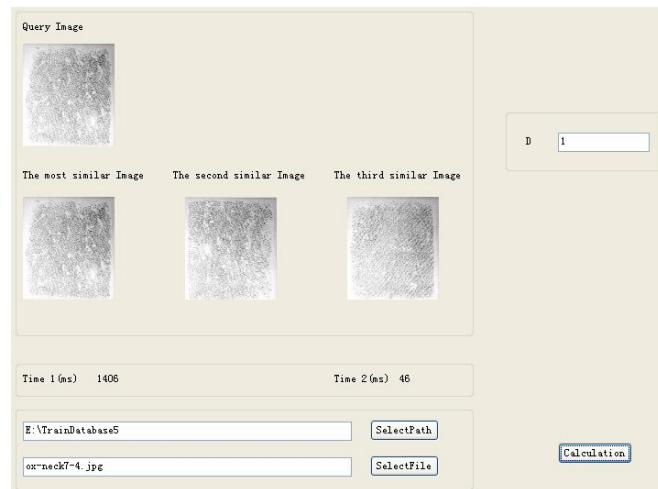(c) Gabor wavelet transform- face



(d) PCA- finger



(e) GLCM- finger

(f) Gabor wavelet transform- finger

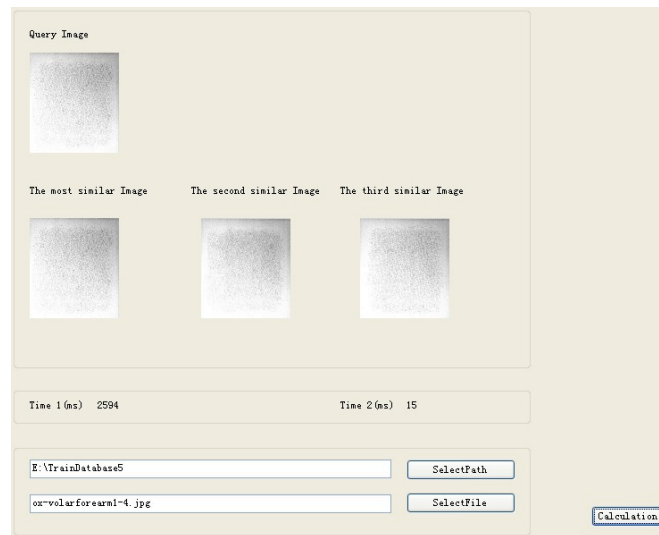

(g) PCA- neck



(h) GLCM- neck

(i) Gabor wavelet transform- neck



(j) PCA- volar forearm



(k) GLCM- volar forearm

Query Image

The most similar Image    The second similar Image    The third similar Image

| | |
|---|---|
| Stage | 4 |
| Orientation | 6 |
| Ul | 0.05 |
| Uh | 0.4 |

Time 1(ms)    133328                    Time 2(ms)    3140

E:\TrainDatabase5                    SelectPath

ox-volarforearm6-4.jpg                SelectFile                Calculation

(l)  Gabor wavelet transform- volar forearm

**APPENDIX 2**

Publications

1. Ou, X., Pan, W., Xiao, P., "In vivo skin capacitive imaging analysis by using grey level co-occurrence matrix (GLCM)", *International Journal of Pharmaceutics*, Volume 460, 2014, Pages 28–32.
2. Pan, W., Ou, X., Zhang, X., Xiao, P., "Skin Damage Assessment by Using Capacitive Imaging and Condenser-TEWL Method", *Perspectives in Percutaneous Penetration 14th International Conference, La Grande Motte*, France, April 23-25, 2014.
3. Xiao, P., Pan, W., Ou, X., "Digital Imaging Processing for in-vivo Skin Measurements", *in 1$^{st}$ IET Intelligent Signal Processing (ISP) conference*, London, UK, December 2-3, 2013.
4. Ou, X., Xiao, P., "Human skin texture analysis using Gray-level Co-occurrence Matrix", *Skin Forum 13th Annual Meeting, London*, UK, June 25-26, 2013.
5. Xiao, P., Ou, X., Ciortea L.I., Berg E.P., "*In vivo* Skin Solvent Penetration Measurements Using Opto-thermal Radiometry and Fingerprint Sensor", *International Journal of Thermo physics*, Volume 33, 2012, Pages 1787- 1794.
6. Xiao, P., Pan, W., Ou, X., "Digital Imaging Processing for in-vivo Skin Measurements", *International Journal of Cosmetic Science*, Volume 34, 2012, Pages 387-387.
7. Xiao, P., Pan, W., Ou, X., "Digital Imaging Processing for in-vivo Skin Measurements", *STRATUM CORNEUM VII*, Cardiff , UK, Sep. 10-12,2012.
8. Xiao, P., Singh H., Ou, X., Caparnagiuc A R., Ciortea LI., Berg EP., Imhof RE., "In-vivo Trans-Dermal Drug Delivery Study by Using Capacitive Fingerprint Sensors", *Skin Forum 12$^{th}$ Annual Meeting*, Frankfurt, Germany, March 28-29, 2011.